

F. Southern Regional Center for Lightweight Innovative Design

Field Technical Monitors: Dr. Mark F. Horstemeyer and Dr. Paul Wang
Mississippi State University
Center for Advanced Vehicular Systems
Box 5405
Mississippi State University, MS 39762
(662)325-5449; e-mail: mfhorst@me.msstate.edu
(662)325-2890; e-mail: pwang@cavs.msstate.edu

Technology Area Development Manager: William Joost
U.S. Department of Energy
1000 Independence Ave., S.W.; Washington, DC 20585
(202) 287-6020; e-mail: william.joost@ee.doe.gov

Contractor: Mississippi State University (MSST)
Contract No.: DE-FC-26-06NT42755 and DE-EE0002323

Executive Summary

Light-weighting materials are critical to reducing emissions and the United States' reliance on foreign oil. Understanding how light-weighting materials utilized in vehicles perform in crash scenarios is paramount, for passenger safety as well as energy efficiency are primary design challenges facing today's automotive industry. The Southern Regional Center for Lightweight Innovative Design (SRCLID) plans to develop an experimentally validated cradle-to-grave modeling and simulation effort to optimize automotive and truck components in order to decrease weight and cost while increasing performance and safety in crash scenarios. This end-to-end ("Atoms to Autos") modeling effort requires that we quantify the microstructure-property relations of lightweight materials by evaluating them at various length scales, starting at the atomic level, for each step of the manufacturing process.

Mississippi State University (MSST) magnesium (Mg) research team is focusing on generating process-structure-property (PSP) relationships for a number of Mg alloys, where a physics-based multiscale internal state variable (ISV) model, including uncertainty, has been deployed for use in the sheet forming process. Sheet bending and extrusion teams have made significant progress in validating and predicting PSP relationships and they have applied such tools to support United States Automotive Materials Partnership (USAMP) Mg demo projects. The MultiStage Fatigue (MSF) Model has been correlated with different Mg alloy strain-life curves and extended to describe friction stir welding (FSW) joint behavior. The MSST steel research team has established a number of atomistic potentials (i.e., Iron (Fe), Carbon (C), Silicon (Si), Aluminum (Al), and Mg) that will be used in development of high strength steel alloys. The polymer team's efforts have included research in natural fiber, polymeric materials, biomechanics, and nanocomposites. The natural fiber program has produced high quality samples for evaluation and the feedback was positive. The biomechanics program has advanced to incorporating polymeric ISV models for tissues and evaluating damage phenomena for brain subject to high rate impact using finite element (FE) analyses. The composites effort has entailed development of multiscale material models to describe process/product concepts. Cyberinfrastructure has integrated our own proprietary software, external software, and experimental information into a wiki and has garnered high recognition from TMS and USAMP. In conjunction with the development of multiscale material models, our design team has established optimization methods, including ISV and PSP, with FE analysis and design. With uncertainty under low and high strain rate tension-compression-torsion tests, we have characterized several structural materials for lightweighting (i.e., Al, steel, and Mg alloys) throughout their respective manufacturing and life cycle histories. We then tested these materials in crash simulations and safety performance evaluations. We have produced a number of high quality graduates with MS and PhD degrees. For the K-12 program, we have developed crash kits and run K-2 and 3-6 grade "Mission Eggcellence" competitions in multiple counties throughout Mississippi in an effort to inspire young students' interest in science and engineering.

Activity and Developments

Task 1 - Multiscale Material Models and Design Framework for Lightweight Alloys (Magnesium and Aluminum)

Principal Investigator: Seong-Gon Kim, Physics & Astronomy, MSST
(662) 325-8031; email: kimsg@hpc.msstate.edu

Co-Principal Investigators: M. F. Horstemeyer, H. Rhee, S. Kim

Objective

Develop a multiscale framework for lightweight materials that accounts for statistical variations from the material microstructure, product geometry, and processing parameters, and utilize the multiscale framework to aid in development of new lightweight alloys and in the design of lightweight structures for automotive applications.

Approach

We are developing a material database and an ISV material and process models for lightweight alloys including Mg and Al. The database will include results from mechanical and microstructural characterization studies performed using advanced experimental techniques. The material model is formulated by a multiscale modeling approach where information from crystal plasticity, dislocation dynamics, and molecular dynamics simulations are utilized to provide insights into the functional forms of the ISV's evolution equations and corresponding material parameters. Finally, a design framework contained in the cyberinfrastructure will be developed to design structural components of new lightweight alloys.

1.1. Internal State Variable Plasticity Modeling

Team Members: Y. Hammi, A.L. Oppedal, M.F. Horstemeyer, E.B. Marin, Q. Ma

Accomplishments

- An ISV material model with mixed hardening laws for Mg AZ31 alloy was established, applicable for warm forming where twinning effect is not yet included.
- An implicit stress integration algorithm was implemented in Abaqus Finite Element Modeling (FEM) software to solve sheet forming conditions.

Results and Discussion

The microstructure-plasticity coupled with damage (DMG) ISV model was used in this work to describe the nonlinear response of the material behavior. A robust fully-implicit stress integration algorithm was developed and implemented in the user material subroutine Vumat of Abaqus/Explicit for 3D, plane strain, and plane stress conditions. Plasticity and hardening parameters can be calibrated from experimental stress-stress curves or from the evolution of polycrystal-based yield surface (PCYS). **Figure 1** shows the evolution of the two-dimensional projection of PCYS using experimental data on tension and compression performed on samples from a 12mm thick AZ31B sheet.

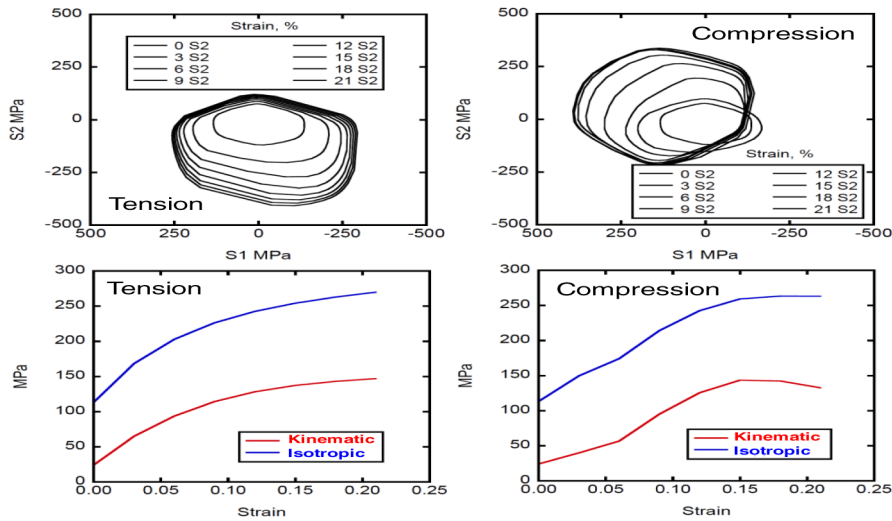


Figure 1. PCYS for tension and compression using the VPSC code and their respective isotropic and kinematic hardening evolution curves.

The PCYS was obtained by incrementally probing it along different strain-paths (i.e. applying different strain-rates $\dot{\epsilon}_{ij}$ and obtaining the corresponding stress response σ_{ij}) in the Visco-Plastic Self Consistent (VPSC) crystal code. By averaging the size of the yield surface and tracking the center of the yield surface, PCYS plots were processed to determine the evolution of isotropic and kinematic hardening for both isotropic and kinematic hardenings. The DMG model with AZ31B plasticity parameters was applied to pan forming and bending simulations (Figure 2).

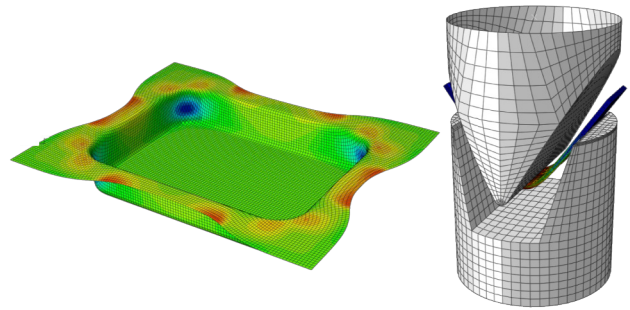


Figure 2. Pan forming and bending simulations using the DMG model.

1.2. Visco-Plastic Self-Consistent Crystal Plasticity for Magnesium Alloy

Team Members: Q. Ma, A.L. Oppedal, H. El Kadiri

Accomplishments

- A VPSC crystal code was employed to describe slip and twinning responses of AM30 alloy
- Stress-strain responses of AM30 at room and elevated temperatures with various strain rates were quantified and simulated by the VPSC code.

Results and Discussion

The measured and VPSC predicted stress-strain curves at room temperature and 450 °C and the corresponding hardening curves are presented in Figures 3 and 4, respectively.

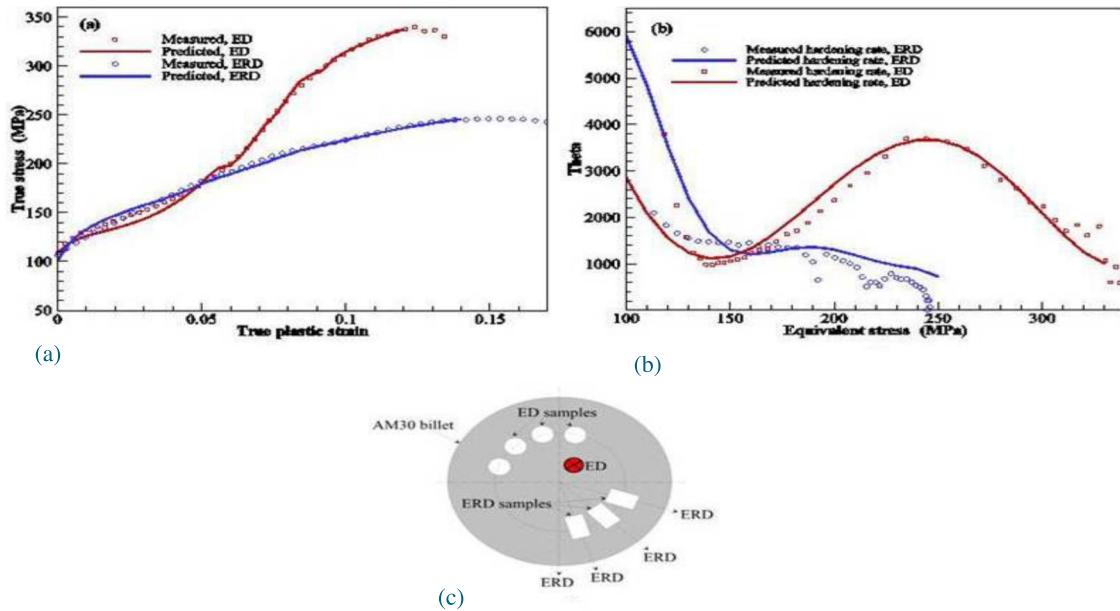


Figure 3. Measured and VPSC predicted mechanical results of AM30 at 25 °C. (a) Measured and VPSC predicted stress-strain curves; (b) measured and VPSC predicted hardening curves; and (c) the extrusion direction (ED) samples and the extrusion radial direction (ERD) samples in the AM30 billet.

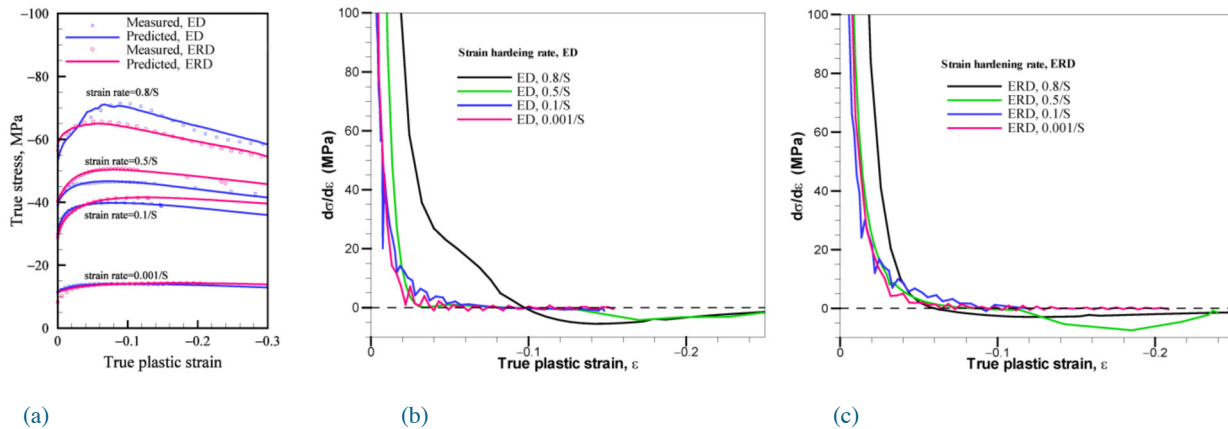


Figure 4. Measured and VPSC predicted mechanical results of AM30 at 450 °C. (a) Stress-strain curves of ED and ERD; (b) measured hardening curves at the ED, and (c) measured hardening curves at the ERD.

At room temperature, the extrusion direction (ED) σ - ϵ curve shows a typical “s” shape which signifies profuse twinning. Twinning could be observed by the very high hardening rate in the stress-strain curves along the ED. The extrusion radial direction (ERD) σ - ϵ curve shows the normal plasticity response. At 450 °C, the σ - ϵ curves are dependent on strain rate and have no such S shape curves. For the ERD, hardening is weaker than what was observed in the ED. At 450 °C, dynamic recrystallization (DRX) is pervasive and results in the softening of the σ - ϵ curves.

1.3: Sheet Forming - Experiments and Modeling

Accomplishments

- Two sets of bending test fixtures were designed and fabricated for sheet bending experimentation conducted at a field emission gun system scanning electron microscope (FEG-SEM) chamber and an Instron machine.
- The FEM-based VPSC+UMAT code was implemented on an MSST server and preliminary numerical results look promising, with the capabilities of describing texture/twinning evolution and mechanical responses of the sheet bending process. (Figure 5)

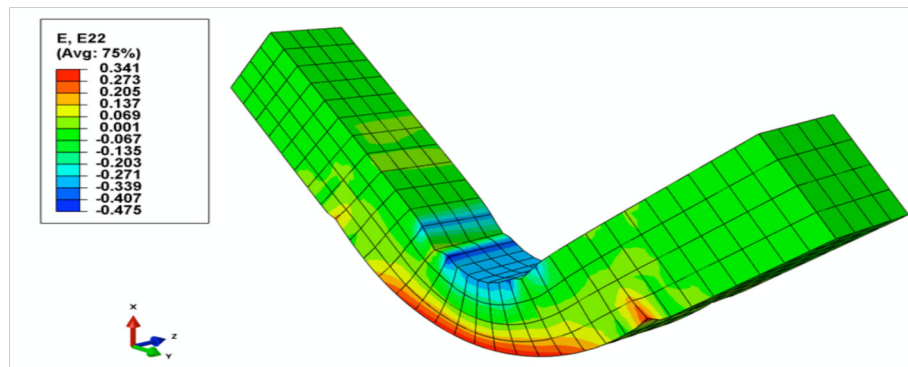


Figure 5. VPSC+UMAT modeling with parallel computing successfully reproduced bending results reported in the literature.

Results and Discussion

Anomalous twin bands were captured in the in situ electron backscatter diffraction (EBSD) scan. High density twins are localized in alternating bands in the compression zone of the sheet during bending. In between the bands, no twins are present. The nature of these twin bands and how they affect sheet forming, especially at room temperature, requires systematic studies. VPSC+UMAT modeling with parallel computing successfully reproduced bending results reported in the literature. Bending of AZ31 sheet is being modeled with the VPSC+UMAT code.

1.4. Extrusion Process

Team Members: E. Marin, C. Bouvard, S.J. Horstemeyer, A.L. Oppedal, Q. Ma. Students: Z. McClelland (UG), S. Bhandari (UG), G. Long (UG)

Accomplishments

- AM30 lab-scale extrusion experiments with flat die has been completed.
- The extrusion process model (HX) is able to describe the flat die extrusion responses including load, displacement, and temperature curves.
- A post-process technique using VPSC code to describe the texture and twinning evolutions during extrusion is implemented and compares well with experiments.

Results and Discussion

The aspect of our extrusion research is summarized in Figure 6. We have completed the AM30 lab-scale flat-die extrusion experiments using different processing parameters: ram speeds of 5, 10, 15, 20, 30 and 40 mm/min, billet temperatures of 454°C and 482°C, and an extrusion ratio (ER) of 25. Load and temperature profiles together with microstructure information have been recorded for model validation. Current extensions of these experiments are focused on extruding AM30 with various die geometries including conical dies, dies for dog-bone profiles, and porthole dies for circular cross section tubes.

FE simulations of the flat-die extrusion experiments have been carried out using HX and a flow-stress type model (sine hyperbolic inverse law) (Figure 7). The material parameters for AM30 were fitted to experimental stress-strain curves produced at CAVS and from the literature. Predicted results for the load-time and temperature-time curves compared well with the experimental ones. Additional work on extrusion process modeling for other dies' geometries is in progress. Also, HX developers (from Altair) are working on extending the capabilities of the code to use ISV material models.

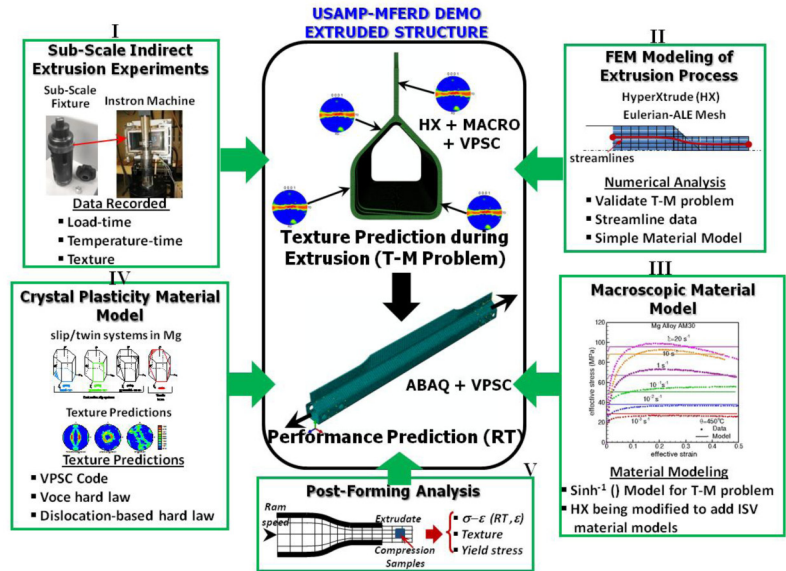


Figure 6. Overview of research activities on extrusion at CAVS as related to the USAMP-MFERD project.

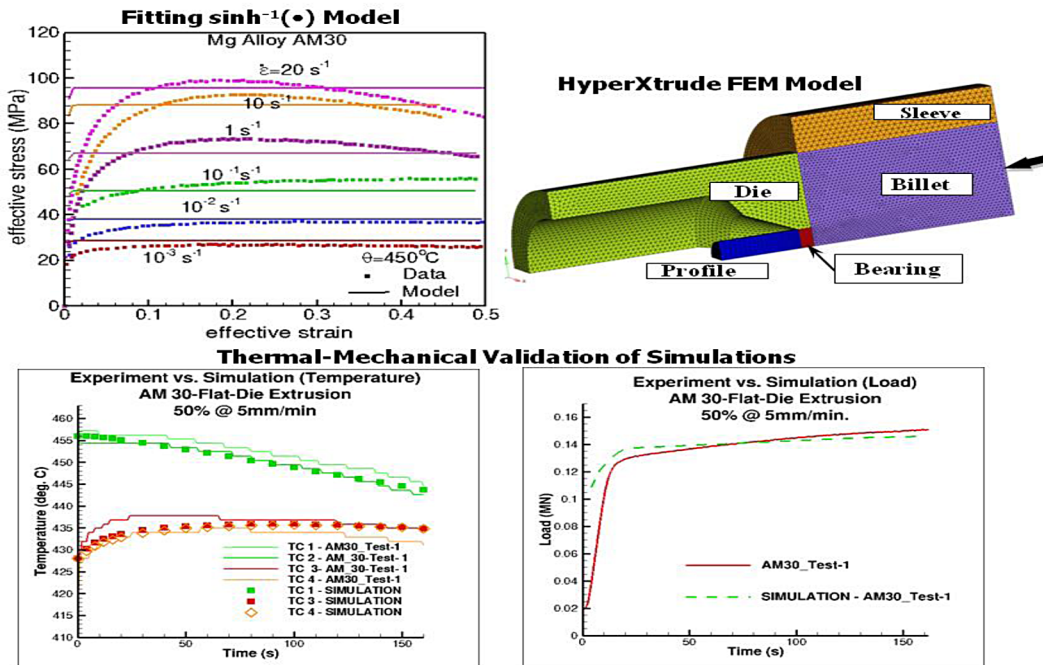


Figure 7. Validation of flat-die extrusion experiments of AM30 using numerical tools: HX and Sinh-1(*) model

Microstructure (texture and twinning) evolution of material particles during the extrusion process is being modeled using the VPSC formulation. Deformation histories along streamlines were obtained from the HX post-processor and used in the VPSC code to compute texture and get a detailed account of the slip/twinning activity in the material. A crystal-level dislocation-based model that represents rate- and temperature-dependence response is being used for this purpose. This methodology has been applied to predict texture during AM30 flat die extrusion. Computed texture patterns agreed well with experimental (EBSD) ones.

Predicting the microstructure and mechanical properties of the material after extrusion is essential for the post-forming structural analysis of the extruded component. In this respect, mechanical tests and microstructure studies are being performed on specimens cut from flat-die extruded rounded bars obtained with ERs of 6.25 and 25. Specimens have been subjected to compression at different strain rates and room temperature (RT), with the recorded data being the stress-strain curves and initial and deformed textures (see Figure 8). These data will be used for testing the capability of the developed numerical tools to predict the mechanical properties of the extrudate.

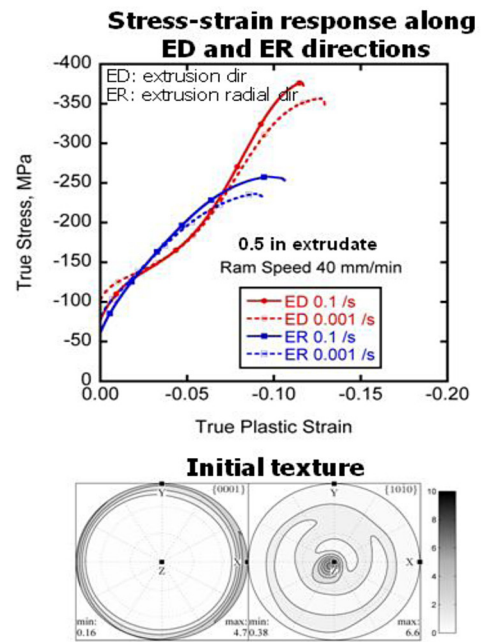


Figure 8. Characterization of compression specimens from flat-die AM30 extruded material

1.5. High Rate Damage and Fracture

Team Members: P. Gullett, W. Whittington

Accomplishments

- Bridgman tension testing was conducted for cast AM60 alloy and the initial porosity distribution quantified.
- Simulation results of tension testing with three initial states (random, uniform, and actual distributed) of porosity revealed that the initial state of porosity distribution has significant impact on the accuracy of predicting failure strain, and it has no impact on the shape of force versus strain curve.

Results and Discussion

Damage Based Failure Predictions

The internal state variable based, microstructural damage model developed by Bammann et al. (1993), then expanded by Horstemeyer (2000) and Hammi and Horstemeyer (2007), was used to examine the effect of microstructural details on simulated failure prediction of a cast AM60B notched Bridgman tensile specimen (Figure 9). Three initial porosity distributions were evaluated and the simulations were compared with experimentally measured results. The three initial porosity states included the experimentally measured porosity distribution, a uniform porosity distribution and a random porosity distribution. For these simulations, total porosity of the numerical model was held constant.



Figure 9. Notched Bridgman tension specimen.

Figure 10 shows a plot of the specimen's predicted axial force versus strain response for the three initial porosity cases, as well as the damage distributions (dark regions correspond to areas of high porosity) for each case at their predicted failure strains. The lower left shows the damage distribution for the experimentally-measured initial damage distribution, the upper left shows the random initial distribution, and the upper right shows the homogeneous initial distribution. The diagrams show that the evolution of damage varies significantly with the choice of initial distribution. The random and uniform distributions result in porosity grown and initial failure near the notch root where the triaxial stress is a maximum, while the actual distribution predicts growth in regions of high initial porosity far from the notch root.

The axial force-strain response shows that the initial porosity distribution has virtually no effect on the shape of the force versus strain response of the tensile specimen. Both the yield and hardening behavior were similar for all distributions. The predicted strain at failure however varies greatly with the initial porosity distribution. The predicted strain at failure for the real distribution is 3.3%, for the random distribution is 8.8%, and 12.3% for the homogeneous distribution. The random and homogenous distributions over predict the actual strain at failure by 170% and 270%, respectively. Therefore, the initial porosity distribution plays a vital role in accuracy of simulation-based failure predictions.

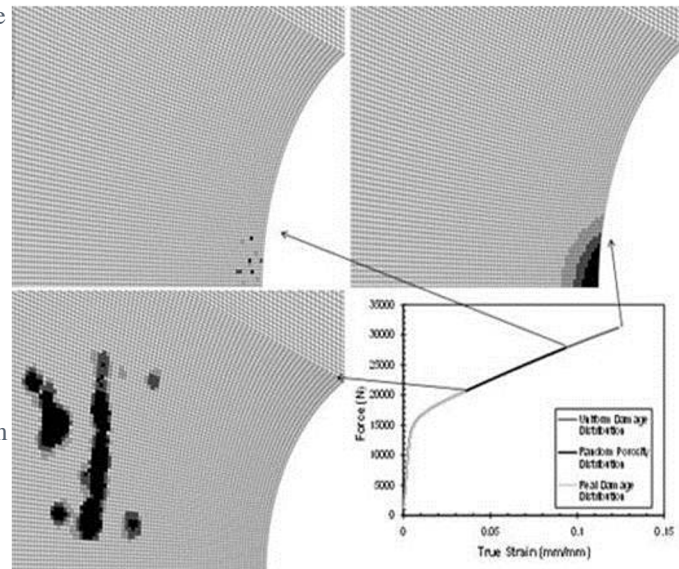


Figure 10. The plot shows the predicted stress strain response for three initial damage distributions. The figures show predicted damage distributions damage (dark) at the failure strain.

1.6. Cyberinfrastructure

Team Members: T. Haupt, R. Carino

Accomplishments

The wiki, which has served as the knowledge management component of the Engineering Virtual Organization for Cyber Design (EVOCD), is made available to the ICME community. The wiki provides access to all portal components: the repository of the experimental data and material constants, online model calibration tools, and the repository of the open source codes.

Results and Discussion

The EVOCD portal is up and running. It has been accessed more than 16,000 times by about 8,000 visitors and contributors from over 80 nations around the world since September 1, 2010. The wiki (<http://icme.hpc.msstate.edu>), shown in Figure 11, serves as the knowledge management component of EVOCD. It supports the accumulation of knowledge pertaining to ICME. Recently added search and indexing capabilities have simplified the navigation through the site contents. In addition, the wiki provides access to all portal components: the repository of the experimental data and material constants, online model calibration tools, and the repository of the open source codes. In the near future, it will also provide access to an autonomic runtime environment for composing and executing multiscale workflows directly from the Web Browser. The wiki is currently populated with information, tutorials, data, and results coming from the other SRCLID tasks. The EVOCD becomes a node of the global ICME cyberinfrastructure – an effort coordinated by TMS.

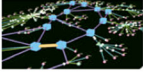
<p>Welcome!</p> <p>Integrated Computational Material Engineering (ICME) is an emerging discipline transforming materials science. Computational engineering accelerates materials development, integrates design and manufacturing, and unifies these with the engineering design optimization process, as well as efficiently employs greater accuracy in simulation-based design. Read more...</p> <p>Efforts to realize this enormous and complex goal have catalyzed the development of the Engineering Virtual Organization for Cyber Design (EVOCD), which provides a cyberinfrastructure to accumulate and protect the intellectual property pertaining to selected aspects of materials science and engineering that is generated by the participants of the organization, to enforce the quality of that information, and to manage its complexity. The intellectual property includes experimental data, material models and constants, computational tools and software artifacts, and the knowledge pertaining to multiscale physics-based models for selected properties and processes. Read more...</p>	<p>Call for Participation</p> <p>The Cyberinfrastructure team created the infrastructure for web-based collaborative efforts. The success of this effort critically depends on the participation of the community towards the generation of the contents that will aid the research in Materials Science and lightweight innovative design. Read more ...</p> <p>How to contribute</p> <p>To learn how to contribute please see our short Tutorial. Please note that contributions (creating new pages or editing existing ones) can be made only by the registered users.</p>	<p>EVOCD components</p> <ul style="list-style-type: none"> ▪ This Wiki ▪ Repository of Data ▪ Repository of Codes ▪ Tools <p>Site Index</p> <ul style="list-style-type: none"> ▪ Overview Pages ▪ Research Topics ▪ Materials ▪ Material Models ▪ Multiscale Simulations ▪ Tutorials ▪ Input Decks
<p>ICME Cyberinfrastructure</p>  <p>In the vision of the National Materials Advisory Board (NMAB) of the National Academy of Engineering (NAE) committee, the ICME cyberinfrastructure will emerge from individual web sites which offer access to information, data, and tools, each established for specific purposes by different organizations. Linked together, these "constituent" Web Portals will form the ICME cyberinfrastructure. EVOCD is one of the nodes of the emerging cyberinfrastructure. Read more ...</p> <p>TMS The creation of the ICME infrastructure is coordinated by the The Minerals, Metals, and Materials Society (TMS).</p>	<p>Elements of ICME Cyberinfrastructure</p> <p>We would also like to invite you to other materials oriented databases: Materials Atlas, nanoHub, matweb, MatData, Granta Design, Knowledgebase of Interatomic Potentials (OpenKIM), Korean Materials Design, MatForge/MatDL, National Institute of Standards and Technology (NIST) Data Gateway</p> <p>See also TMS ICME forum</p>	<p>Our Sponsors</p>  <p>(NSF Award ID: 0742730)</p>  <p>(DOE contract 4000054701) DOE Southern Regional Center for Lightweight Innovative Design (SRCLID)</p>
<p>Contact</p> <p>Tomasz Haupt  Mark Horstemeyer </p>		

Figure 11. Home page of the EVOCD Wiki

1.7. Fatigue Performance of Lightweight Materials

Team Members: M. F. Horstemeyer, M. Lugo, B. Jordon, T. Tang, J. Bernard, A. Yeldell, D. Rayborn

Accomplishments

- We have conducted strain-life fatigue tests for an extruded AM30 in the extruded and transverse directions and for three different wrought products of AZ31 alloy: extruded, plate, and sheet.
- We have developed MSF models for AZ31, AM60, and AZ91 alloys.
- We have conducted fractography analysis of fracture surfaces of AZ31 and AM30 alloys.
- We have made microstructure sensitive fatigue model predictions for FSW of different welds under various welding conditions and performed fractography analysis to determine failure mechanisms.

Results and Discussion

Fatigue Modeling of AZ31 Magnesium Alloy in Extrusion, Plate and Sheet Forms

The strain-life fatigue behavior of AZ31 Mg alloy in the extrusion, plate, and sheet formation were examined and structure-property relations were quantified. Nearly identical asymmetric cyclic stress-strain behavior was observed in the extrusion and plate materials when compared to the sheet material which exhibited more symmetric hysteresis loops. Twinning was observed on fracture surfaces of the extrusion material, while no evidence of twinning was observed on fracture surfaces of the plate and sheet materials. However, intermetallic particles at or near the surface were identified as sources of fatigue crack initiation in all three materials. A multistage fatigue model was employed to predict the fatigue damage in the three differently processed materials. The multistage model comprises three scales of fatigue damage: crack incubation, microstructurally small crack and physically small crack, and long crack growth. In addition, the fatigue model incorporates microstructure influences resulting from crystallographic orientation, grain size, and inclusion size in the incubation and growth stages.

Figure 12 shows a typical SEM fracture surface for the extruded alloy. The initiation crack sites occurred near surface at inclusion particles. In most cases, fractured particles were identified to be the fatigue crack initiation sites. Also observed in the SEM images was evidence of twinning on the fatigue fracture surfaces similar to what has been reported elsewhere (Yang et al., 2008; Morita et al., 2010).

Figure 13 shows the correlations of the MSF models to the experimental strain-life data. Longer lives were generally observed for the sheet material; the MSF model also reflects this difference and correlates well for the three materials. The grain size can have an influential impact on fatigue lifetimes (Ochi et al., 2006; Ishihara et al., 2007), and as such the small crack formulation can capture this effect. Particle size is the other factor contributing to this difference in fatigue performance, as noted in other Mg alloys (Jordon et al., 2011). The effect of twinning is captured through the cyclic stress-strain response.

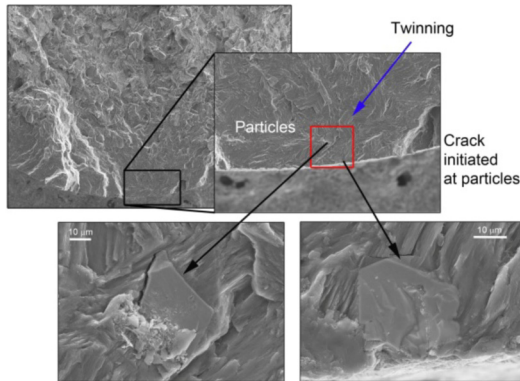


Figure 12. Fractured surface for an AZ31 Mg alloy at 0.6% of strain amplitude.

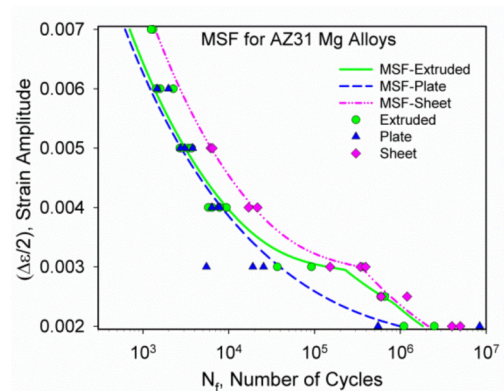


Figure 13. Comparison of the MSF model to the strain-life results of the extrusion, plate and sheet materials of AZ31.

Cyclic Behavior and Microstructure Properties of an Extruded AM30 Magnesium Alloy

Strain controlled experiments were conducted to study the cyclic behavior of an AM30 Mg alloy. Anisotropy and asymmetric behavior were identified in both the extrusion and transverse directions. Formation of cracks occurred for most of the samples at inclusions of second particles, which were identified as Al-Mn rich. In addition, other initiation crack sites were observed to occur due to profuse twinning. Figure 14 shows the strain-life for extruded AM30 Mg alloy in the extrusion and transverse directions, for strain controlled, constant strain amplitude, and completely reversed loading conditions. The strain-life curve in the log-log domain shows a linear pattern from 0.6 to close to 0.3 %; then the slope changes drastically to a strain amplitude of below 0.3%.

Figure 15 shows the evolution of stress amplitude as a function of the number of cycles at the strain amplitudes of 0.6%, 0.5%, 0.3%, and 0.2%. The strain amplitudes ranging from 0.3% to 0.6% show a greater hardening effect than the other strain amplitude levels. The cyclic hardening appears strongly in the initial cycles at about 10% of the total fatigue life and a small amount of hardening continued to the point of the final failure. This hardening effect is most likely related to twinning in compression and detwinning in tension that occurs at high strain amplitudes (Brown et al., 2007).

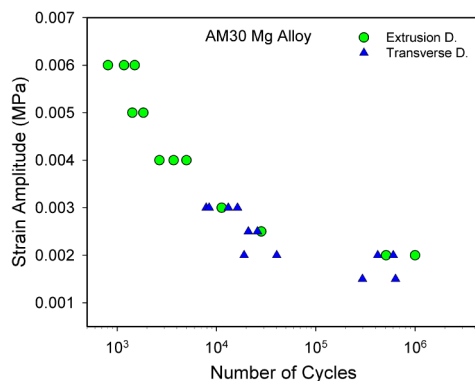


Figure 14. Total strain life of an AM30 Mg alloy in the extrusion and transverse directions.

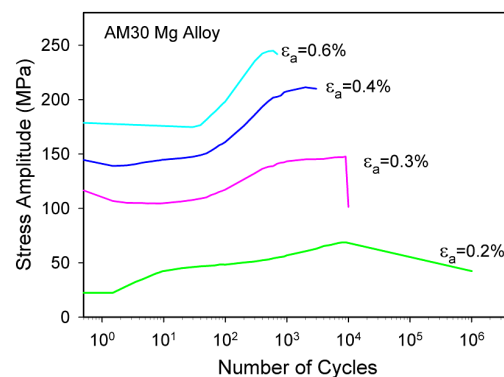


Figure 15. Stress amplitude response of AM30 Mg Alloy.

Fatigue Modeling of Friction Stir Spot Welding Joints for Magnesium Alloys

The purpose of this task is to develop a microstructure-sensitive model for predicting fatigue damage in spot welded joints made using friction stir technology. In order to realize this goal, relationships of microstructural and geometrical features to fatigue performance were investigated using AZ31 Mg alloy sheets joined by friction stir spot welding (FSSW). Fractography analysis conducted in this study suggested that the effective top sheet thickness largely determined the failure mode, which in turn influenced the final number of cycles to failure. While the height of the interfacial hook was greater in the process with better fatigue performance, it was the larger effective top sheet thickness that promoted crack propagation modes more favorable to greater fatigue resistance. To further aid in determining the cause and effect relationships and to elucidate the mechanisms behind fatigue damage in FSSW, a linear elastic fracture mechanics model was used to correlate the fatigue life in the two processes. The fatigue model, which is a function of hook size, sheet thickness, and nugget diameter, showed good correlation to the experimental results as shown in Figure 16. The use of this model revealed that the fatigue of the FSSW was most sensitive to the sheet thickness in the weld zone, followed by hook height, and then nugget diameter. As such, the shoulder plunge depth during the FSSW process may likely be the dominant factor in producing durable spot welds using this novel welding technique.

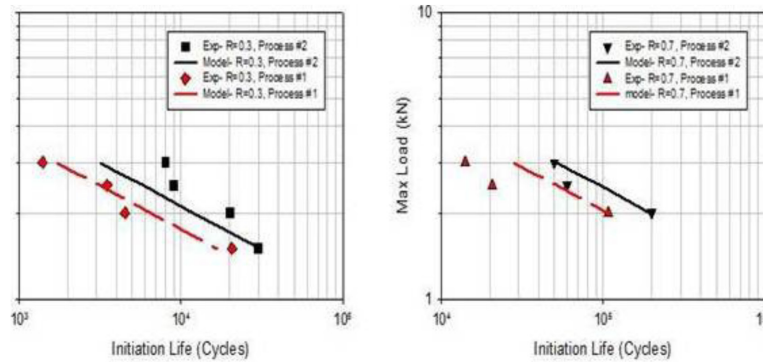


Figure 16. Comparison of the fatigue model to the experimental results of FSSW lap-joints for two welding conditions (process #1 and #2).

1.8. Multiscale Modeling of Corrosion

Team Members: M. F. Horstemeyer, H.J. Martin, Students: C. Walton (GRA), W. Song (GRA)

Results and Discussion

Figures 17(a) and (b) show the average weight and thickness loss, respectively, over the five exposure times for the immersion and salt spray surfaces on AZ91 and AM30. As one can see, all surfaces follow similar logarithmic trends for weight loss (Figure 17(a)) and thickness loss (Figure 17(b)). The samples exposed to the salt spray environment gained weight and thickness, while both sets of samples exposed to the immersion environment lost weight (Figure 17(a)), although AM30 lost a minimal amount of weight. Only the AZ91 immersion samples experienced a thickness loss.

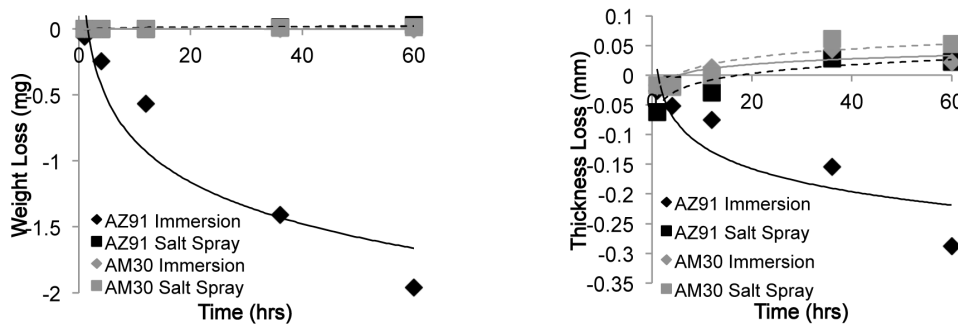


Figure 17. (a) Average weight loss and (b) average thickness loss of AZ91 and AM30 based on testing environment as a function of time. Notice that all surfaces followed logarithmic trends.

Figure 18(a) shows the pit number density over the five exposure times for the immersion and salt spray surfaces on AZ91 and AM30. The salt spray surfaces followed second-order polynomial trends, while the immersion surfaces followed linear trends. The AM30 salt spray surfaces showed the lowest amount of pit formation, while the AZ91 salt spray surfaces showed the highest amount of pit formation. Both immersion surfaces had pit number densities that were in between the pit number densities of the salt spray surfaces. Figure 18(b) shows the changes in the pit area, which is the 2-D area covered by the pits as seen by micrographs for the immersion and salt spray surfaces on AZ91 and AM30. AM30 experienced large pit area increases for both surfaces, while AZ91 experienced a small change in pit area. Figure 19(a) shows the changes in the nearest neighbor distance, which is the distance between two pits, for the immersion and salt spray surfaces on AZ91 and AM30. The as-cast AZ91 surfaces showed the smallest nearest neighbor distances while the extruded AM30 surfaces showed the largest nearest neighbor distance. Figure 19(b) shows the intergranular corrosion area fraction (ICAF), which is the fraction of the surface that shows the corrosion that occurs in the β -phase precipitate phase of the alloy, for the immersion and salt spray surfaces on AZ91 and AM30. AM30 experienced more intergranular corrosion than AZ91 for both environments.

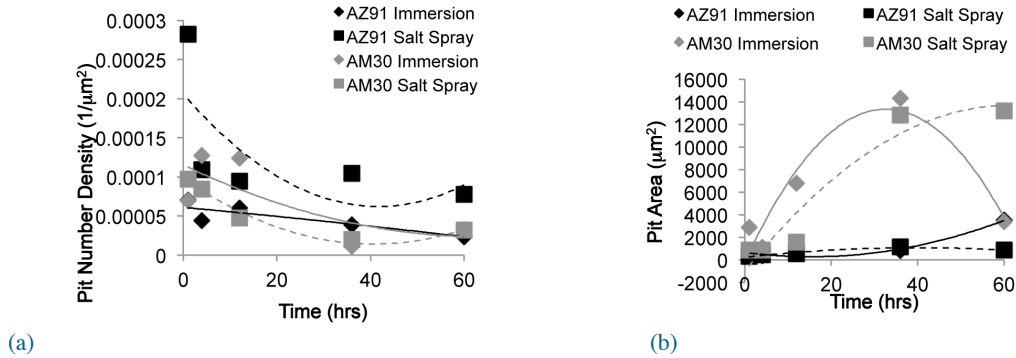


Figure 18. (a) Average pit number density and (b) surface area of AZ91 and AM30 based on testing environment as a function of time.

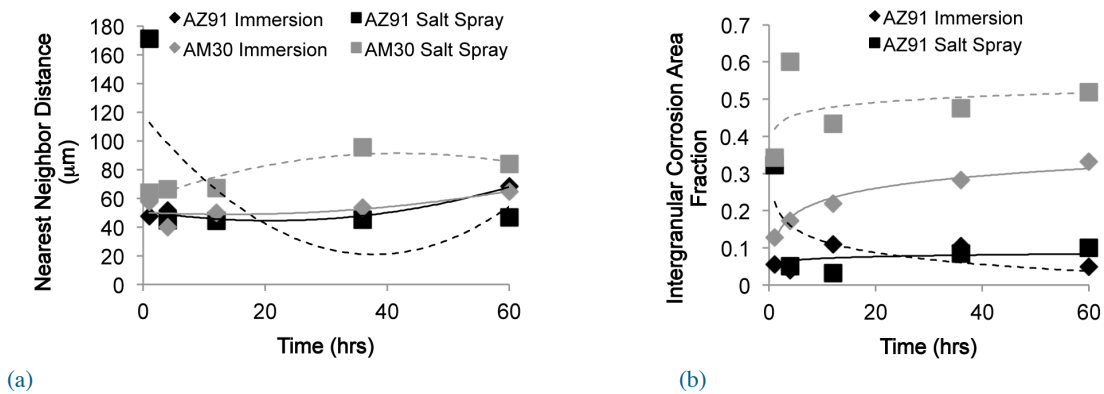


Figure 19. (a) Average nearest neighbor distance and (b) intergranular corrosion area fraction of AZ91 and AM30 based on testing environment as a function of time.

The differences in weight and thickness changes are attributed to the environment, where the salt spray allowed samples to gain weight, resulting in increased thickness and weight for both AM30 and AZ91. The continuous presence of water in the immersion environment allowed both alloys to lose weight. The differences in pit formation, nearest neighbor distance, and ICAF are the effect of the increased presence of Al (9% in AZ91, 3% in AM30) causing the formation of a galvanic cell that increased corrosion, thereby increasing pitting and intergranular corrosion. The pits grew more easily on AM30, though, because there was more Mg present, which degrades quickly in a saltwater environment thereby allowing the pits to grow in size.

1.9. Material Design of Lightweight Magnesium Alloys

Team Members: S.-G. Kim, S. Kim, A. Moitra, L. Lyanage

Accomplishments

Established the understanding of twinning nucleation of Mg alloys by employing molecular dynamic simulations.

Approach

Design a novel Mg alloy with improved formability and energy absorption, creep, and corrosion resistance for automotive use.

Results and Discussion

Twinning Nucleation in Magnesium

In atomistic dynamic simulations of Mg alloys with hexagonal close packed (HCP) crystals, we observed the nucleation of radially growing $\{10\bar{1}2\}$ twinning under tensile loading in a rectangular wire system without creating artificial twinning. The wire axis is along the x-direction, normal to the basal plane of the Mg crystal (see Figure 20). Tensile deformation was performed along the c-axis, parallel to the x-direction in Figure 20, which nucleated the $\{10\bar{1}2\}$ twinning. The twinning boundary on the $\{10\bar{1}2\}$ plane was initially spherical but became linear after deformation.

The twinning nucleation mechanism of Mg alloys is very different from the well-known twinning mechanism observed in face centered cubic (FCC) crystals; the Mg twinning nucleates from a point source rather than from a fault plane following the partial dislocation line in the FCC crystal. More details forthcoming in continued work under Phase IV.

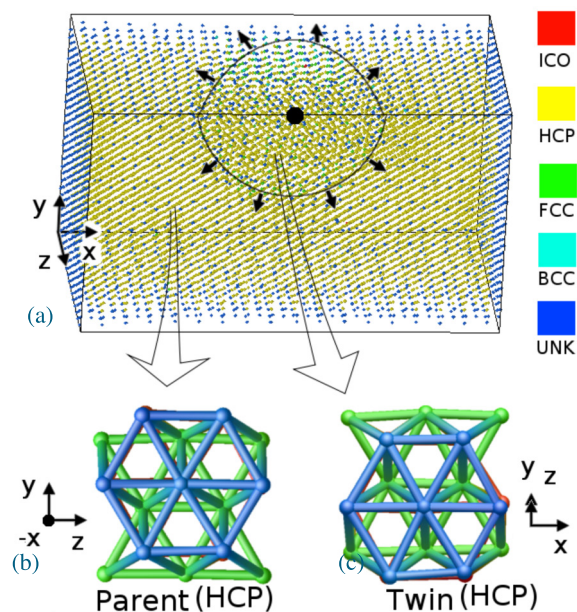


Figure 20. (a) Twinning nucleation and spherical growth of a twinning region from the middle of the edge plane as indicated by a black dot. The colors of atoms represent different atomic structures classified by Ackland method. The ICO represent icosahedral structure and the UNK unknown. The twinning structures are HCP indicated by yellow. (b) The structure of the parent is magnified and viewed from x direction. The basal plane of the parent is normal to x-axis. (c) The twinning region is magnified at specific viewpoints to show the basal planes of twinning. The colors in (b) and (c) represent the depth of structure.

1.10. Simulation-Based Design Optimization

Team Members: M. Rais-Rohani, K. Motoyam; Students: A. Najafi (PhD), M. Rouhi (PhD), C. Tamasco (MS), A. Parrish (MS), M. Kiani (PhD)

Accomplishments

- Investigated the influence of process-induced texture on energy absorption of square tubes.
- Developed a framework for coupled forming-crush simulation and optimization of sheet-formed tubes.
- Performed crashworthiness optimization of vehicle structures based on dummy responses.
- Performed uncertainty analysis of components made of nano-enhanced composite materials.

Results and Discussion

Influence of Texture on Crush Behavior of Square Tubes

To study the effect of process-induced texture on structural response, the crush behavior of polycrystalline metallic (FCC Al alloy) square tubes under constant rate axial loading condition was investigated through a mesoscale crystal plasticity model embedded in an explicit FE simulation code, ABAQUS/Explicit. The model accounts for crystal orientations and their effect on the flow rule, stress-strain response during loading, unloading, yielding, and hardening behavior (Marin, 2006). Two basic folding modes were simulated to investigate different localized regions that may form during the axial collapse of the tube. Due to computational limitations, each FE simulation was performed using 40 grains per element integration point to capture the crystal evolution information at each time step calculation (Najafi et al., 2011a).

To model different orientation patterns in the crystal structure, a single FE model was used to simulate the load path under basic loading conditions (i.e., uni-axial tension and compression and simple shear) encountered during the manufacturing process as shown in Figure 21. The initial random along with the three load-induced textures was then used to define the material model in crush simulations of square tubes with the assumption that the entire tube model has the same texture architecture. Crush tubes experience excessive distortions in the localized regions as they collapse, and since energy absorption is dominated by the plastic collapse mechanisms in the corner elements, the influence of texture and the evolution of grain orientation were expected to be significant.

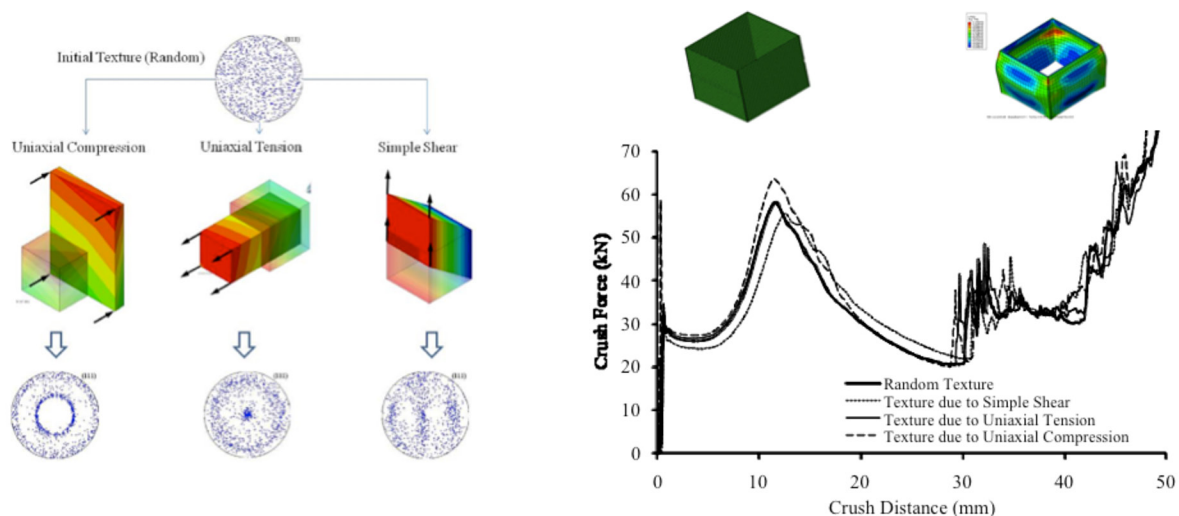


Figure 21. Different texture models and their impact on energy absorption of a square tube.

The simulation results (see Figure 21) show the effects of random and anisotropic texture on the overall energy absorption of the tube. It appears that texture due to uni-axial compression helps to increase the peak crush force in comparison to the random texture and anisotropic texture due to simple shear. Initially, the lowest curve is that of the tube with simple shear induced texture, but after the second peak, the curve for the random texture is the lowest one. The uni-axial compression shows better performance in overall energy absorption behavior compared with uni-axial tension. This conceptual study revealed that by controlling texture during the manufacturing process, the performance of the component can be enhanced.

Sequential Coupled Process-Performance Simulation and Optimization

In this study, sheet-forming simulation was coupled with crush simulation to investigate the effect of manufacturing process and product design parameters on energy absorption characteristics of thin-walled tubes as depicted in Figure 22. The coupled process-performance simulations were integrated with a multi-objective design optimization approach for finding the optimum process and performance responses. Geometric attributes including the cross-sectional dimensions as well as manufacturing process parameters such as holder force, punch velocity, and friction coefficient were treated as design variables. Rupture and thinning were measured based on the result of deep drawing simulation in ABAQUS/Explicit and the springback distortion was extracted from ABAQUS/Standard solver by including the residual stresses and dynamic and contact responses from deep drawing simulation. Energy absorption was measured by the mean and maximum crush force values from ABAQUS/Explicit simulation that included all the history variables from deep drawing and springback analyses. We investigated the sequential coupled simulation with both piecewise linear plasticity as well as Bammann–Chiesa–Johnson (BCJ) plasticity and addressed a number of critical issues that enabled the successful coupling of multiple simulations from start to finish while retaining key information such as residual stresses, plastic strains, thinning, springback, etc. and determination of their influence on crush performance (Najafi and Rais-Rohani, 2011; Najafi et al. 2011b). Surrogate models using radial basis functions were developed and used in multi-attribute process-performance optimization. Pareto optimal solutions were found and the sensitivity of process and performance responses to the selected design variables was evaluated.

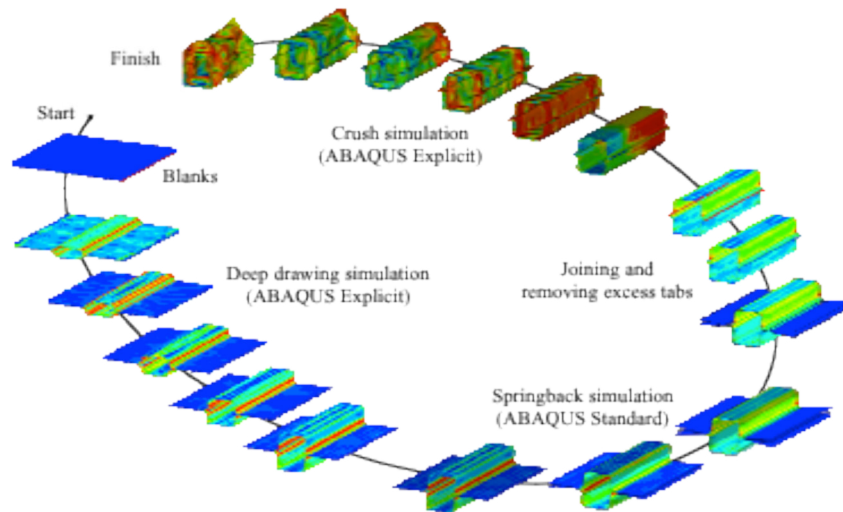


Figure 22. Sequential coupled forming-crush simulations of double-hat tubes.

1.11. Solidification Microstructure Modeling for Magnesium Alloy

Team Members: S. Felicelli, L. Wang; Students: T. Talukdar (MS), H. Yin (PhD-graduated), U. Sajja (PhD-graduated), R. Lett (PhD), M. Eshraghi (PhD), J. Coleman (UG), R. Johnson (UG)

Accomplishments

- Characterized microstructure of AZ91 Mg alloy for four different casting processes
- Evaluated reliability of A356 Al alloy plates produced with EGPS process
- Developed Lattice-Boltzmann model for solidification microstructure simulation
- Developed mushy-zone model with mesh adaptation for segregation defects
- Produced 5 refereed publications
- Graduated 2 PhD students

Results and Discussion

Microstructural and mechanical property data were generated from several control arm castings of Mg alloy AZ91 produced for the High Integrity Magnesium Automotive Components (HIMAC) project. The castings were made by four different processes: squeeze cast, low pressure permanent mold, T-Mag, and Ablation. Ten control arms were examined from each of the four casting groups. The microstructure, grain size, pore fraction, and pore size were measured with optical microscopy and image analyzer. Different types of defects were identified to evaluate the four casting processes. In order to explore the presence of oxide films, a series of four-point bend (FPB) tests were performed and the ultimate bending stress (UBS) was obtained. The mechanical properties of the castings were quantitatively evaluated for reliability using a two-parameter Weibull distribution function. A detailed metallographic analysis of the fracture surfaces of FPB samples was performed using SEM.

Figure 23 shows the UBS Weibull plots obtained for three of the casting processes. Since none of the Ablation samples was broken by the FPB tests, the Ablation process is not included in the Weibull plots. The Weibull moduli for the UBS are 7.93, 11.54, and 17.29 for Squeeze Cast, LPPM, and T-Mag, respectively. Dispersed shrinkage porosity and oxide film defects were observed in the Squeeze Cast samples, which in turn results in more scatter in FPB test results than in LPPM and T-Mag samples. The mean values of the UBS are 295.80MPa, 334.93MPa, and 352.84MPa, for Squeeze Cast, LPPM, and T-Mag, respectively. For the Ablation process, an average UBS level of 536.35MPa was reached before the sample bottomed out. These results indicate that, for the samples analyzed, the T-Mag and Ablation castings have better mechanical properties than Squeeze Cast and LPPM.

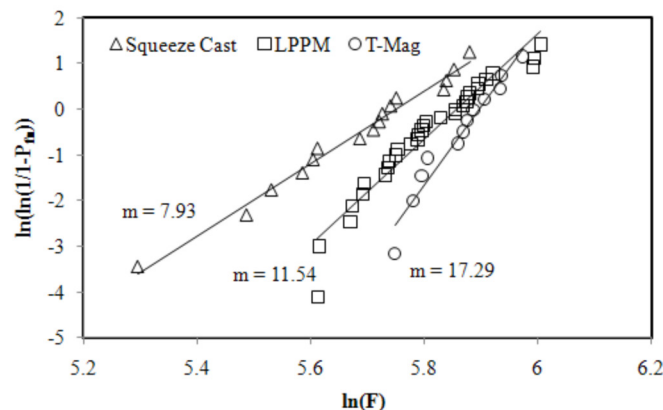


Figure 23. Weibull plot for UBS data of FPB tests for different casting processes.

Task 2 – Multiscale Materials Modeling and Characterization of Steel Alloys

Objective

Deploy and adapt current enhanced capabilities developed at CAVS in multiscale materials modeling and characterization to steel manufacturing, process optimization, and alloy design impacting the growth of regional economy and drawing regional/national/international company participation into education, services, and research on ferrous alloys.

Approach

Establish a set of small-scale steel material processing steps and computational capabilities in CAVS labs to simulate industrial casting and subsequent downstream processes. This research includes alloy design, computationally simulated and experimentally validated material models to understand process-structure-property relationship from solidification to downstream forming and heat treatment processes.

2.1. Materials Design of Steel Alloys

Team Members: S.-G. Kim, H. Rhee, S. Kim, A. Moitra, L. Lyanage

Accomplishments

- A new inter-atomic potential for Fe-C alloys was established and validated by cementite (Fe_3C).
- Experimental study of heat treatment of a dual-phase steel alloy is completed.

Results and Discussion

Modified Embedded Atom Method Potentials for Fe-C Alloys

Reliable Fe-C alloy potential is critically important in designing lightweight steel alloys. We developed a new Modified Embedded Atom Method (MEAM) potential for Fe-C alloys using the multi-objective optimization procedure based on the MEAM potentials for pure Fe and C (Kim, 2009). Our results show that this MEAM potential for an Fe-C alloy system reproduces materials properties of Fe-C alloys under various static loading conditions. We further validated this potential by applying it to determine the thermo-mechanical properties of cementite (Fe_3C). At the eutectic temperature, cementite becomes a solution of iron and carbon without a crystal structure. We performed a two-phase simulation using the newly developed Fe-C alloy MEAM potential to predict the eutectic point as shown in Figure 24.

In this simulation, a block of cementite was heated using an isothermal-isobaric ensemble, consisting of moles (N), pressure (P) and temperature (T) (NPT), molecular dynamic run to 1200 K. Then, we kept the

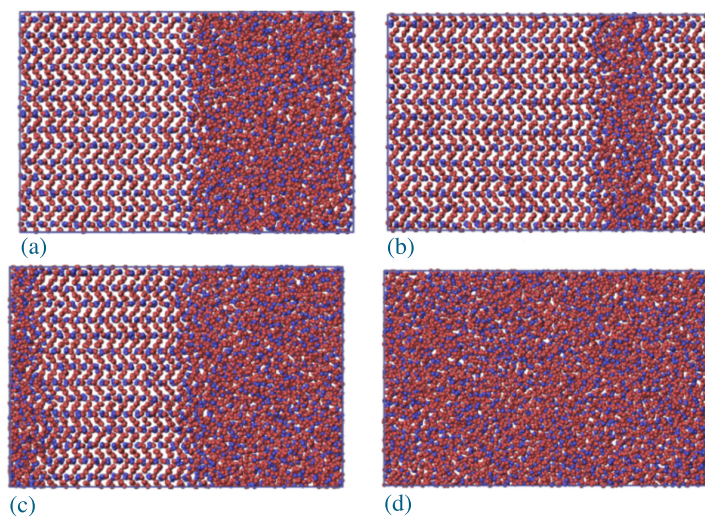


Figure 24. The snapshot of two-phase melting simulation of cementite: (a) the initial configuration; (b) two-phase cementite system at 1400 K at the end of the MD run. The liquid phase has been crystallized and the solid phase is spreading to the entire system; (c) the system at 1440 K. Both phases are persistent and the designation of the final phase is ambiguous; (d) two-phase cementite systems at 1450 K at the end of the MD run. The solid phase has been melted and the liquid phase is spreading to the entire system.

atoms in the left half of the system fixed at 1200 K positions while heating the atoms in the right half of the system to 4000 K causing a liquid phase of Fe and C to form. The initial configuration was completed when the right half was cooled down to 1500 K. This initial configuration was then heated from 1400 K to 1500 K in 10 K intervals using NPT molecular dynamic runs. Each system ran for 6.4 ns (32x105 MD steps). At a particular temperature, if the system was progressing towards the solid phase, the cementite was considered to be solid, whereas if it progressed toward the liquid phase, then at that temperature cementite was considered to be liquid. The total energy versus temperature and volume per atom versus temperature graphs are used to determine the melting temperature as shown in Figure 25. From these methods we can conclude that the eutectic temperature of cementite is between 1440 K and 1460 K. This is in excellent agreement with the experimental value of 1420 K.

Thermomechanical Treatment on DP Steels

We carried out heat treatments (i.e., intercritical annealing at selected temperatures followed by quenching in different quench media), structure observation, and mechanical tests (Figure 26) along with the fractographical study (Figure 27) on dual-phased (DP) steels to investigate the optimum heat treatment conditions to obtain the desired combination of mechanical properties by modifying volume fractions of constituent phases.

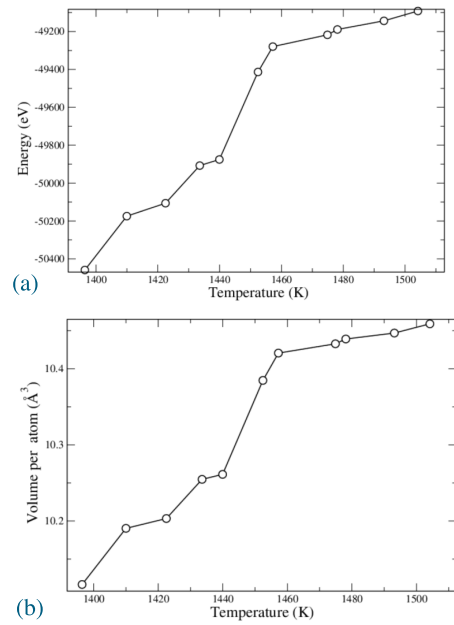


Figure 25. (a) Energy vs. temperature plot and (b) volume vs. temperature plot for two-phase simulation of cementite

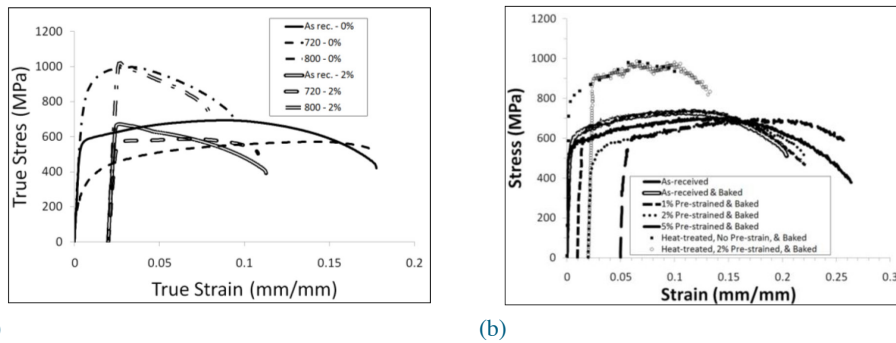


Figure 26. (a) Stress versus strain curves comparing as-received and heat-treated DP 590 steels with 0% and 2% pre-strains. All specimens were baked following pre-straining. (b) Stress versus strain curves obtained from high strain-rate Hopkinson bar tests in tension on non-heat treated and heat treated (i.e., ice brine quenched from 800°C) specimens with various pre-straining and baking protocols.

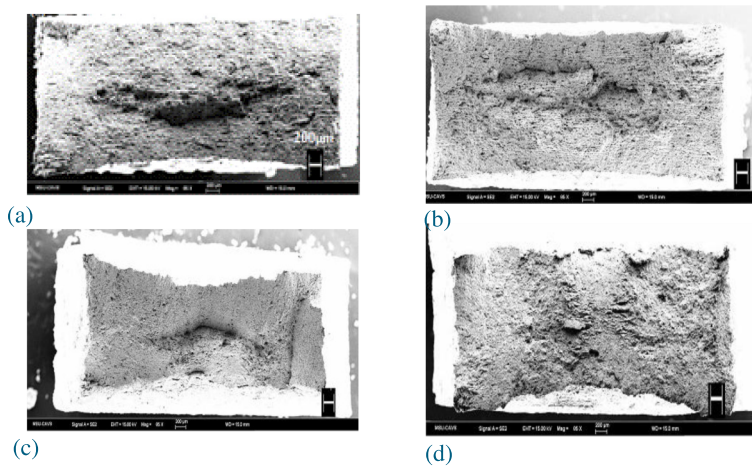


Figure 27. SEM fractography on the specimens heat treated at different annealing temperatures followed by quenching prior to the tensile tests; (a) 720°C annealed followed by 0% pre-strained and baked, (b) 720°C annealed followed by 2% pre-strained and baked, (c) 800°C annealed followed by 0% pre-strain and baked, (d) 800°C annealed followed by 2% pre-strain and baked.

2.2. Solidification and Phase Transformation in Steel Alloys

Team Members: S. Felicelli, L. Wang, Students: T. Talukdar (MS), H. Yin (PhD-graduated), U. Sajja (PhD-graduated), R. Lett (PhD), M. Eshraghi (PhD), J. Coleman (UG), R. Johnson (UG)

Accomplishments

- Simulations of laser deposition processes of Cu-H13 and H13-H13 samples were performed. The thermo-mechanical model is capable of describing thermal history of layers deposited and residual stress.

Results and Discussion

A three-dimensional thermo-mechanical finite element model was developed to simulate the temperature history and residual stress in a Copper (Cu)-H13 sample (H13 powder on a solid Cu substrate) deposited by the LENS® process. The laser power and scanning speed along with two different scanning strategies were optimized to obtain a pre-defined molten pool size for each layer. The temperature history and cooling rates obtained from the thermal analysis were used for the residual stress analysis in the built part. In order to verify and compare the results, the model was also applied to a H13-H13 sample (H13 powder on a solid H13 substrate). Different distributions of residual stress, depending on different material samples, scanning speeds and scanning strategies, were considered. The simulated stress distributions were compared with the available experimental results in literature.

A comparison of laser power density for Cu-H13 and H13-H13 samples is shown in Figure 28. It is observed that a large amount of laser power is needed for the first layer of Cu substrate in comparison to the H13 substrate and the difference gradually decreases with subsequent layers. Higher thermal conductivity of Cu substrate causes rapid heat loss through the substrate and hence, results in higher power requirement to maintain the steady molten pool size during the deposition of the first layer. However, for subsequent layers, the previous layers act as a barrier to heat conduction to the substrate which, in turn, reduces the difference of required laser power for Cu-H13 and H13-H13 samples.

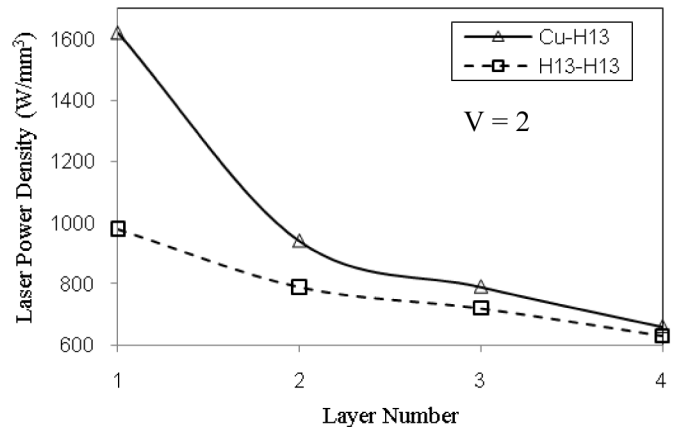


Figure 28. Laser power density for Cu-H13 and H13-H13 samples for both alternative and unidirectional scanning strategies.

Task 3 – Multiscale Material Models and Processing Design for Polymeric Materials

Objective

Develop a multiscale ISV model and specific processing models for polymeric materials that account for statistical variations from the material microstructure, product geometry, and processing parameters and that can aid in the design of polymeric materials for automotive applications. Four main groups of materials will be investigated in this task: 1) Thermoset resins; 2) Nanocomposites and carbon fiber composites; 3) Natural fiber composite products from kenaf bast fiber; 4) Soft biological tissues and animal outer armor.

Approach

We will develop a material database, ISV material models, and process models for different groups of non-metallic materials. The material model will be developed using a multiscale modeling approach, where information from molecular dynamics simulations are to be used to provide insights into the functional form of the ISV's evolution equations and corresponding material parameters.

3.1. Material Models for Polymeric Materials

Team Members: J.-L. Bouvard, S. Nouranian, M.T. Tschopp

Accomplishments

- Molecular dynamics (MD) simulations on amorphous polyethylene under tension were established to understand how chain structure changes contributed to the material response during deformation of crosslinked polymers.

Results and Discussions

An ISV material model has been developed to capture the time- and temperature-dependent mechanical behavior of thermoplastics (Bouvard et al., 2010). The model is being modified to simulate the mechanical behavior of thermosets at different strain rates, stress states, and temperatures. The development follows current methodologies typically used for metals and departs from the typical spring-dashpot representations widely used in the polymer modeling. The main purpose of the ISV model is to develop a physics-based model in a thermodynamic framework.

MD simulations were carried out on amorphous polyethylene under tension to understand how non-bonded van der Waal's interactions, bond stretching, bond bending, and bond torsion portions of the polymer chain energy contribute to the material response during deformation (Figure 29). This information was used to define the ISVs of the material model and their corresponding evolution equations.

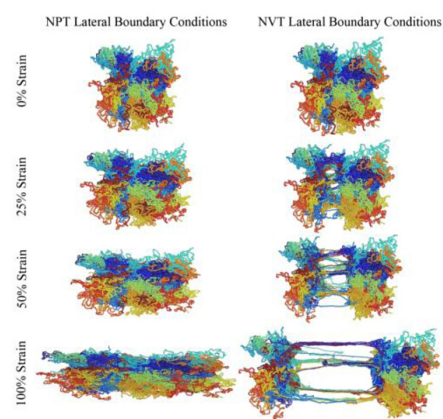


Figure 29. Polyethylene structure evolution for the NPT and NVT lateral boundary conditions at 0%, 25%, 50%, and 100% strain. Colors represent different chains.

3.2. Structural Nanocomposite Design

Team Members: T. Lacy and students

Accomplishments

- Established the framework of multiscale material model for a nanocomposite material;
- Critical information to bridge material scales has been investigated and results look encouraging.

Results and Discussion

MD simulations were performed to assess both pristine (Nouranian et al., 2011) and oxidized (Jang et al., 2011) vapor grown carbon nanofiber (VGCNF) surface effects on liquid vinyl ester (VE) monomer distributions. The VE was composed of styrene and two monomers with one and two bisphenol-A groups in their backbones, VE1 and VE2, respectively. Temporally and spatially averaged relative monomer concentrations, calculated in a direction away from the graphene surfaces, were monitored. The relative styrene, VE1, and VE2 distributions near the oxidized nanofibers surface were profoundly different

from those for a pristine (unoxidized) VGCNF. To illustrate these differences, the relative concentration ratios of styrene/VE1, styrene/VE2, and VE1/VE2 were compared for both oxidized and pristine VGCNF surfaces at equilibrium (Figure 30). Lower styrene and higher VE1 concentrations were observed near the oxidized VGCNF surfaces. This could lead to a stiffer interphase than the one near the pristine VGCNF surfaces after resin curing. This significant difference in VGCNF/VE interphase properties affects the effective nanocomposite bulk properties calculated at the micro- and meso-scales by the micromechanical models.

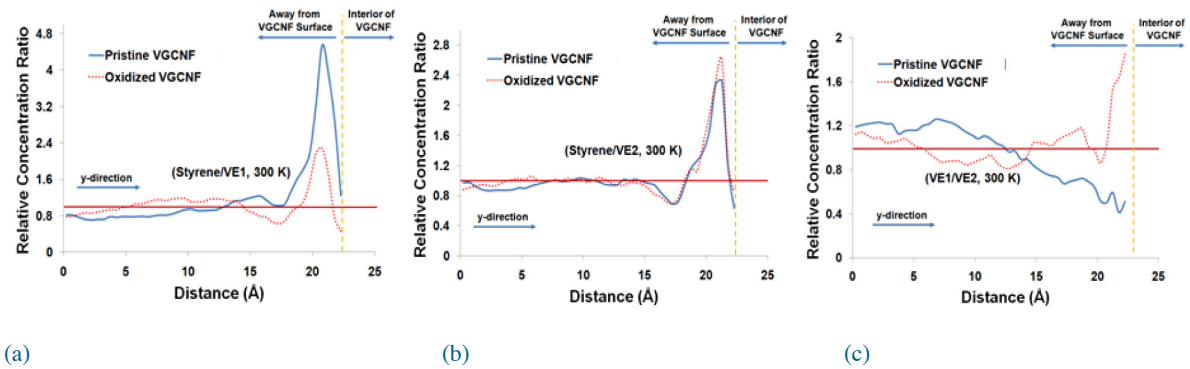


Figure 30. (a) Relative styrene/VE1 concentration ratios, (b) relative styrene/VE2 concentration ratios, and (c) relative VE1/VE2 concentration ratios at 300K along the y-coordinate of the simulation cell for pristine versus oxidized graphene sheets.

A parametric study was performed using the Effective Continuum-Micromechanics Analysis Code (EC-MAC) to investigate the effects of solid/hollow nanoreinforcement geometries, distinct elastic properties, and voids on various nanoreinforcements and polymer matrices. While there was a fair degree of scatter in the measured moduli (Zhang et al., 2006), Figure 31(a) shows that the two micromechanical solutions reasonably matched the mean experimental responses over a range of volume fractions for solid silica nanosphere/epoxy and hollow glass sphere/polyester composites. Similar effective property estimates (Figure 31(b)) were obtained for composites comprised of hollow glass nanospheres in a polyester matrix. In contrast to the case involving solid silica nanospheres, the effective moduli decreased with increasing volume fractions of hollow glass spheres because of the relatively low fraction of solid glass contained in each sphere. The predicted moduli correlated reasonably well with the experimental data obtained from Huang and Gibson (1993). The predicted effective moduli for a polyester matrix containing spherical voids only (i.e., no glass outer wall) fell significantly below the measured and predicted values for the hollow glass sphere/polyester composites (Figure 31(b)). This suggests that the very thin glass outer wall significantly contributes to the overall composite properties.

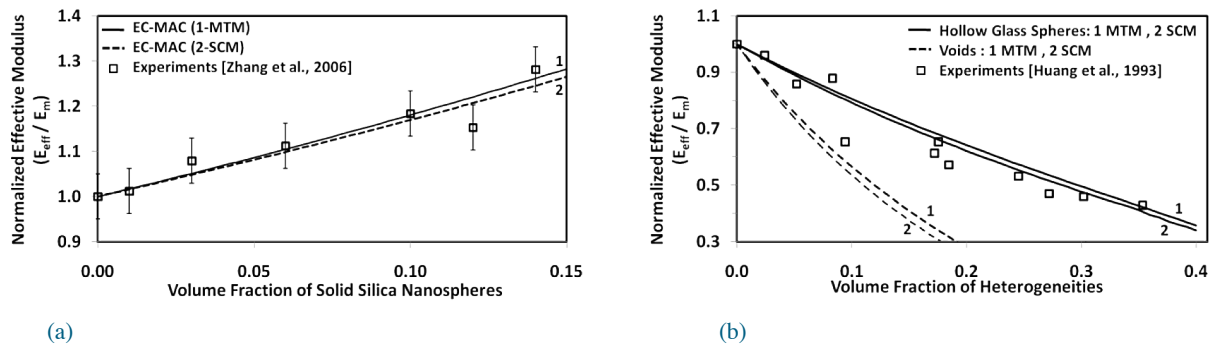


Figure 31. Measured and predicted effective elastic moduli for (a) solid silica nanosphere/epoxy and (b) hollow glass sphere/polyester composites and a polyester matrix containing spherical voids.

Figure 32(a) contains a plot of the effective moduli of α -ZrP nanoplatelet/epoxy nanocomposites containing randomly oriented nanoplatelets with different aspect ratios ($D_p / t_p = 100, 1000$). The predicted solutions fell within the error band of the measured values from Boo et al. (2007), while, in both cases, they slightly over-estimated the mean experimental responses. Figure 32(b) contains a plot of the effective moduli for composites containing randomly oriented, wavy, hollow nanofibers with voids, where the void volume fraction was increased as either a linear ($c_v = c_f$) or a quadratic function of

the nanofiber volume fraction ($c_v = 500.0 \cdot c_f^2$). For the latter case, the estimated moduli matched the observed values from Lee (2010) and the predicted moduli captured the essential nonlinear character of the experimental data (Figure 32(b)). At higher VGCNF volume fractions, the measured composite stiffness values were somewhat insensitive to further increases in nanofiber content. Hence, variations in the effective volume fraction of VGCNFs may not significantly influence the composite elastic properties, but could have a profound impact on strengths.

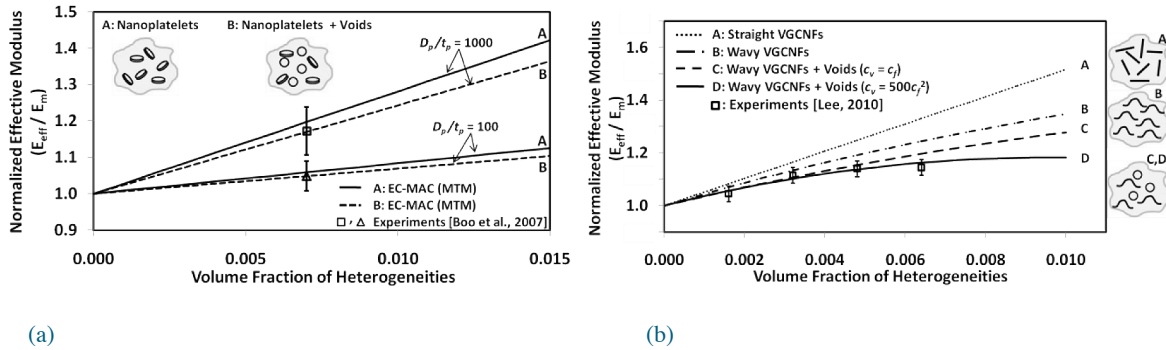


Figure 32. Measured and predicted effective elastic moduli for (a) α -ZrP nanoplatelet/epoxy composites containing nanoplatelets ($D_p / t_p = 100, 1000$) and voids ($c_p = c_v$) and (b) VGCNF/VE nanocomposites containing wavy nanofibers and voids ($c_v = c_f, c_v = 500.0 \cdot c_f^2$).

Conclusions

This study helps to facilitate the development of engineered multiscale materials design by providing insight into relationships between nanomaterial fabrication/processing, chemical and physical characteristics, and interaction and evolution of structure across disparate spatial and temporal scales that lead to improved macroscale performance. A crucial aspect of this work is the establishment of appropriate handshake protocols for efficient data transfer between multiscale calculations performed over a series of fundamentally distinct spatial scales.

3.3. Natural Fiber Composites for Structural Component Design

Team Members: S. Q. Shi, K. Liang, J. Wang, T. Tang, M.T. Tschopp, Students: Y. Shen (MS), W. Che (MS), E. Zhang (MS)

Accomplishments

- Vinyl tris (2-ethoxymethoxy) silane treatment of kenaf fiber was conducted. By such treatment, the water absorption and flexural properties of the resulting kenaf fiber composites were significantly improved.
- A micromechanics modeling framework, Variational Asymptotic Method for Unit Cell Homogenization (VAMUCH), was developed to investigate the moisture absorption process in natural fiber composites.
- Amorphous cellulose models were successfully created with the use of ReaxFF. Preliminary molecular dynamic simulations have been developed for the amorphous cellulose.
- Principles and practices of life-cycle assessment (LCA) were used to evaluate environmental performance of natural fiber reinforced bio-resin matrix composites. Preliminary results indicated their superiority in environmental performance to a traditional glass fiber polymer composite.

Results and Discussion

The water absorption of silane treated kenaf fiber composites decreased by 22% compared to untreated fiber composites. After a four-week water immersion, the water absorption of silane treated kenaf fiber composite was about stable, while that of untreated kenaf fiber composites still increased (Figure 33(a)). The hydrophilic nature of kenaf fiber was reduced and hence the water resistance of the resulting fiber composites was improved after silane treatment of kenaf fiber. Compared to the untreated fiber composites, the flexural strength and modulus of silane treated kenaf fiber composites increased by 25% and 8%, respectively (Figure 33(b)). Silane treatment of kenaf fiber improved the mechanical properties of the resulting fiber composites.

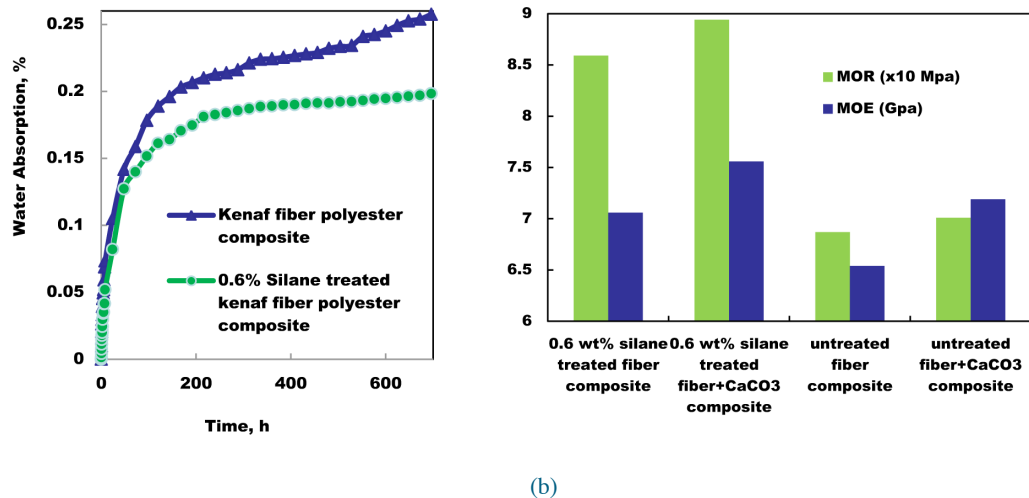


Figure 33. (a) Water absorption of treated and untreated kenaf fiber composites and (b) Flexural properties of treated and untreated kenaf fiber composites.

Figure 34 shows how the tensile loading leads to a net change in the shape of the cell, where the colors represent the different atom types (C, H, O). To investigate the deformation behavior of the cellulose, the stress-strain behavior, temperature dependence, and internal energy evolution were monitored as a function of deformation. Figure 35 shows the stress-strain behavior for amorphous cellulose at a strain rate of 10^{10} s^{-1} . The red dots are stress values taken at various strain levels and the black line is the averaged response; this scatter is typical of polymer deformation in molecular dynamics. After an initial elastic regime, yield occurs and then strain hardening is observed. The green and blue dots (mainly hidden behind green dots) represent stresses in the directions lateral to the loading direction – these are centered about 0 GPa, a boundary condition indicative of the uniaxial tensile load applied. This stress-strain curve is similar to previous simulations in the literature as well as experimental results (Chen et al., 2004).

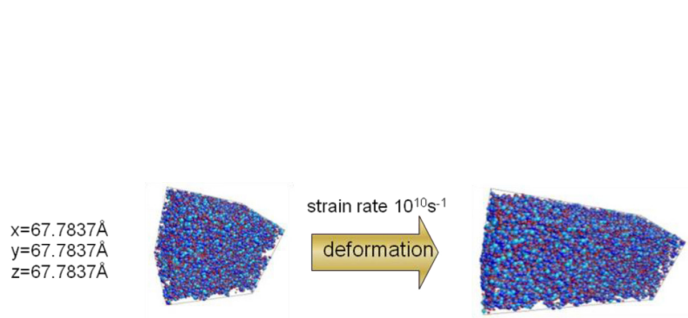


Figure 34. The model system in equilibrium at 100K and after being uniaxially deformed. Colors represent different atom types being simulated (C, H, and O)

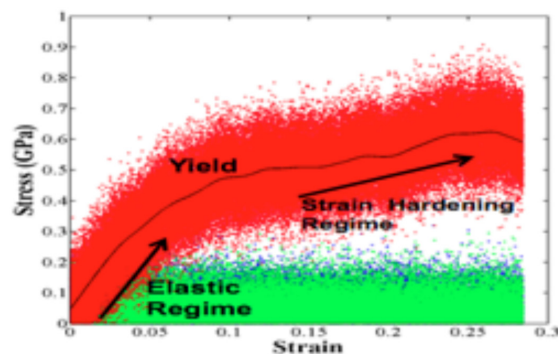


Figure 35. A characteristic stress-strain curve for amorphous cellulose (28,404 atoms, 100 K temperature 10^{10} s^{-1} strain rate). Black line is the average stress response in the tensile direction. Red, green, and blue dots show the scatter of the instantaneous stresses, the loading direction, and two lateral directions respectively.

Figure 36 shows the contour plots of moisture concentration flow flux in y_2 direction at 100 s, respectively, when the water concentration C_a is kept constant as 10 g/mm^3 . To quantitatively describe the moisture concentration flow flux, we plotted the distribution of y_2 direction along the vertical center line of unit cell at different time, as shown in Figure 37. It can be seen that the moisture concentration flow flux decreased with time since the gradient of moisture concentration, which is the driving force for moisture diffusion, decreased with time.

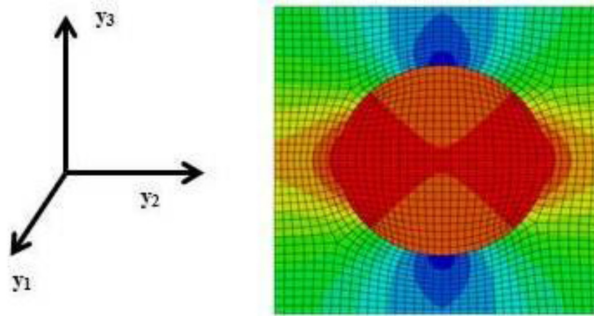


Figure 36. Finite element model for the analysis of the global transient moisture diffusion process.

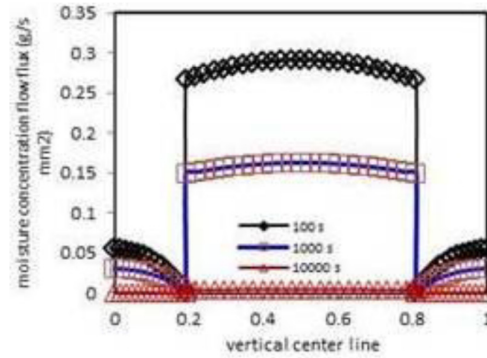


Figure 37. Distribution of moisture concentration along the horizontal center line at different time.

Figure 38 indicates that kenaf fiber has less negative environmental impact than glass fiber during a period from raw materials extraction to fiber manufacturing. Figure 39 shows that bast fibers consume less energy than other fibers in manufacturing 1-kg fibers. Wood pulp and bast fibers consume less non-renewable energy. Method to calculate Cumulative Energy Demand was based on the method published by Ecoinvent version 2.0 and expanded by PRé Consultants for raw materials available in the SimaPro 7 database. Figure 40 demonstrates that natural fibers achieved overall lower environmental burdens. Land uses contributed substantial portions for agri-fibers (jute and kenaf). The scale is chosen in such a way that the value of 1 point is representative for one thousandth of the yearly environmental load of one average European inhabitant. The key environmental measures for three product scenarios were computed with Simapro software and are shown in Figure 41. Negative means carbon credit, i.e. saving non-renewable resources otherwise being used. Both kenaf-fiber reinforced SMCs perform better than glass fiber SMC in every environmental category. The global warming potential of the kenaf fiber SMC could be only about 45% of that for the glass fiber SMC.

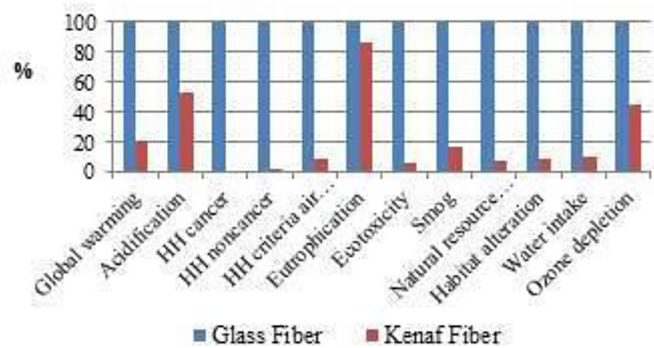


Figure 38. Comparison of environmental impacts of fiber productions. BEES impact indexes are selected as characteristics.

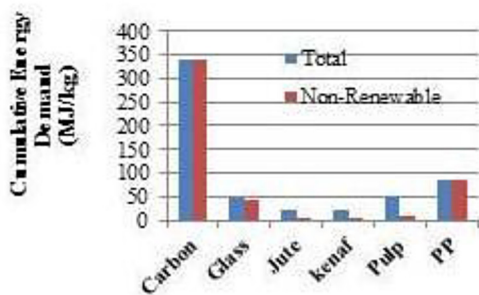


Figure 39. Cumulative energy demands of typical fiber productions (per 1 kg fiber)

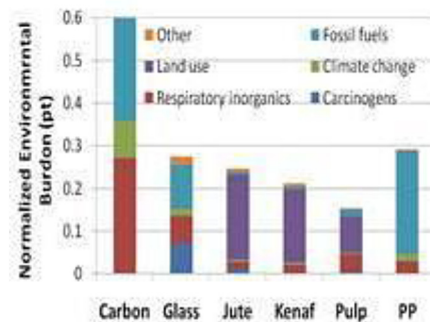


Figure 40. Weighted environmental points for typical fiber productions (per 1 kg fiber)

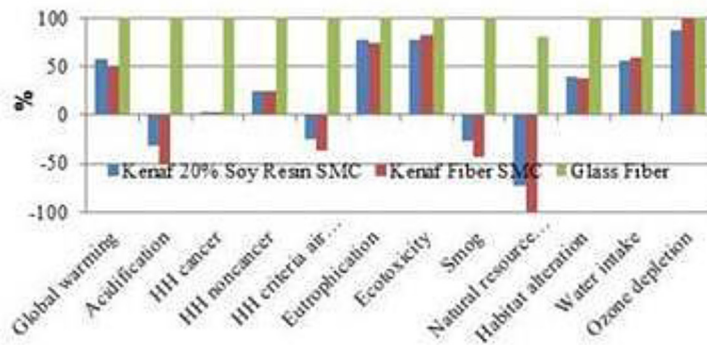


Figure 41. BEES environmental impacts of manufacturing three fiber reinforced polymer composites (per functional unit).

Technology Transfer Path

Life-cycle thinking and assessment is a great marketing and educational tool to promote bioproducts applications.

Conclusions

Vinyl tris (2-ethoxymethoxy) silane treatment of kenaf fiber improved the physical and mechanical properties of the resulting kenaf fiber composites. The water absorption of silane treated kenaf fiber composites decreased by 22% compared to untreated fiber composites. And the flexural strength and modulus of silane treated kenaf fiber composites increased by 25% and 8%, respectively. The simulated stress-strain behavior using molecular dynamics showed similar trends both qualitatively and quantitatively as those observed in the experimental testing for amorphous cellulose. The multiscale model of moisture absorption process of natural fiber composites was developed on the basis of the theoretical framework of VAMUCH. The LCA preliminary result demonstrated that the use of modified soybean oil and natural fiber to make sheet molding compound had a great potential from an ecological point of view.

3.4. Bio-inspired Design

Team Members: L. N. Williams, J. Liao, H. Rhee, Y. Mao, R. Prabu, S. Patnaik, S. Ryland, N. Lee

Accomplishments

- Thorough evaluation of skin, liver, tendon, and lung mechanics
- Robust and realistic finite element meshes of human head, heart, and liver were constructed
- A basic framework for finite element simulation of human head under blast loads was developed, which could potentially be adapted to other tissues and organs
- Materials/mechanical properties tests were performed and structure-property relations were investigated of the turtle shell, armadillo shell, rams horn, bream teeth, and woodpecker beak
- Computational modeling and simulations were carried out on mechanical test results obtained from turtle shell carapace

Results & Discussion

A human head FE model was developed and simulated under blast range Boundary Conditions (BCs). A three-dimensional realistic human head FE mesh, consisting of scalp, skull, intracranial cavities, and brain, was generated from the cryosections of the human head (Visible Human Project®, NIH). An ISV based constitutive model, MSU TP Ver. 1.1 (Bouvard et al., 2010), calibrated to the brain tissue high strain rate experimental data (Prabhu et al., 2011), was used for the brain parenchyma. Pressure-based BCs, obtained from Mouritz's work (2001) on underwater explosions, were applied at various distances from the human head mesh during FE simulations. The results from our FE simulations show that the stress state during a blast was highly non-uniform (Figure 42), with concentrated regions of peak positive and negative pressure values at the coup and countercoup sites. Further, the FE simulations also showed that the interaction of shock waves with the skull, cerebro-spinal fluid and brain played a key role in the nature of the blast related Traumatic Brain Injury (bTBI).

Quasi-static tests of porcine patellar tendon revealed that the tissue is stiffer in compression and stiffness increases with increasing strain rate. A clear difference in the material behavior is seen between the three different strain rates and thus strain rate dependency is achieved.

The compressive stress-strain response for armadillo shell, turtle shell, and ram horn at various strain rates is provided in Figure 43. Compression test results revealed a typical deformation behavior of cellular solids showing three distinctive regions: an initial linear elastic deformation, a plateau of deformation, and another period of near linear deformation with a fairly high modulus. The favorable deformation mechanisms of these materials in compressive conditions can be explained by those of synthetic foams found elsewhere (Gibson and Ashby, 1988; Rhee et al., 2009). The three materials showed varying levels of strain rate dependence. The ram horn gave the highest strain rate sensitivity, while the armadillo and turtle shell showed the considerably strain rate dependence. The Young's modulus for each material increased with increasing strain rate, which is a typical phenomenon among polymeric materials. When loaded at a low strain rate, the molecular chains have sufficient time to adjust to the imposed stress and the modulus value is lower than for the case where the same material is loaded at a higher strain rate (Goble and Wolff, 1993).

The TEM images of woodpecker beak reveal wavy lines at the keratin cell boundary, which has a role of energy absorption in cranial bone (Jaslow, 1990). Suture morphology relates to the load, especially compressive loads, and arrangement of the fibers in the suture (Krauss et al., 2009). Thus, this wavy line is also assumed to have the energy absorption role at the tip of the woodpecker beak. The result of the nano-indentation testing shows that the interior bony part of woodpecker beak is about two or three times harder than keratin shell. Hard interior material is assumed to be responsible for greater impact absorbing capabilities.

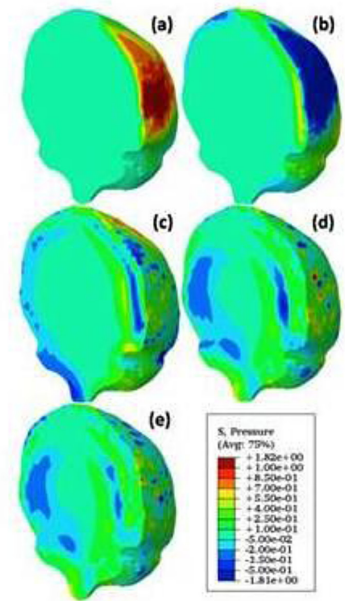


Figure 42. Sagittal view of the brain with pressure contour snapshots at (a) 125, (b) 163, (c) 224, (d) 316, and (e) 355 μ s.

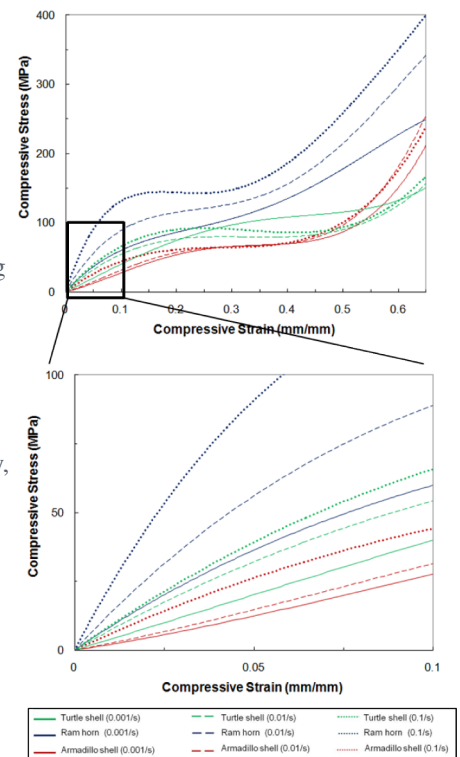


Figure 43. Compressive stress-strain response for turtle shell, armadillo shell, and ram horn for strain rates of 0.001, 0.01, and 0.1/s.

Task 4. K-12 Outreach Program

Team Members: M. Horstemeyer, R. Cuicchi

Objective

Development of a K-12 program (Mission Eggcellence) that communicates the importance of crashworthiness and safety issues in design and construction of vehicles through the utilization of a “Car Crash Curriculum” to educate K-12 teachers and students through teacher workshops and student competitions.

Approach

Create a grade appropriate curriculum with experiments and problems associated with the Physics of car crashes for grades K-2, 3-5, 6-8, and 9-12. Develop a Teacher Workshop and supply equipment to train grades K-12 teachers for use of the grade appropriate curriculum in the regular classroom. Design a competition for grades K-2, 3-5, 6-8, and 9-12 incorporating bumper design for passenger safety. Design a competition for grades K-2, 3-5, 6-8, and 9-12 incorporating car design for passenger safety.

Accomplishments

- Created a grade appropriate curriculum with experiments and problems associated with the physics of car crashes for grades K-2, 3-5, 6-8, and 9-12.
- Developed a Teacher Workshop for grades K-2, 3-5, 6-8, and 9-12 teachers for training in use of the grade appropriate curriculum in the regular classroom. Equipment necessary to conduct the experiments and compete in the competitions is given to each teacher participant.
- Design a competition for grades K-2, 3-5, 6-8, and 9-12 incorporating bumper design for passenger safety.
- Design a competition for grades K-2, 3-5, 6-8, and 9-12 incorporating car design for passenger safety.
- The Automotive Engineering Society’s “A World in Motion” program is in the process of adopting the Mission Eggcellence Program.

Results and Discussion

Contributions to the Long-term and Sustainable Engagement of the Team/Unit

MSU is developing an “Automotive Experience” strategic program that includes K-12, undergraduate work, and graduate level work. A new course and certificate are being developed in real time for this endeavor.

Thirty-three school districts in 30 counties have had 207 teachers participate in the teacher workshops. Eight hundred ninety-seven students have competed in the student competitions. Seventy-nine percent of the teachers who attended the workshop had students compete in both the bumper design and car design competitions.

We are being adopted by Automotive Engineering Society’s “A World in Motion” program to broaden the program further. Nissan North America (Canton, MS) and Vista Engineering Inc. have both donated in-kind contributions to the SRCLID program with specific interest in the educational development aspects of the program.

Conclusions

The Mission Eggcellence Program has been developed for the grades K-2, 3-5, 6-8, and 9-12. The Teacher Workshop for these grades has been very successful. Feedback was excellent.

Technology Assessment

Fundamental investigation of magnesium alloys including twinning nucleation, recrystallization, and fracture by utilizing the approach of multiscale material models and critical experimentation as demonstrated by this project has paved the road toward alloy design of Mg alloys with specific attributes and cost in mind. In the next three to five years, this program will provide significant impact to industry as a knowledge hub in materials design, via cyberinfrastructure, for automotive applications.

Conclusions

The Southern Regional Center for Lightweight Innovative Design (SRCLID) is dedicated to developing multiscale material models in conjunction with critical lab-scale experiments to characterize the microstructures and properties of several lightweighting materials (i.e., Al, steel, and Mg alloys) throughout their respective manufacturing and life cycle histories. We will then test these materials in crash simulations and safety performance evaluations. These materials are crucial to ongoing and critical demands for increased energy efficiency and safety performance in modern automotive designs, and the results of this research will facilitate their optimization for these applications.

Our Mg research team is focusing on generating PSP relationships for a number of Mg alloys, where a physics-based multiscale ISV model including uncertainty has been developed and validated in the lab-scale extrusion and post forming processes. Both sheet forming and extrusion teams have been actively engaged in Mg demo projects to validate and predict PSP relationships at the component level. The MSF Model has been correlated with several Mg alloys in terms of strain-life curves and extended to describe FSSW joint behavior. Our steel research team has established a number of atomistic potentials (i.e., Fe, C, Si, Al, Mg) that will be used in development of advanced high strength steels. The polymer team's efforts include research in natural fiber, polymeric materials, biomechanics, and nanocomposites. The natural fiber program has produced high quality samples for evaluation and the feedback was positive. The biomechanics program has advanced to the levels of incorporating polymeric ISV models for tissues and evaluating damage phenomena for brain subject to high rate impact. The composites effort has been developing multiscale material models to describe process/product concepts. Our Cyberinfrastructure has integrated our own proprietary software, external software, and experimental information into wiki and has garnered high recognition from TMS and USAMP. In conjunction with the development of multiscale internal state variable models, our design team has established optimization methods, including ISV and PSP within the design methodology. We have produced a number of high quality students and graduated 12 students with MS and PhD degrees. For the K-12 program, we have developed crash kits and run K-2 and 3-6 grade "Mission Eggcellence" competitions in multiple counties throughout Mississippi in an effort to inspire young students' interest in science and engineering.

In our industrial partnership development, we continue to establish strong ties with companies from various sectors (i.e., automotive, software, and manufacturers) throughout the world and they have embraced the technology being developed in this program. We received multiple-year cost sharing support from several companies: Alpha Star, SAC, POSCO, Mitsubishi Motors, Ftech, Genesis, Smart Aluminum, and Simufact. As the result of extensive interaction with these sponsors, we have met the cost share requirement for the program.

In order to commit a strong support role to the ICME program, we initiated a "Predictive Design Symposium" at MSST in June 2011 to share the progress of the SRCLID program with world-renowned scientists and industrial sponsors. Plans are for this symposium to be held every two years at MSST's campus. In order to demonstrate the deployment of building-block technology being developed in various tasks, we have actively engaged our Mg-focused research teams with USAMP members in the MFERD and HIMAC projects. The team has been developing detailed predictions of process structure-property relationships for a front-end Mg subsystem. The subsystem is composed of cast, extruded, and sheet-bended components. We have used our ISV, HCP crystal plasticity, extrusion process, and fatigue models from Tasks 1-6 to predict the state of microstructure (i.e., twinning, textures, strength) and mechanical behavior of the subsystem.

We will continue to develop the process-structure-property relationships and high fidelity material models for lightweight materials with a focused effort to demonstrate the technology through the Mg front-end project sponsored by the DOE. Composite, biomechanics, and natural fiber research teams will move forward to develop material specific multiscale models, validate them with critical experiments, and assess their cost structures. With the new data generated, we will employ these materials in crash simulations. We will continue to update the cyberinfrastructure and work to extend its national and international user base. We will also seek further support and form additional alliances with southern regional OEMs where the global technology community is within our reach.

References

Bammann, D.J.; Chiesa, M.L.; Horstemeyer, M.F.; Weingarten, L.I. Failure in Ductile Metals using Finite Element Methods. In *Structural Crashworthiness and Failure: Proceedings of the Third International Symposium on Structural Crashworthiness Held at the University of Liverpool, England, 14-16 April 1993*; Jones, N., Wierzbicki, T., Eds.; Taylor & Francis: Oxon, 1993, pp. 1-45.

Bisanda, E.T.N.; Ansell, M.P. The Effect of Silane Treatment on the Mechanical and Physical Properties of Sisal-epoxy Composites. *Composites Science and Technology* 1991, 41, pp. 165-178.

Boo, W.J.; Sun, L.; Warren, G.L.; Moghbelli, E.; Pham, H.; Clearfield, A.; Sue, H.J. Effect of Nanoplatelets Aspect Ratio on Mechanical Properties of Epoxy Nanocomposites. *Polymer* 2007, 48, pp. 1075-1082.

Bouvard, J.L.; Ward, D.K.; Hossain, D.; Marin, E.B.; Bammann, D.J.; Horstemeyer, M.F. A General Inelastic Internal State Variable Model for Amorphous Glassy Polymers, *ActaMech* 2010, 213(1), 71-96.

Brown, D.W.; Jain, A.; Agnew, S.R.; Clausen, B. Twinning and Detwinning During Cyclic Deformation. *Materials Science Forum* 2007, 539-543, pp. 3407-3414.

Chen, W.; Lickfield, G.C.; Yang, C.Q. Molecular Modeling of Cellulose in Amorphous State. Part I: Model Building and Plastic Deformation Study. *Polymer* 2004, 45(3), pp. 1063-1071.

Corbiere-Nicollier, T.; Gfeller Laban, B.; Lundquist, L.; Leterrier, Y.; Msnson, J.A.E.; Jolliet, O. Life Cycle Assessment of Biofibres Replacing Glass Fibres as Reinforcement in Plastics. *Resources, Conservation and Recycling* 2001, 33, pp. 267-287.

Gibson, L.J.; Ashby, M.F. *Cellular Solids: Structure & Properties*. Pergamon Press, Inc., 1988.

Goble, D.L.; Wolff, E.G. Strain-rate Sensitivity Index of Thermoplastics. *Journal of Materials Science* 1993, 28, pp. 5986-5994.

Hammi, Y.; Horstemeyer, M.F. A Physically Motivated Anisotropic Tensorial Representation of Damage with Separate Functions for Void nucleation, Growth, and Coalescence. *International Journal of Plasticity* 2007, 23(10-11), pp. 1641-1678.

Horstemeyer, M.F.; Lathrop, J. et al. Modeling Stress State Dependent Damage Evolution in a Cast Al-Si-Mg aluminum Alloy. *Theoretical and Applied Fracture Mechanics* 2000, 33(1), pp. 31-47.

Huang, J.S.; Gibson, L.J. Elastic Moduli of A Composite of Hollow Spheres in A Matrix. *Journal of the Mechanics and Physics of Solids* 1993, 41, pp. 55-75.

Ishihara, S.; Nan, Z.; Goshima, T. Effect of the Microstructure on Fatigue Behavior of AZ31 Magnesium Alloy. *Materials Science and Engineering A* 2007, 468, pp. 214-222.

Jang, C.; Nouranian, S.; Lacy, T.E.; Gwaltney, S.R.; Toghiani, H.; Pittman Jr., C.U. Molecular Dynamics Simulations of Oxidized Vapor-Grown Carbon Nanofiber Surface Interactions with Vinyl Ester Resin Monomers. *Carbon* 2011, doi:10.1016/j.carbon.2011.09.013.

Jaslow, C.R., *Mechanical Properties of Cranial Sutures*. *J Biomechanics* 1990, 23, pp. 313-321.

Jordon, J.B.; Gibson, J.; Horstemeyer, M.F.; El Kadiri, H.; Baird, J.; Luo, A.A. Effect of Twinning, Slip, and Inclusions on the Fatigue Anisotropy of Extrusion-Textured AZ61 Magnesium Alloy. *Materials Science and Engineering A* 2011, 528, pp. 6860– 6871.

Kim, S-G.; Horstemeyer, M.F.; Baskes, M.I.; Rais-Rohani, M.; Kim, S.; Jelinek, B.; Houze, J.; Moitra, A.; Liyanage, L. Semi-empirical Potential Methods for Atomistic Simulations of Metals and Their Construction Procedures. *J. Eng. Mater. Technol.* 2009, 131(4), 041210 [9 pages].

Krauss, S.; Monsonego Ornan, E.; Zelzer, E.; Fratzl, P.; Shahar, R. Mechanical Function of a Complex Three Dimensional Suture Joining the Bony Elements in the Shell of the Red Eared Slider Turtle. *Advanced Materials* 2009, 21, pp. 407-412.

Lee, J. Characterization of the Effect of Material/fabrication Parameters on the Mechanical Response of Vapor-grown Carbon Nanofiber/Vinyl Ester Nanocomposites. MS Thesis, Department of Aerospace Engineering, Mississippi State University, 2010.

Marin, E.B. On the Formulation of Crystal Plasticity Model; SAND2006-4170; Sandia National Laboratory: Los Alamos, NM, 2006.

Morita, S.; Tanaka, S.; Ohno, N., Kawakami, Y.; Enjoji, T. Cyclic Deformation and Fatigue Crack Behavior of Extruded AZ31B Magnesium Alloy. *Materials Science Forum* 2010, 638-642, pp. 3056-3061.

Mouritz, A. P. Ballistic Impact and Explosive Blast Resistance of Stitched Composites. *Composites Part B: Engineering* 2001, 32, pp. 431-439.

Najafi, A.; Rais-Rohani, M. Coupled Sequential Process-Performance Simulation and Multi-Attribute Optimization of Thin-Walled Tubes. In *Proceedings of the ASME 2011 International Design Engineering Technical Conferences*; Washington, D.C., Aug 29-31, 2011.

Najafi, A.; Marin, E.B.; Rais-Rohani, M. Influence of Anisotropic Texture on Crushing Behavior of Square Tubes. In *Proceedings of the 52nd AIAA/ASME/ASCE/AHS/ASC Structures, Structural Dynamics and Materials Conference*; Denver, CO, April 4-7, 2011a.

Najafi, A.; Rais-Rohani, M.; Hammi, Y. Multi-Attribute Integrated Forming-Crush Simulation Optimization Using Internal State Variable Model. In *Proceedings of 1st World Congress on Integrated Computational Materials Engineering (ICME)*; Seven Springs, PA, July 10-14, 2011b.

Nouranian, S; Jang, C; Lacy, T.E.; Gwaltney, SR; Toghiani, H; Pittman Jr., CU. Molecular Dynamics Simulations of Vinyl Ester Resin Monomer Interactions with a Pristine Vapor-Grown Carbon Nanofiber and Their Implications for Composite Interphase Formation. *Carbon* 2011, 49(10), pp. 3219-3232.

Ochi, Y.; Masaki, K.; Hirasawa, T.; Wu, X.; Matsumara, T.; Takinaga, Y.; Higashi K. High Cycle Fatigue Property and Micro Crack Propagation Behavior in Extruded AZ31 Magnesium Alloy. *Materials Transactions* 2006, 47(4), pp. 989-994.

Prabhu, R.; Horstemeyer, M.F.; Tucker, M.T.; Marin, E.B.; Bouvard, J. L.; Sherburn, J.A.; Liao, J., et al. Coupled Experiment/Finite Element Analysis on the Mechanical Response of Porcine Brain Under High Strain Rates. *Journal of the Mechanical Behavior of Biomedical Materials* 2011, 4, pp. 1067-1080.

Rhee, H.; Horstemeyer, M.F.; Hwang, Y.; Lim, H.; El Kadiri, H.; Trim, W. A Study on the Structure and Mechanical Behavior of the Terrapene Carolina Carapace: A Pathway to Design Bio-inspired Synthetic Composites. *Materials Science and Engineering: C* 2009, 29, pp. 2333-2339.

Springer, G.S. Effects of Temperature and Moisture on Sheet Molding Compounds. *Journal of Reinforced Plastics and Composites* 1983, 2, pp. 70.

Yang, F.; Yin, S.M.; Li, S.X.; Zhang, Z.F. Crack Initiation Mechanism of Extruded AZ31 Magnesium Alloy in the Very High Cycle Fatigue Regime. *Materials Science and Engineering A* 2008, 491, pp. 131-136.

Zhang, H.; Zhang, Z.; Friedrich, K.; Eger, C. Property Improvements of In Situ Epoxy Nanocomposites with Reduced Interparticle Distance at High Nanosilica Content. *Acta Materialia* 2006, 54, pp. 1833-1842.

G. Multi-Material Enabling

Oak Ridge National Laboratory

Field Technical Monitor: C. D. Warren
Oak Ridge National Laboratory
1 Bethel Valley Road; Oak Ridge, TN 37831
(865) 574-9693; e-mail: warrencd@ornl.gov

Technology Area Development Manager: William Joost
U.S. Department of Energy
1000 Independence Ave., S.W.; Washington, DC 20585
(202) 287-6020; e-mail: william.joost@ee.doe.gov

Contractor: Oak Ridge National Laboratory (ORNL)
Contract No.: DE-AC05-00OR22725

This project consists of four tasks critical for the welding of lightweighting metal structures. The tasks include (1) development of an understanding of dynamic loading on spot welds in AHSS's; (2) development of friction stir spot welding (FSSW) methods for AHSSs; (3) development of friction stir and ultrasonic welding methods for Mg (Mg) alloys; and (4) development of a rapid, reliable spot weld inspection method for use in manufacturing plants.

Executive Summary

Significant weight reduction in future vehicle structures will likely occur through the adoption of a variety of materials including light metals. The obstacles to incorporating these materials include material cost and manufacturability. In addition to these obstacles, critical technologies are needed to enable the cost-effective performance necessary for application of these materials. Those technologies include multi-material joining, corrosion prevention, and nondestructive evaluation (NDE).

Joining in nontraditional material systems requires significant changes in processes and techniques as compared to conventional steel structures. An understanding of the new material response to dynamic loads is needed even if traditional joining methods (such as spot welding) are used. Alternative joining methods for magnesium (Mg), aluminum (Al), and high-strength steels (HSSs) are needed when joints are formed from similar and dissimilar materials. Candidate methods may include friction stir welding (FSW), friction stir spot welding (FSSW), ultrasonic welding (USW), fusion bonding, adhesive bonding, and others.

Corrosion of alternative candidate automotive materials is a potential limiting factor to their adoption. Research is needed to mitigate the corrosion of Mg, Al, and HSSs in an automotive environment. Corrosion issues become more critical for dissimilar material joints, especially when the materials have a significant difference in electrochemical potentials. Mitigation strategies are needed.

The quality of materials and joints is critical to their application. Nondestructive inspection methods for verifying joint integrity and material quality are needed. Those methods need to be rapid, reliable, repeatable, and easily integrated into automotive production plants.

The balance between strength, modulus, fracture toughness, and strain rate sensitivity is different for different materials. As a result, design methods for these materials need to be developed to maximize their positive attributes and minimize their negative attributes. This project develops alternate material and multi-material design methods while integrating joining, corrosion prevention, and component optimization.

This project consists of six tasks critical for the welding, inspection, and development of lightweighting metal structures. The tasks include (1) development of an understanding of dynamic loading on spot welds in advanced HSSs (AHSSs); (2) development of USW methods for Mg alloys; (3) development of a rapid, reliable spot weld inspection method for use in manufacturing plants; (4) design of a lightweight engine; (5) improvement the fatigue life of welds, and (6) design of joints for Al-steel chassis structures.

Activity and Developments

Dynamic Characterization of Spot Welds in Advanced High-Strength Steels

Principal Investigator: Zhili Feng, ORNL
(865) 576-3797; e-mail: fengz@ornl.gov

Principal Investigator: Srdjan Simunovic, ORNL
(865) 241-3863; e-mail: simunovics@ornl.gov

Accomplishments

- Generated a comprehensive data set of the spot weld static strength and failure modes under four different loading conditions covering 17 combinations of steel grades, coatings, thicknesses, and 2T/3T stacks.
- Developed an online spot weld property database and retrieval system for data dissemination with industry collaborators.
- Extended the spot weld element (SWE) formulation to handle the heat affected zone (HAZ) softening of certain AHSS welds.

Future Directions

- Validate a resistance spot weld process and property model that can cover common resistance spot welds of AHSS for auto-body structures (steel grades, coating, material mixing, thickness, and stack).
- Validate an SWE formulation for different AHSS thickness combinations of 2T stack and different 3T thickness configurations.
- Complete an SWE simulation with developed failure criteria and validate.

Technology Assessment

- Target: A spot weld modeling tool capable of incorporating the behavior of spot welds (strength, failure mode, and deformation rate effects) that is practical to use in advanced auto-body structure crashworthiness computer aided engineering (CAE), for more efficient design of structures of AHSS for lightweighting while meeting crash requirement and cost-effectiveness.
- Gap: The prediction of spot weld failure of AHSS in finite element modeling (FEM) crash analysis does not match experimental results in stress magnitude or in the failure modes observed, which greatly affects the overall accuracy of crash analysis of welded structure components.
- Gap: The lack of accurate crash analysis methods for welded structures impedes the rapid adoption and optimal use of AHSS and other lightweight materials in auto-body structures.

Introduction

The primary driver for increased use of AHSSs in auto-body structures is the drastic improvements in performance while reducing vehicle weight. Resistance spot welding (RSW) is by far the most common joining process used in automotive manufacturing. Typically, there are several thousand spot welds in a vehicle. Because the failure of spot welds can affect the crash response of welded structural components, the static and dynamic behavior of the spot welds has been one of the critically important considerations in vehicle design and manufacturing.

CAE based simulation of the crash behavior of auto-body structures is an indispensable tool that enables rapid and cost-effective design and engineering of crashworthy auto-body structures. The prediction of spot weld failure in crashworthiness CAE simulation has been generally unsatisfactory for AHSS and other lightweight materials such as Al and Mg alloys. The lack of fundamental understanding of and predictive capability for spot weld behavior is a critical barrier that hinders rapid adoption and optimal use of lightweight materials in auto-body structures. Weld failures, detected in later stages of the new model car development cycle, have frequently resulted in design compromises that can adversely affect the weight savings available from using AHSS. Further lightweighting opportunities from optimized use of AHSS and other lightweighting materials are not possible without an improved understanding of the phenomena and the development of respective spot weld CAE tools.

Approach

This project is developing a new and robust approach to reliably predict the deformation and failure of spot welds in advanced crashworthiness CAE. These developments will provide solutions to the barriers to the design and engineering of crashworthiness for welding-intensive auto-body structures. The project will cover the range of AHSSs, weld configurations, welding conditions, and loading modes required for industry CAE implementation. The outcome will be an optimized model that can be implemented in crash simulation finite element analysis (FEA) codes used by the automotive crash modelers.

A three-pronged approach, supported by experimental data, was used to develop the new spot weld modeling methodology:

- a SWE formulation and associated constitutive models optimized for robustness in CAE simulation and practical to use by automotive crash modelers, yet with the complexity to incorporate weld geometry and microstructure effects;
- a physics based, integrated, electrical-thermal-mechanical-metallurgical spot weld process model to generate the weld geometry, microstructure, and residual stress results needed by SWE; and
- a companion weld characterization and impact test database for development and validation of the new spot weld modeling approach.

Results and Discussion

In FY 2011, we completed comprehensive testing and characterization of resistance spot welds. The test matrix included four different grades of steel (DP 600, DP 980, TRIP 780, boron), four different surface coatings [hot dipped galvanized (HDG), hot dipped galvanized, hot dipped aluminized, and uncoated], and three different thicknesses (1.0, 1.2, and 2 mm). The test matrix also included welding of different combinations of AHSSs (DP 600/DP 980, DP 600/TRIP 780, TRIP 780/boron), different thicknesses, and 3T stacks. For each combination of steel grade, coating, and thickness, welds were produced with three different weld nugget sizes. The welded samples were tested under lap-shear, cross-tension, coach-peel conditions, and a specially designed in-plane torsion condition. The test matrix covered more than 220 unique combinations of materials, welding, and mechanical testing conditions. In addition, multiple duplicates of welds were produced for each combination for microstructure characterization, microhardness mapping, and miniature mechanical property testing that will be carried out in FY 2012.

To efficiently manage and evaluate the large data set and to enable future technology transfer, we have established a project web page (Figure 1). The current configuration is used for test analysis and for distribution of FEM models and formulations. A more detailed description of the method and results from the high-resolution simulations will be presented in the first quarter of FY 2012.

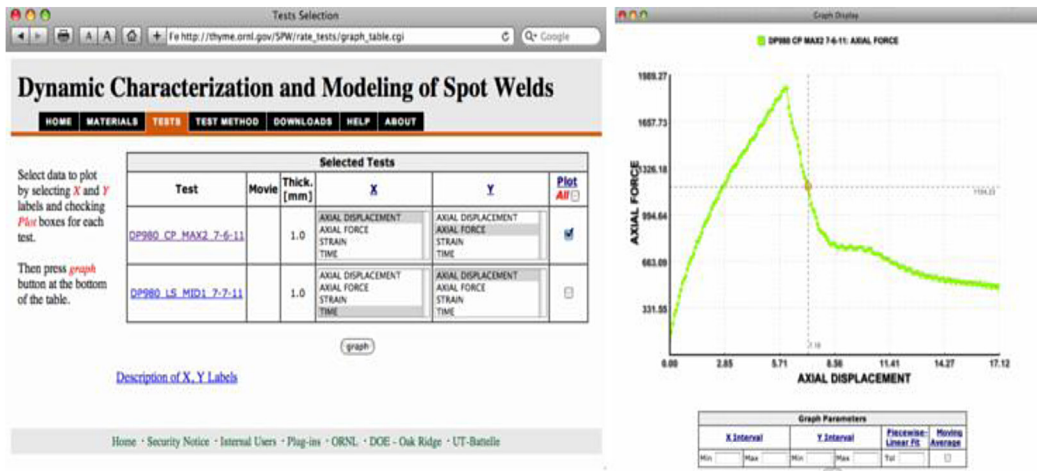


Figure 1. Interface for online experimental data retrieval and analysis.

Table 1 provides examples of selected testing results of TRIP 780 and heat treated boron steels. It is noteworthy that the dissimilar metal joints between TRIP 780 and boron steels have higher strength than both steels welded to themselves under cross-tension loading conditions. In addition, the failure of the dissimilar metal joint was located in the higher-strength boron steel side under both lap-shear and cross-tension loading conditions. The causes of such failure in dissimilar metal joints are being investigated.

Table 1. Joint strength of TRIP 780 and boron steel, and their combination; sheet thickness: 1.0 mm.

Material	Nominal weld size (mm)	Loading mode			
		Lap shear		Cross-tension	
		Strength (N)	Failure mode	Strength (N)	Failure model
TRIP 780 to TRIP 780	4.0	8359	Button	2884	Button
	4.8	8967	Button	3459	Button
	5.5	11670	Button	4863	Button
Boron to boron	4.0	12244	Interfacial	3738	Button
	4.8	14654	Button	3668	Button
	5.5	15744	Button	3963	Button
TRIP 780 to boron	4.0	10577	Button, Boron side	3877	Button, Boron side
	4.8	11309		4201	
	5.5	12562		4126	

The effect of weld nugget size on the joint strength is illustrated in Figure 2. It is evident that the weld nugget has very strong influence on the joint strength. Such load-displacement curves will be used to assist and validate the SWE model.

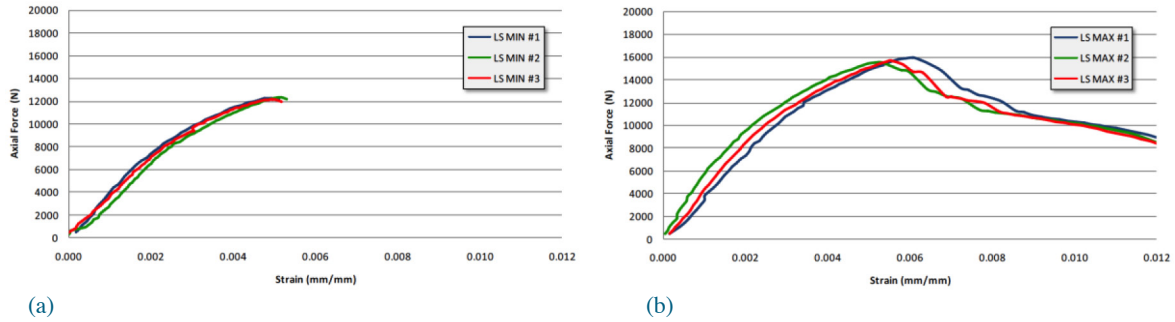


Figure 2. Load-displacement curves of boron steel welds. Three repeats for a given spot weld size; thickness = 1.0 mm. For (a), weld nugget = 4.0 mm; for (b), weld nugget = 5.5mm.

Figure 3 shows the microhardness distribution in a DP 980 spot weld made between a 1.2 mm thick sheet and a 2.0 mm thick sheet. The weld nugget region exhibits much higher hardness due to the formation of nearly 100% martensite. The HAZ softening—a region outside of the weld nugget exhibiting a reduction of hardness, thereby the strength—is clearly revealed. The physics based, integrated, electrical-thermal-mechanical-metallurgical spot weld process model developed in this project is capable of predicting such features of microstructure and property heterogeneity, as reported in the FY 2010 annual report. The integrated model is being further refined and validated with the comprehensive set of welds and testing results generated this fiscal year (2011). In FY 2011, the integrated weld process model gained a new feature to properly handle the chemical mixing in the molten nugget region between steels with different chemistry. The model is being compared with the experimental data.

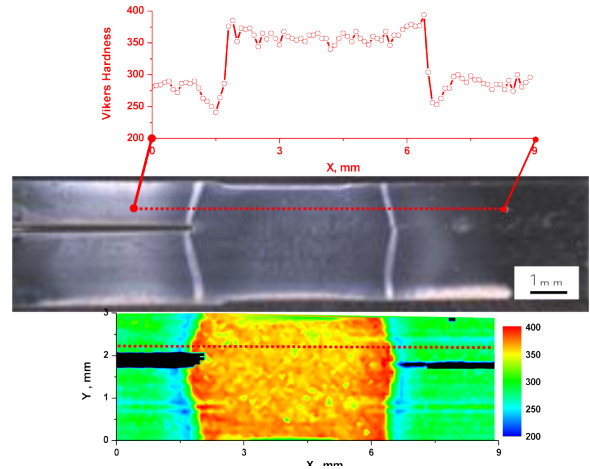


Figure 3. Microhardness mapping of DP 980 steel. Sheet thickness: top = 1.2 mm, bottom = 2.0 mm.

For the SWE development, we have developed parametric, high-resolution mechanical models for analysis of the mechanical response of the joints. The parametric form allows for systematic investigation of model performance and convergence properties. Results from the welding simulations are mapped into mechanical properties of the material in the spot weld specimens. Details of the high-resolution mechanical spot weld models in lap-shear and cross-tension test configurations are shown in Figure 4.

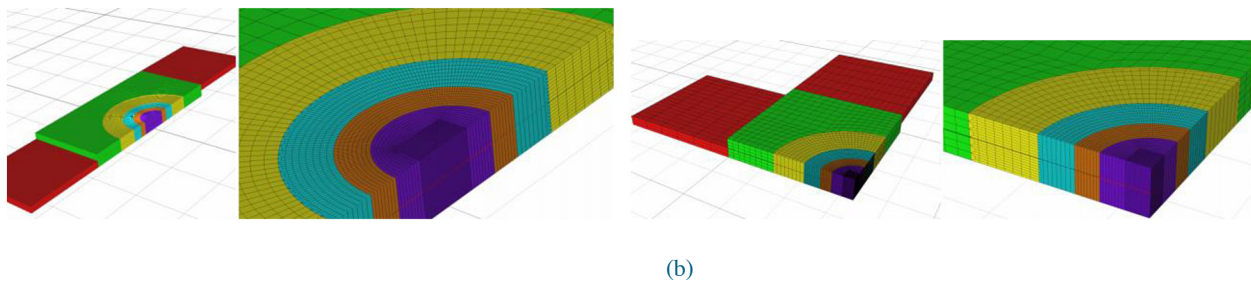


Figure 4. High-resolution finite element model of a lap-shear spot weld specimen (a) and a cross-tension spot weld (b). Colors denote different zones in the specimen.

These high-resolution models are used for determining a strategy for scaling up the formulation into a coarse-mesh formulation as illustrated in Figure 4. The simulations are also used to determine appropriate scaling of material properties in the weld zones that are expected to control the overall response of the joint. In the SWE formulation, plates are modeled by shell finite elements. Weld nuggets are modeled by solid elements. The coupling interfaces will also incorporate progressive failure mechanisms as is shown in Figure 5.

To be able to accurately model the mechanical response and the load transfer in the coarse-scale spot weld, a new formulation for coupling its parts is needed. The new model cannot be entirely built using the available technology and existing capabilities in commercial software. Currently available formulations in commercial codes for connecting shell (representing sheet metal) and solid elements (representing welds) do not couple all the required degrees of freedom to allow for accurate mechanical representation of the joint. We have developed coupling formulations based on expanding the degrees-of-freedom approach that account for specifics of the spot weld mechanical response. The formulations will be extended to modeling dominant failure regions and their behavior based on experiments and results from high-resolution models.

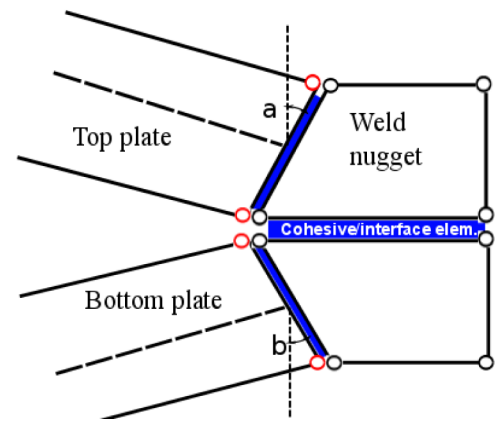


Figure 5. A scheme of the developed coarse-scale spot weld submodel model for component-level crash simulations.

Conclusions

The integrated electrical-thermal-mechanical-metallurgical RSW process and performance model formulation have been successfully developed with all essential features to handle various materials, joint geometries, and welding process conditions typically encountered in RSW of AHSS auto-body components. The integrated weld process model has been shown to be stable and robust and can be used to provide the microstructure and local property variations (including the HAZ softening) as input to the SWE model. This model is being further validated with the comprehensive experimental data set generated in FY 2011. A comprehensive spot weld dataset and an effective online based data retrieval and analysis tool have been completed. The formulation of the robust SWE will be further developed in FY 2012.

Ultrasonic Solid State Joining Magnesium to Steel

Principal Investigator: Michael Santella, ORNL
(865) 574-4805; e-mail: santellaml@ornl.gov

Accomplishments

- Demonstrated the ability to effectively join Mg to steel using both FSW and USW solid-state joining techniques.
- Developed an improved understanding of the effect of different energy sources, whether rotating friction or ultrasonic vibration, and application conditions such as rotation speeds and pressure or ultrasonic frequency and amplitude and their effect on alloy-product form combinations.
- Assessed erosion behavior and developed strategies for controlling it.
- Completed initial milestones demonstrating the ability to produce AZ31 hot dip galvanized mild steel USW with lap-shear strengths exceeding 4 kN.
- Completed initial investigation into bond formation and performance of Mg to steel joints including microanalysis procedures to begin establishing bonding mechanisms.

- Demonstrated that a low cost infrared (IR) camera is capable of both postmortem and real-time weld quality assessment to establish a rapid nondestructive inspection technique for spot welds.
- Applied advanced multiphysics model for revealing temperature and deformation evolution during resistance RSW of AHSSs in two and three layer stackups. The prediction was used to improve the data analysis algorithm used in IR inspection techniques.

Future Directions

- The joining of dissimilar metal will include the determination of the fundamental aspects of Mg-steel bond formation in ultrasonic spot welding. This will include analysis of joint microstructures to better characterize features that contribute to making strong bonds.
- Evaluate weld bonding (combinations of adhesive bonding with the solid-state welding processes) as a means to improve mechanical properties. Research plans include placing more emphasis on fatigue testing in the FSW and USW task with the goal of determining stress levels that can support a fatigue life of 106 loading cycles.

Technology Assessments

- Target: Develop robust, mechanically strong, and industry affordable FSSW and USW processes for joining dissimilar metals.
- Gap: Dissimilar metals are not joinable by conventional welding processes.
- Gap: Joining with adhesives is too expensive and time consuming for dissimilar metal joints.

Introduction

Joining methods available in the cost environment relevant to automotive manufacturing include RSW, adhesive bonding, linear fusion welding, hemming, clinching, bolting, and riveting. However, because of the highly dissimilar natures of Mg and steel, joints of these two metals can be problematic. For instance, Mg-to-steel joints cannot be simply fusion welded due to the extreme differences in their melt temperatures and solid-state methods that require large amounts of plastic strain suffer from the poor ductility of Mg due to its hexagonal crystal structure.

USW appears to have potential for overcoming some of the traditional barriers to constructing hybrid Mg-steel components. USW is commonly considered a solid-state welding process that forms metallurgical bonds with minimal heating. However, no significant studies are available about applying USW to Mg-steel welding.

The purpose of this project is to develop an applied understanding of

- the localized metal forming and metallurgical bonding that develops USW;
- the influence of process parameters on joint strength and performance; and
- the properties of joints, including lap-shear strength, fatigue properties, corrosion issues, and microstructural characteristics.

Approach

This project is designed to overcome some of the technical barriers to implementing the USW process. Task 1 focused on a preliminary assessment of the application of USW for spot welding Mg to steel. It featured a decision gate of achieving lap-shear strengths of at least 1 kN as an indication of technical feasibility. Task 2 concentrated on improving joint strength through modification of process controls and on investigating the fundamental metallurgical aspects of bond formation. Task 3 focused on evaluating fatigue properties of Mg-steel ultrasonic spot welds and developing strategies to control corrosion in

the joints. The tasks were oriented toward developing information useful to manufacturers in their decision making processes. However, the intention was to develop a basic understanding the feasibility of making Mg-steel joints and of the general usefulness of USW.

The ultrasonic welds are made with a Sonobond CLF2500 using a pedestal welding station. The sonotrode tips are made from T1 steel. They typically have flat, rectangular faces with dimensions of either 5 mm by 7 mm or 7 mm by 7 mm.

The materials used for the current experiments were sheets of 0.8 mm thick HDG mild steel and 1.6 mm thick AZ31B-H24. The zinc coating on the steel was about 9 μm thick. Before welding, the surfaces of the AZ31B sheet were buffed with nonmetallic abrasive pads to remove surface oxides and produce shiny surfaces. Both metals were also degreased with acetone followed by isopropyl alcohol to remove lubricants and surface debris.

Coupons of AZ31 nominally 30 mm wide by 100 mm long were welded to mild steel coupons of the same size to produce specimens for mechanical testing and metallographic analysis. A 25 mm overlap was used for making lap-welded coupons with spot welds centered in the overlap regions. Specimens were positioned for welding so that the primary vibration direction of the sonotrode was perpendicular to their long axis. Spot welding was typically performed at 1,500–2,500 W, and welding times typically ranged from 0.2–1.2 s.

Results and Discussion

The results from tensile lap-shear testing are presented in Figure 6, where the variations of failure load with welding time are plotted for two arrangements: Mg-steel, where the sonotrode engaged the AZ31, and Steel-Mg, where it engaged the HDG steel. The Mg-steel results were discussed in a previous report. The maximum lap-shear failure loads for Mg-steel spot welds are near 4 kN in 1.0 s of welding time. Those lap-shear strengths are in the range of the levels found for RSW and FSSW AZ31 to itself. Given the disparities of properties between AZ31 and the mild steel, the lap-shear results are remarkable. The figure indicates that similar maximum failure loads can be achieved with the arrangement of steel contacting the sonotrode. This important result indicates that USW has the desirable flexibility for addressing components in the manufacturing environment.

Initial results from evaluating weld bonding are presented in Figure 7, where the Mg-steel results are replotted for comparison. Results are shown for three adhesive (Dow Betamate 73305) conditions. First, USW spot welds were made through uncured adhesive as is commonly done with RSW. This approach caused a significant decrease of lap-shear strength. Subsequently, some spot welded coupons were cured. Curing produced lap-shear strengths in the range of 6 kN. As a reference, coupons that were only adhesive bonded and cured were also tested, and these had lap-shear strength of 4–5 kN. These results suggest that USW through adhesive is not advisable. Presumably, this is at least partially due to the adhesive modifying friction properties at the welded interface. Additional study will be required to determine how much strength can be preserved in USW spot welds made through uncured adhesives. Once the adhesive is cured, lap-shear strengths can exceed those made by either process alone. In all of the experiments, the area covered by adhesive was about 25 mm by 25 mm, a significantly larger area than that of the USW spot welds (about 7 mm by 7 mm).

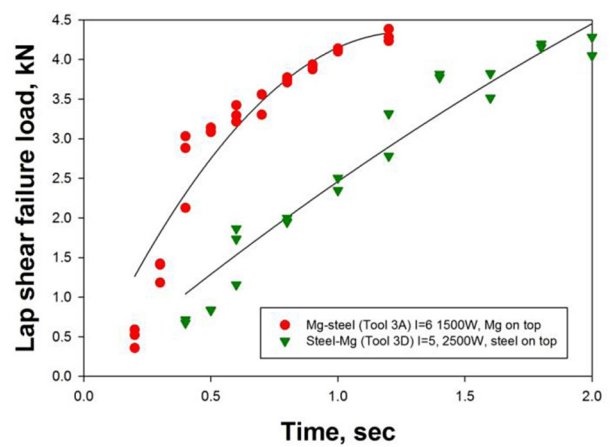


Figure 6. Variations of lap-shear strength with welding time and metal arrangement using a 7 mm by 7 mm sonotrode tip.

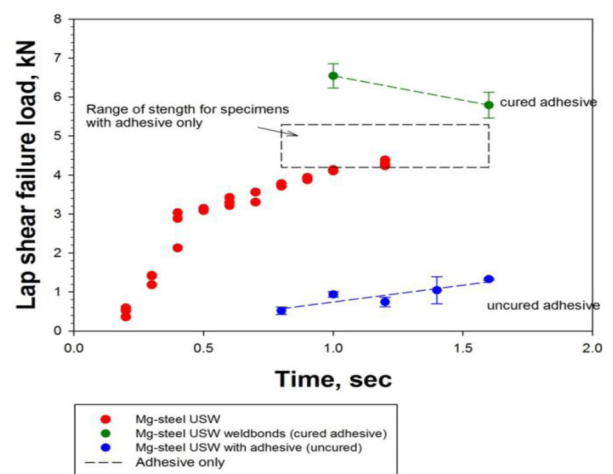


Figure 7. Variations of lap-shear strength with welding time and adhesive cure condition.

Results from an evaluation of the effect of corrosion on lap-shear strength are shown in Figure 8. A total of 20 Mg-steel specimens were made for exposure using the Ford Arizona Proving Ground Equivalent Corrosion Cycle (APGE) test, a widely accepted screening test for automotive components. The exposure consisted of immersion in 5% NaCl bath at room temperature for 15 min followed by air-drying for 3 h. Following this, the dried specimens were placed in a chamber where relative humidity was controlled to 80% and temperature was maintained at 50°C. Each cycle of exposure in the chamber lasted 20.75 h. Starting at the fifth cycle of exposure, one specimen was tested for lap-shear strength after each cycle. Figure 8 shows that strength decreased linearly with each cycle of exposure up to 12 cycles. From that point on, strengths became very erratic and many specimens could be broken by routine handling.

Photographs of a specimen after the 20th cycle are shown in Figure 9. A compound identified as $Mg(OH)_2$ was deposited in the crevice between the AZ31 and the steel. The deposits were observed after even one exposure, but they continued to thicken with each exposure cycle, contributing to a separation force between the sheet specimens. Examination of fracture surfaces found that welded areas also decreased with exposure cycle, but even in the weakest joints there was evidence of metal-metal bonding.

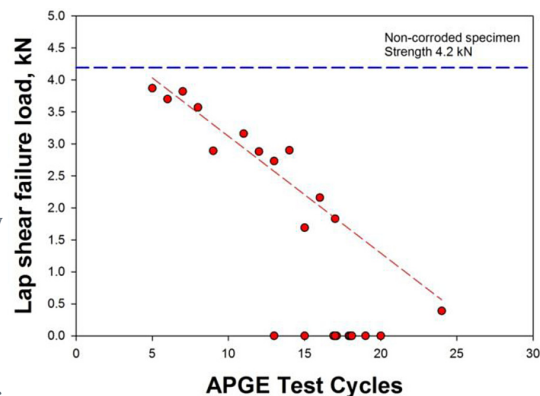


Figure 8. Variations of lap-shear strength with welding time and tip size.

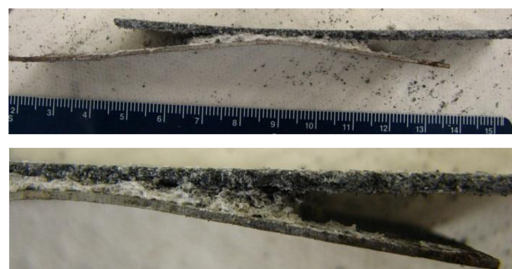


Figure 9. Variations of fatigue life expressed as cycles to failure with loading range.

Conclusions

USW of AZ31 to HDG mild steel was insensitive to metal arrangement. With steel contacting the sonotrode, spot weld failure loads were as high as those with AZ31 contacting the sonotrode, but the weld time needed increased from 1–1.2 s to 1.5–2.0 s. When adhesive bonding was coupled with USW (i.e., weld bonding), lap-shear failure loads increased to near 6 kN. Exposure of spot welds in the APGE corrosion tests showed that lap-shear failure load decreased linearly with exposure cycle. No useable joint strength was preserved after about 17 cycles of exposure.

Online Weld Quality Monitor and Control with Infrared Thermography

Principal Investigator: Zhili Feng, ORNL
(865) 576-3797; e-mail: fengz@ornl.gov

Project Team: Jian Chen, Ralph B. Dinwiddie and Wei Zhang, ORNL

Accomplishments

- Evaluated weld quality attributes including nugget size, existence of surface cracking and/or porosity defects, and weld hardness and microstructure.
- Simulated the postmortem inspection using finite element heat transfer analysis for identifying quantifiable infrared (IR) signal signatures for weld quality and refining heating device and procedure.
- Developed fully automated, efficient, and robust IR image analysis algorithms that can readily meet the online and offline inspection cycle time requirements.
- Completed real-time IR data acquisition on a large matrix of resistance spot welds made of different steels, thickness gauges, coatings and stackups, including leveraging the in-kind industry cost share by AcerlorMittal.

Future Directions

- Continue the measurement of weld quality attributes on spot welds especially those fabricated recently in late August 2011 for use in the development of the correlation between IR thermal signals and weld quality.
- Improve the accuracy of both online and offline IR image analysis algorithms for the weld quality inspection, aided by advanced FEM.
- Begin the assembly of a prototype IR inspection system with major components including cost-effective IR camera, post-weld heating and/or cooling device, software expert system, and computer for data acquisition and analysis.

Technology Assessment

- Target: Develop a system that can meet or exceed the inspection cycle time requirements dictated by the mass production assembly line environment including (1) collection time less than 2–3 s for online inspection, (2) collection time less than 5–10 s for offline inspection, and (3) data analysis and decision making time less than 1–2 s.
- Target: The prototype spot weld quality inspection system based on IR thermography can detect the stuck weld, weld nugget size (up to 0.2 mm resolution), and surface indentation (up to 0.1 mm resolution) in both the two layer (2T) and three layer (3T) stackup configurations.
- Gap: Automated, robust, and efficient IR image acquisition and analysis algorithms and hardware system to determine the weld quality within the targeted time period and with the necessary quality and weld attribute special resolution do not exist.

Introduction

The development of RSW for AHSSs is critical for enabling the broader implementation of AHSSs in vehicle structures for lightweighting and crashworthiness. For example, boron steel, with a strength of 1,500 MPa (i.e., 5 times that of mild steels common to vehicle structures), has been successfully implemented in mass production commercial vehicles (O'Hara, 2010). Lotus estimated a 16% weight reduction for body-in-white (BIW) by using an AHSS intensive automotive body structure (Lotus, 2010). Variations in welding conditions, part "fit-up," and other production conditions inevitably occur in the complex, high-volume BIW assembly process. These variations can result in out-of-tolerance joints that impair the quality and performance of the vehicles. The increasing use of AHSSs and other lightweight metals is expected to pose even more

stringent requirements on joint quality. Reliable quality inspection techniques are crucial for achieving and ensuring high-quality joints on the assembly line. For it to be successfully adopted by the automotive industry, any new quality inspection technology needs to be low cost, fast, and highly accurate.

In last year's (FY 2010's) effort, an RSW quality inspection system was successfully demonstrated based on a low cost IR camera for both real-time (online) and postmortem (offline) applications. As the IR imaging analysis algorithms were just being developed, user intervention was needed for processing the data and judging the weld quality. Built on last year's groundwork, this year's effort was focused on three major areas: (1) development of a fully automated, efficient, and robust IR image analysis algorithms for determining weld quality; (2) acquisition of a weld quality database to cover a wide range of steels, thickness gauges, etc.; and (3) improvement of inspection system hardware including the post-weld heating device and procedure. Details are provided in the following.

Approach

For the IR based inspection technique to be accepted in the intended automotive body structure manufacturing environment, it needs to cover a variety of AHSSs with different grades, thickness gauges, coatings, and stackup configurations in the current and future generations of lightweight vehicle structures. In FY 2011, we conducted extensive welding experiments and data collections for both the real-time and post-weld approaches. The majority of the welding experiments were conducted at AcerlorMittal, and more recently at AET Integration. The AHSSs included galvanized DP 590 1.2 mm and 1.8 mm, DP 600 1.0 mm and 2.0 mm, TRIP 780 1.0 mm and 2.0 mm, cold rolled DP 980 1.2 mm and 2.0 mm, and boron steel 1.0 mm and 2.0 mm. Various combinations of those steels in both 2T and 3T stackup configurations were studied. In the experiment, the welding parameters were carefully controlled to produce welds with varying attributes (the nugget size and the existence of surface cracking, etc.). Several replicates for each condition were produced to understand the statistical variation in weld quality. Real-time IR images during welding were acquired during the experiment. The resulting welds were further analyzed using the postmortem inspection procedure. More than 500 welds were made and thermal images were acquired.

A select number of welds were evaluated destructively for measuring weld nugget size, existence of surface cracking and/or porosity defects, and weld hardness and microstructure. Such weld attribute data are important for the development of the correlation between IR thermal signals and weld quality.

The fully automated image analysis algorithms function by reading and/or collecting the IR image data for online or offline inspection. The algorithms then identify and select the areas of interest and effectively analyze the data to obtain the characteristic signature of the thermal images in correlation to the weld defect and quality. At the time of this report, ORNL was in the process of patent application for IR image analysis and hardware improvement. Therefore, the details of IR image analysis and hardware improvement will be reported in the future. Finally, FEM of surface temperature evolution in both real time and postmortem applications was used to (1) refine the heating device and procedure and (2) identify temperature fingerprints (or thermal signatures) for accurate quantification of weld quality attributes.

Results and Discussion

Figure 10 shows the destructive measurement of weld nugget attributes. The nugget size (\emptyset) and the indentation depth (d) can be readily determined from the weld transverse section shown in Figure 10(a). In addition, the microhardness profiling is done on this transverse section to quantify the weld microstructure. Depending on where the transverse section is cut, the porosity may or may not be captured. To precisely observe the existence of any porosity, the specimen is carefully polished down to the faying surfaces to reveal the normal section, as shown in Figure 10(b).

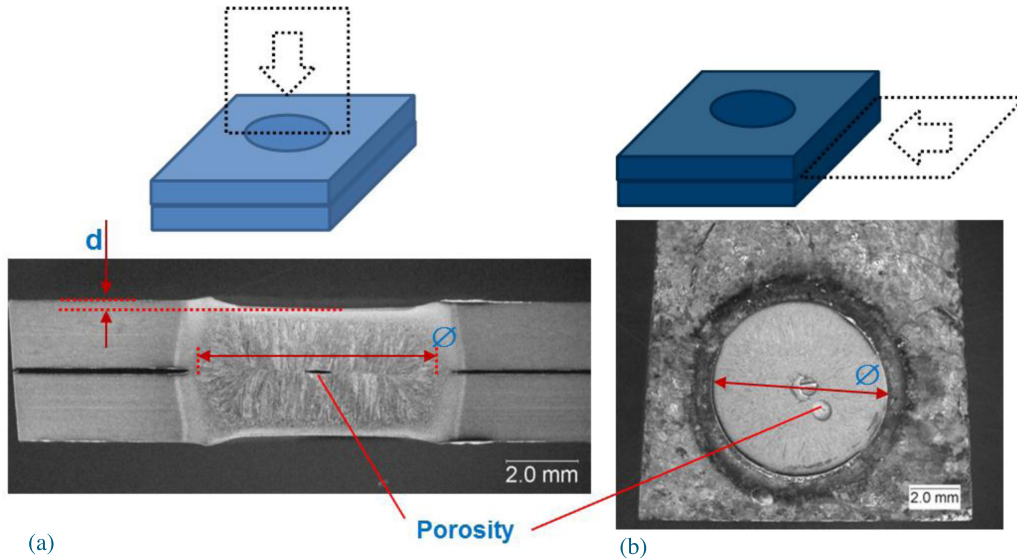
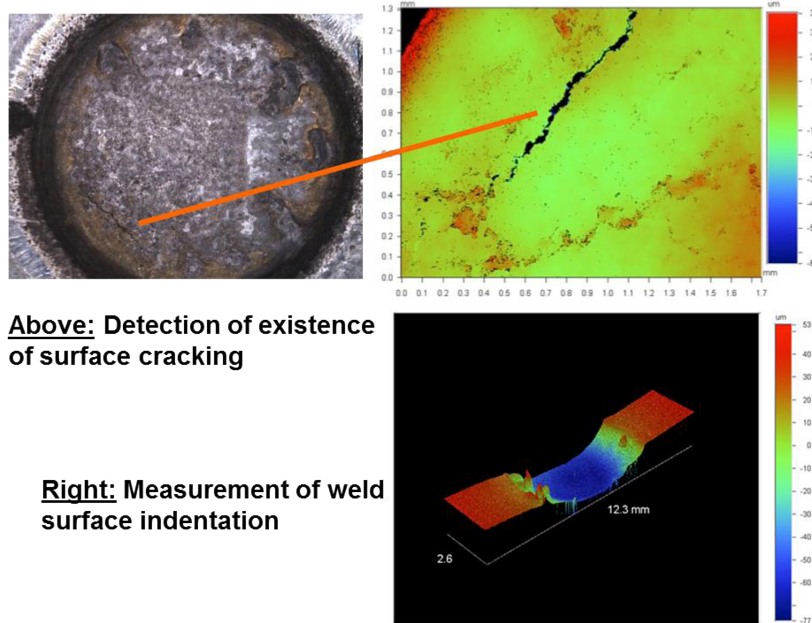


Figure 10. Destructive evaluation for measuring weld nugget size, indentation, and existence of porosity, showing (a) transverse section and (b) normal section. Symbols d and \emptyset correspond to the indentation depth and the weld nugget size, respectively.

Three methods are used for the detection of surface cracking, another common defect found in RSW of AHSSs. The optical imaging method, though very simple, is not reliable for detecting the existence of any cracking due to the surface discoloring. The dye penetrate method, on the other hand, is a reliable way to detect surface cracking. Finally, the three-dimensional (3D) white-light profiling method provides an accurate and quantitative measurement of both the surface cracking and the surface indentation geometry, as shown in Figure 11. The weld attributes determined destructively are prerequisites for correlating IR thermal signatures to the weld quality.



Above: Detection of existence of surface cracking

Right: Measurement of weld surface indentation

Figure 11. Measurement of surface cracking (if any) and indentation using 3D white-light profiling.

Figure 12 shows some preliminary results obtained using the fully automated algorithms for postmortem inspection on two different welds: (a) a weld with acceptable nugget size and (b) a weld with excess heat input leading to expulsion. The calculated thermal signature, shown in the lower right window, exhibits a steeper bottom portion for the acceptable weld than the weld with expulsion. Additional algorithm development is ongoing to quantitatively correlate the thermal signatures to the weld quality. The automated algorithms have so far demonstrated robustness in their ability to tolerate variations in experiment testing, a critical function necessary for the application in automotive assembly line.

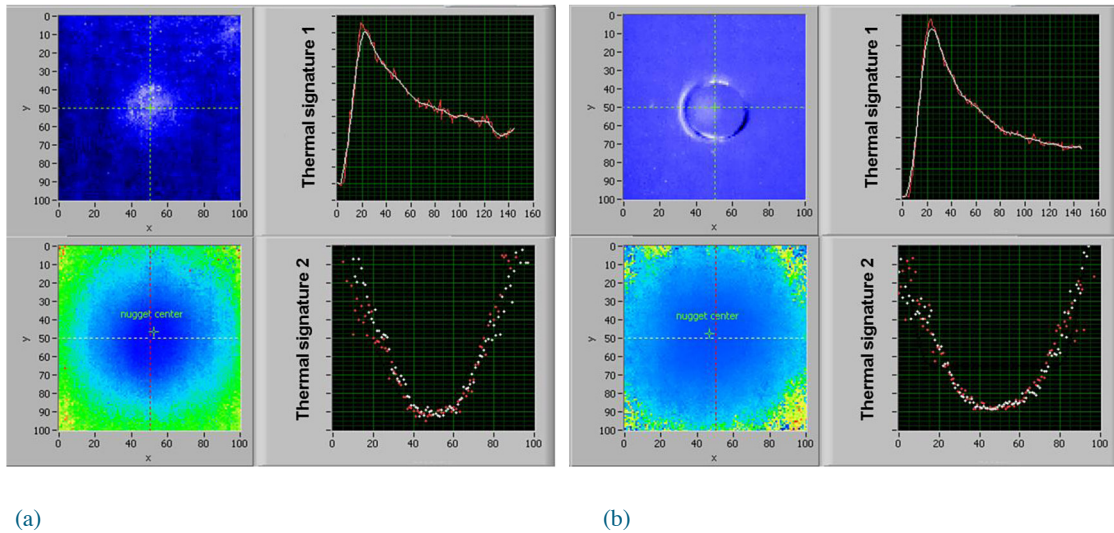


Figure 12. Preliminary results demonstrating the ability of automated data analysis algorithms to distinguish two welds in postmortem inspection: (a) an acceptable weld and (b) a weld with excess heat input, leading to expulsion.

An application of the automated algorithms for real-time inspection is illustrated in Figure 13. As shown in this figure, the algorithms analyze the real-time data during spot welding to extract the thermal signatures, which are then used to correlate to the weld nugget attributes (such as nugget size). Significant development efforts are ongoing to improve the accuracy of both online and offline IR image analysis algorithms for weld quality inspection, aided by advanced FEM.

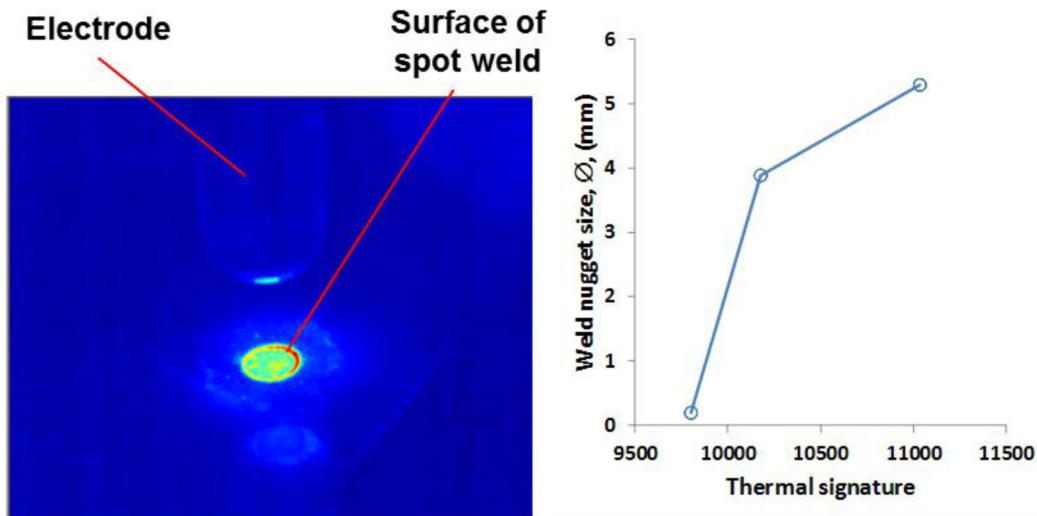


Figure 13. Preliminary results illustrating the quantitative correlation of an IR thermal signature to weld nugget size in real-time inspection.

Conclusions

Significant work was accomplished in FY 2011 toward the development of a cost-effective, robust, and accurate IR thermography based system to quantitatively inspect spot weld quality in automotive manufacturing plants. The weld quality database was expanded based on a large matrix of RSW experiments covering different steels, thickness gauges, coatings, and stackups used in current and anticipated future generations of vehicle structures. Weld quality attributes were evaluated destructively to determine nugget size, existence of surface cracking and/or porosity defects, and weld hardness and microstructure. FEM of both real-time and postmortem applications was performed to identify quantifiable thermal signatures for weld quality and to refine the heating device and procedure. Finally, a first version of the fully automated, efficient, and robust IR thermography image analysis algorithms that can readily meet the online and offline inspection cycle time requirements was successfully developed.

Improving Fatigue Performance of Advanced High-Strength Steel Welds (CRADA)

Principal Investigator: Zhili Feng, ORNL
(865) 576-3797; e-mail: fengz@ornl.gov

Principal Investigator: Benda Yan, ArcelorMittal USA
(219) 399-6922; e-mail: benda.yan@arcelormittal.com

Accomplishments

Completed literature review and state-of-the-art assessment of weld fatigue life improvement strategies pertaining to auto-body structure applications.

- Identified three key factors that can be effectively controlled for weld fatigue life improvement.
- Completed experimental planning and system acquisition for in situ transient weld stress measurement and in situ neutron diffraction study of steel phase transformations.

Future Directions

- Apply the integrated weld process and performance model to identify effective means of controlling the key parameters influencing the weld fatigue life.
- Develop weld filler metal and welding process control methodology for weld fatigue life enhancement.
- Conduct coupon level and component level welding and fatigue life testing to verify the fatigue life improvement strategy.
- Develop case-by-case application guidelines to apply the technologies in automotive body structure fabrication.

Technology Assessment

- Target: Develop robust in-process weld fatigue life improvement technologies that can be used to join AHSS auto-body structural components with cost penalties acceptable to the auto industry.
- Gap: The weld fatigue strength in the as-welded condition does not increase in proportion to the yield/tensile strength of AHSS. The insensitivity of weld fatigue strength to steel strength is a major barrier for lightweighting through down-gaging for chassis and other load-bearing components.
- Gap: Today's weld fatigue improvement techniques are mostly post-weld based. The added steps are cost prohibitive in the high volume mass production automotive environment and there exist large variabilities in the fatigue life achieved by the post-weld-based techniques.

Introduction

Under a CRADA agreement, ORNL and ArcelorMittal USA are working together to develop the technical basis and demonstrate the viability of innovative technologies that can substantially improve the weld fatigue strength and the durability of auto-body structures. The developed technology will be cost-effective and practical in the high volume vehicle production environment. Enhancing weld fatigue performance would close a critical technology gap that impedes the widespread use of AHSSs and other lightweight materials for auto-body structure lightweighting. This means that the automotive industry would be able to take full advantage of AHSS strength, durability, and crashworthiness without being concerned with weld fatigue performance. In the not too distant future, engineers need to be able to design an auto-body structure using the steel and other lightweight, high performance materials with the lightest gages possible to maximize fuel efficiency improvement and greenhouse gas emissions reduction while improving the performance, stiffness, strength, crashworthiness and durability at the lowest cost. Improving fatigue life of welds is critical for achieving this goal.

Durability is one of the primary metrics in designing and engineering automotive body structures. Fatigue performance of welded joints is critical to the durability of body structure because the likeliest locations for fatigue failure are often at welds. Even in the most meticulous fatigue design, a weld may have to be placed in a high tensile stress region, and any possible resulting fatigue crack will likely preferentially initiate at the weld stress riser (Bonnen, 2006). Recent studies by the A/SP Sheet Metal Fatigue Committee, DOE's Lightweighting Materials Program, and others (Bonnen, 2006; Yan, 2005; Iyenger, 2008; Feng, 2008; Feng 2009) have clearly revealed that, unlike the base metal fatigue strength, the weld fatigue strength of AHSS is largely insensitive to the base metal composition, microstructure, and strength under typical welding conditions used in BIW. The lack of inherent weld fatigue strength advantage of AHSSs over conventional steels is a major barrier for vehicle weight reduction through down-gauging, as down-gauging leads to increases in stresses, thereby reducing durability under the same dynamic road loading conditions. In addition to AHSSs, a recent comparative study (Feng, 2011) reveals that other lightweight alloys such as Al and Mg alloys may not offer improved weld fatigue strengths on a "specific weight" basis. Therefore, solutions to improve the fatigue strength of welds are critical to BIW lightweighting.

Because of its broad impact, weld fatigue life has been a topic for extensive research for many years, and many researchers have worked on this topic to find ways to improve weld fatigue life. Many good ideas have been developed, but most involve additional post-processing steps (Prevey, 2003; Matamleh, 2007; Stevens, 2002) such as laser shot peening, low plasticity burnishing, sand blast peening, or coining. Although many of the post-welding stress suppressing techniques are effective in improving the weld fatigue life, they are difficult to implement in the automotive industry due to extra cost and time. Because of the difficulties in improving the weld fatigue life, the auto industry designs the weld line away from the high stress area. If this is not possible, then HSS will not be used. This was the major reason that HSSs, such as dual phase steels, were not used in the chassis structure until recently and are not fully used in other areas due to weld fatigue concerns. One example area is the tailor welded blank/structure/tube, an important lightweighting technology, which often cannot be used due to weld fatigue concerns.

Approach

Instead of using post-welding techniques to improve the weld fatigue strength, this project focuses on developing in-process weld technology as part of the welding operation. The proposed work will take advantage of the extensive experience with AHSSs gained over the years in the nuclear power generation, construction and mining equipment, oil-gas, and automotive industry sectors by both ORNL and ArcelorMittal to develop innovative solutions for weld fatigue life improvement. The proposed joint research will also fully utilize the most advanced test and analysis equipment at ORNL and ArcelorMittal Global R&D, East Chicago, Indiana.

The current work will look into effective ways to control and mitigate the key factors governing the fatigue life of AHSS welds, including weld profile, weld residual stress, and weld microstructure/ chemistry. Two specific in-process approaches will be further developed in this project. Technical and economic issues unique to the automotive body structural welding environment have been identified and will be addressed. Per CRADA policy, specific details of the approaches will be released to the public at a later time.

Results and Discussion

This project started in March 2011. A series of meetings and discussions have been conducted among the team members to review the state-of-the-art weld fatigue life improvement techniques. Through a close interaction between the two teams, pros and cons of different weld fatigue life improvement techniques are reviewed and ranked in consideration of the unique automotive structure and production requirements. Baseline welds are being produced for fatigue testing, weld residual stress measurement, weld profile study, and weld microstructure characterization. ORNL's integrated weld process and performance model is being further developed to predict the weld fatigue life from weld microstructure, weld residual stress, and weld profile. A novel approach using in situ neutron diffraction for steel phase transformation has been identified and will be applied in the course of this project to assist the development of the fatigue life improvement technology. Welding equipment at ArcelorMittal R&D has been upgraded for the planned welding experiments.

Conclusions

Weld fatigue life has been identified as one of the key technology barriers to widespread use of lightweight materials (AHSS, Al and Mg alloys) for auto-body structure lightweighting. The technology developed in this project is expected to provide cost-effective and practical solutions to the automotive industry to address this critical issue.

Infrared Heat Treatment of Cast Bimetallic Joints and Residual Stress Characterization

Principal Investigator: Thomas R. Watkins, ORNL
(865) 574-2046; e-mail: watkinstr@ornl.gov

Principal Investigator: Timothy W. Skrzek, Cosma Engineering
(248) 786-2584; e-mail: tim.skszek@vehmaintl.com

Investigators: Joeseeph A. Angelini, Rick Battiste, Pooron Joshi, Gerald M. Ludtka, Adrian Sabau, Hebi Yin, Wei Zhang, ORNL; Xiaoping Niu, Promatek Research Centre

Accomplishments

- Signed the CRADA with Cosma on April 28, 2011.
- Received flat plate samples and bimetallic joint samples.
- Determined initial microstructures and emissivities of the as-cast plates.
- Have run initial thermodynamic and numerical heat flux simulations.

Future Direction

- Future work will be aimed toward developing Al T5 and modified Al T6 IR heat treat methods for flat Al-Si-Mg castings (i.e., not bimetallic joints), determining the minimum duration of time at temperature with IR heating to achieve yield strength and elongation of conventional T5 and T6 tempers, characterizing IR processed flat samples, beginning the modeling effort, and ultimately proceeding to the "Go/No-Go" decision point (see below).

Technology Assessment

- Target: Achieve the three minimum performance requirements for T5 treated flat castings—yield strength >172 MPa, ultimate tensile strength >243 MPa, and elongation >7%—and/or meet the three minimum performance requirements for T6 treated flat castings—yield strength >250 MPa, ultimate tensile strength >310 MPa, and elongation >8%.
- Gap: Current heat treatments are either too time consuming or degrade the beneficial residual stresses.

Introduction

This project addresses the DOE VTP LM technology barrier of “Joining and Assembly” by facilitating the use of lightweighting, high performance materials that will contribute to the development of vehicles that provide better fuel economy yet are comparable in size, comfort, and safety to today’s vehicles. The project is focused on a specific application on a high volume vehicle platform; however, the joining technologies and methods developed will be applicable to multiple joints throughout this and other vehicle architectures.

The purpose of this project is to investigate an IR heat treatment to increase yield strength and elongation of the cast Al portion of an Al–steel bimetallic joint to achieve a superior joint. IR heat treatments have been demonstrated to provide reduced processing time, reduced energy requirements, and improved material properties of Al components including strength and elongation relative to convection thermal heat treatment methods. The bimetallic joints (Buchholz, 2011) under consideration are part of the automotive front and rear cross-car structure, wherein a steel tube is enveloped by molten Al to form a joint. It is believed that a novel IR heat treatment approach may be able to tailor the temperature profile, post casting, to strengthen the Al, better manage the residual stresses, and achieve a superior joint. Fabrication and thermal processing of a bimetallic structure comprising two dissimilar materials presents processing challenges to mitigate/reduce/optimize many materials issues such as residual stresses, interfacial reactions, and changed properties.

Approach

The technical objective of the CRADA is to develop and model a heat treatment process based on IR heating of an Al casting and a bimetallic joint to produce a T5 temper in a shorter period of time than is currently achievable and, separately, a T6 temper for improved mechanical properties without loss of joint integrity. These objectives have been organized into three research areas: IR processing experiments and prototype assembly, model development and validation, and characterization of castings and joints. Two distinct sets of samples will be examined: flat casting samples and sectioned bimetallic “joint-only” samples. Cosma will supply both flat castings and joint-only samples under standard processing conditions (T5 and T6 anneal) as well as untempered/un-heat-treated flat casting and joint-only samples.

During Phase I of this project T5 and modified T6 IR heat treat methods for flat Al-Si-Mg castings (i.e., not bimetallic joints) will be developed, minimum duration of time at temperature with IR heating to achieve yield strength and elongation of conventional T5 and T6 tempers will be determined, flat samples will be characterized, and the modeling effort will be begun. Ultimately, the project will proceed to the Go/No-Go decision point to meet the three minimum performance requirements for T5 treated flat castings (yield strength >172 MPa, ultimate tensile strength >243 MPa, elongation >7%) and/or the three minimum performance requirements for T6 treated flat castings (yield strength >250 MPa, ultimate tensile strength >310 MPa, elongation >8%) to continue efforts into year 2.

Results and Discussion

Phase I of the project was initiated in late April of FY 2011. More than 200 flat A356 casting samples were received from Cosma. Emissivity measurements have been conducted and the casting microstructure noted. Phase equilibria and heat flux simulations have been conducted.

As part of IR processing experiments and prototype assembly tasks, the emissivity of the as-received sample surfaces was measured. Emissivity, ϵ , is the ability of a surface of a particular material to emit energy by radiation relative to the energy radiated by a black body at the same temperature. This ratio is dimensionless and for a real object $\epsilon < 1$ ($\epsilon = 1$ for a true black body). In production, a colloidal graphite mold release agent is used and the surfaces of the flat casting have residual mold release agent on them. This residual coating would be present in production and impacts the emissivity of the sample surface. For these samples, one surface was darker (more residual graphite coating) than the other. Spectroscopic reflectivity measurements were made using a Perkin-Elmer Lambda 900 spectrophotometer with an integrating sphere attachment, which can be used to measure diffuse reflectance samples. The emissivity of a typical flat casting sample was estimated as $1 - \rho$, where ρ is the reflectivity (Pitts and Sissom, 1977). In Figure 14, the gray hemispherical emissivity was estimated to be 0.88 and 0.84 for the darker and lighter surfaces, respectively.

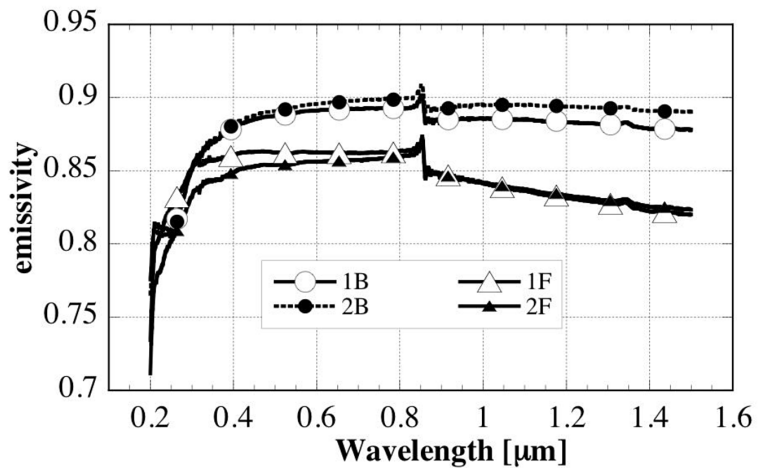


Figure 14. Emissivity of carbon coated flat casting samples obtained from spectroscopic reflectivity measurements. (Note: 1B refers to sample 1, back surface, which is the darker surface; 2B refers to sample 2, back surface; and 1F refers to sample 1, front surface, etc.).

Figure 15 shows the microstructure of the as received as cast samples. A356 is a hypoeutectic Al-silicon (Si) alloy (ASM Handbook, 2004) with alloying contents less than the amount of Si (92.2 Al/7.1 Si/ 0.4 Mg/0.3 other). A network of gray silicon particles surrounds the dendritic Al-Si eutectic phase (American Society for Metals Handbook, 1972). The dendritic structures appear to be about the same size in Figures 15 (a) and 15 (b) but are significantly larger in Figure 15 (c). This difference is likely due to differences in grain nucleation and growth driven by the faster cooling of the outside surface relative to inner/middle regions of the casting.

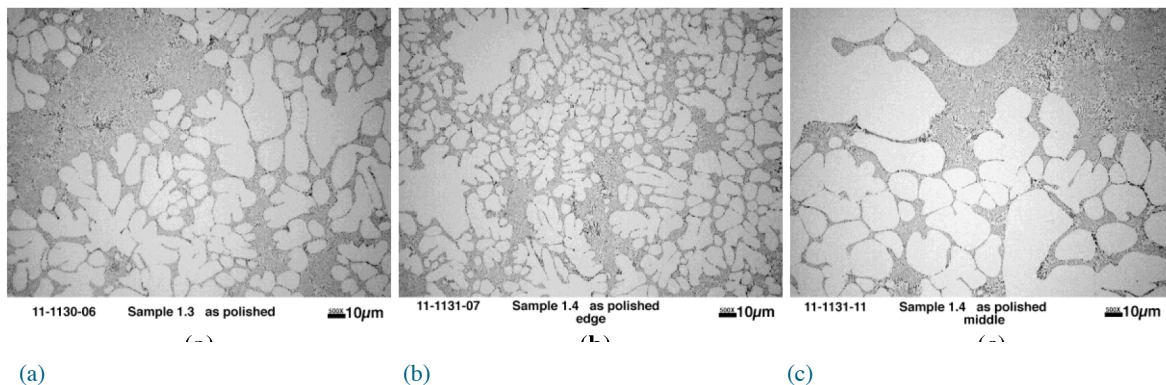


Figure 15. Optical micrographs of an as received as cast sample: (a) in-plane, (b) cross section near the top surface, and (c) cross section near the middle.

Preliminary thermodynamic calculations have been performed to understand the phase equilibrium of Al alloy A356, which is one of the prerequisites for designing heat treatment schedules to achieve the required mechanical properties. Figure 16 is a pseudo-binary Al-Mg phase diagram calculated for the specific composition of the A356 alloy, where the equilibrium phase fractions at three different temperatures are superimposed. At 538°C (1,000°F), a typical solutionizing temperature used for T6, the calculated phases consist of mostly Al (94 mole %) and a small amount of Si (6 mole %). Indeed, the solutionizing treatment at this temperature dissolves the hardening agents (such as Mg_2Si particles) into the Al matrix, reduces the microsegregation of alloying elements, and spheroidizes the eutectic silicon particles to improve the ductility. It should be noted that several hours at the elevated temperature may be needed to reach the desirable extent of homogenization due to the phase transformation kinetics. As the transformation kinetics become much more rapid with increasing temperature, a higher

solutionizing temperature may reduce the time required for homogenization. However, melting may occur if the temperature is too high; at 580°C a significant amount of liquid (54 mole %) exists. A final temperature of interest is 182°C (300°F). This is a typical artificial aging temperature at which the strengthening precipitates form from the supersaturated Al matrix.

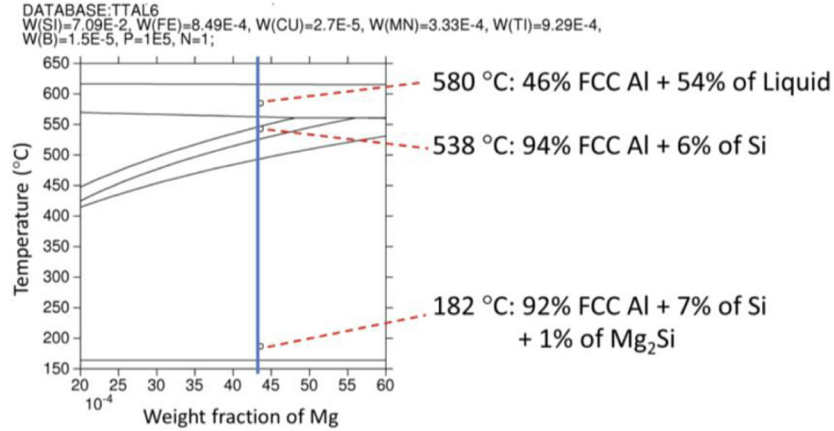


Figure 16. Calculated pseudo-binary Al-Mg phase diagram, where the solid vertical line corresponds to the specific chemical composition of the Al alloy A356. Phase fractions are given as mole percent, and only major phases are labeled.

Numerical simulations were conducted to estimate the heat flux requirements for IR processing. The sample is considered was supported by a few rods, such that conduction losses are minimized. In addition to heat conduction within the sample, the heat transfer losses at sample surface due to natural convection and thermal radiation were considered. The heat transfer coefficients at top and bottom surfaces were taken as 4 and 2 W/cm²K, respectively. The predicted temperature evolution for the top surface is shown in Figure 17 for a sample that was heated with an IR on its lighter side (emissivity = 0.84). The heat flux was varied such that after 60 s of heating under uniform heat flux, the surface temperature would reach 480°C.

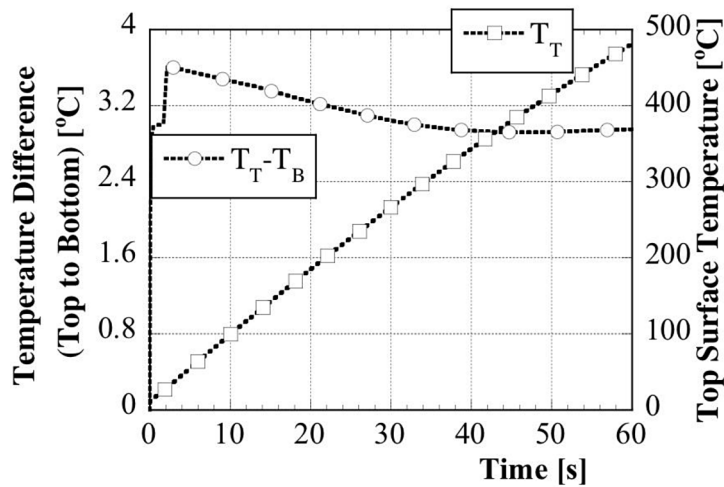


Figure 17. Numerical simulation results for the temperature evolution during the ramp-up period. T_T is the top surface temperature, $T_T - T_B$ is the temperature difference between the top and bottom surfaces of the sample.

Table 2 lists the amount of heat flux required to attain metal surface temperatures of 480°C, 510°C, or 525°C within 15, 30, or 60 s exposure time. Previous heat flux measurements, which were conducted at one offset distance between the sample and IR lamps for the regular ORNL IR flat bed furnace, indicate that the ORNL IR flat bed system can deliver a maximum heat flux of about 20 to 30 W/cm². Table 2 shows that the existing IR flat bed can successfully be used to heat the sample to the target temperature in 60 s.

Table 2. Heat fluxes (W/cm^2) required for reaching the target surface temperatures of 480°C, 510°C, or 525°C within 15, 30, or 60 s when exposed to IR.^a

Target temperature (°C)	Darker surface ramp-up time (s)			Lighter surface ramp-up time (s)		
	15	30	60	15	30	60
480	68.4	35.1	18.3	71.5	36.7	19.1
510	73.0	37.6	19.7	76.4	39.4	20.5
525	75.5	38.9	20.4	79.0	40.7	21.3

^aThe gray hemispherical emissivity was taken as 0.88 and 0.84 for the dark and light surfaces, respectively.

Conclusion

The emissivity and microstructure of samples, which were provided by Cosma, were determined using a Perkin-Elmer Lambda 900 spectrophotometer at wavelengths of 0.2 to 1.4 μm and standard metallography, respectively. Thermodynamic simulations predicted a pseudo-binary Al-Mg phase diagram calculated for the specific composition of the A356 alloy. Numerical simulation results for the temperature evolution during the ramp-up step show that the existing IR flat bed at ORNL can successfully be used to heat the samples to target temperatures in 60 s.

Conclusions

This project comprises seven tasks aimed at developing the computational tools, process methodologies, and inspection methods for joining lightweighting metals. FSW, FSSW, and USW processes for joining steels and dissimilar metals are being developed. Alternative heat treatment method for cast Al and bi-metallic structures is being developed, as well as robust NDE methods for assessing joint quality. The design of a lightweight engine will soon begin.

Presentations / Publications / Patents

Chen, J.; Feng, Z.; Wang, H.; Zhang, W. Non-destructive Inspections of Welds and Joints Using Infrared Imaging and Post-Weld Heating. ORNL patent application, May 2011.

Feng, Z. Multi-Physics Simulation of Fusion Welding. Invited penal presentation at the ASME International Mechanical Engineering Congress and Exposition, Vancouver, British Columbia, Canada, November 12–18, 2010.

Franklin, Teresa J.; Pan, Jwo; Santella, Michael; Pan, Tsung-Yu. Fatigue Behavior of Dissimilar Ultrasonic Spot Welds in Lap Shear Specimens of Magnesium and Steel Sheets. Presented at 2011 SAE World Congress, Detroit, Michigan, April 2011, SAE Paper 2011-01-0475.

Santella, Michael; Franklin, Teresa; Pan, Tsung-Yu; Pan, Jwo. Ultrasonic Spot Welding of AZ31B to Galvanized Mild Steel. Presented at 2011 TMS Annual Meeting & Exhibition, San Diego, California, February 27–March 3, 2011.

References

- American Society for Metals (ASM). Atlas of Microstructures of Industrial Alloys; Metals Handbook, Volume 7; ASM: Metals Park, Ohio, 1972; pp. 257–258.
- ASM International. Metallography and Microstructures; ASM Handbook, Volume 9; ASM International: Materials Park, Ohio, 2004; pp. 715, 720.
- Bonnen, J.; Iyengar, R. M. 2006. Fatigue of Spot Welds in Low-Carbon, High-Strength Low-Alloy, and Advanced High-Strength Steels and Fatigue of Fusion Welds in Advanced High-Strength Steels. In 2006 International Automotive Body Congress, pp.19–30.
- Buchholz, K. Two-Metal Cradle from Cosma is Production-Ready. *Automot. Eng.* [Online] 2011, 15. <http://www.sae.org/mags/AEI/9505> (last accessed September 2011).
- Feng, Z., Chiang, J.; Kuo, M.; C. Jiang, C.; Sang, Y. A New Perspective on Fatigue Performance of Advanced High-Strength Steel GMAW Joints. Presented at Sheet Metal Welding Conference XIII, Detroit, Michigan, May 14-16, 2008.
- Feng, Z. et. al. Weldability and Performance of Welded AHSS Structures. Presented at the DOE EERE Vehicle Technologies Lightweighting Materials Program, Arlington, Virginia, May 9-12, 2011.
- Feng, Z.; Sang, Y.; Jiang, C.; Chiang, J.; Kuo, M. Fatigue Performance of Advanced High-Strength Steels (AHSS) GMAW Joints. Presented at SEA 2009 World Congress, Detroit, Michigan, April 20-23, 2009; Paper 09M-0256.
- Iyengar, R. M. et al. Fatigue of Spot-Welded Sheet Steel Joints: Physics, Mechanics and Process Variability. Presented at the 2008 Great Designs in Steel Seminar (<http://members.steel.org/AM/Template.cfm?Section=GDIS&CONTENTID=24671&TEMPLATE=/CM/HTMLDisplay.cfm>).
- Lotus Engineering, Inc. An Assessment of Mass Reduction Opportunities for a 2017–2020 Model Year Vehicle Program; March 2010.
- Matamleh, O.; Lyons, J.; Forman, R. Laser and Shot Peening Efforts on Fatigue Crack Growth in Friction Stir Welded 7075-T7351 Aluminum Alloys Joints. *Int. J. Fatigue*, 2007, 29, 421–434.
- O’Hara, B.; Shafer, P. 2011 Honda Odyssey Body Development: Concept, Styling, Weight Reduction, and Safety. Presented at the International Automotive Body Congress (IABC), November 2010.
- Pitts, D. R.; Sissom, L. E. Heat Transfer; Schaum’s Outline Series in Engineering; McGraw-Hill: New York, 1977; p. 286.
- Prevey, P.; Mahoney, M. Improved Fatigue Performance of Friction Stir Welds with Low Plasticity Burnishing: Residual Stress Design and Fatigue Performance Assessment. *Mater. Sci. Forum*, 2003, 426–432, pp. 2933–2940.
- Stevens, D. W.; Hackel, L. A.; Lingenfelter, A. C. Laser Peening of Alloy 22 Welds; Technical Report UCRL-ID-149146; U.S. Department of Energy Yucca Mountain Project, Lawrence Livermore National Laboratory: 2002.
- Yan, B.; S.H. Lalam, S. H.; Zhu, H. Performance Evaluation of GMAW Welds for Four Advanced High-Strength Steels; SAE International Paper 2005-01-0904; SAE International: Warrendale, Pennsylvania, 2005.

H. Multi-Material Enabling

Pacific Northwest National Laboratory

Field Technical Monitor: Dean Paxton
Pacific Northwest National Laboratory
902 Battelle Boulevard; P.O. Box 999; Richland, WA 99352
(509)375-2620; e-mail: dean.paxton@pnnl.gov

Technology Area Development Manager: William Joost
U.S. Department of Energy
1000 Independence Ave., S.W.; Washington, DC 20585
(202) 287-6020; e-mail: william.joost@ee.doe.gov

Contractor: Pacific Northwest National Laboratory (PNNL)
Contract No.: DE-AC05-00OR22725 & DE-AC06-76RL01830

Executive Summary

The Multi-Materials Enabling project consists of two tasks focused on research and development that can lead to greater implementation and improved manufacturing of multi-material lightweight components/systems for automotive applications. The tasks include the following: 1) Friction Stir Spot Welding (FSSW) of Advanced High Strength Steels (AHSS) (follow-on); and 2) Friction Stir and Ultrasonic Solid-State Joining of Magnesium (Mg) to Steel.

More energy efficient and environmentally friendly highway transportation is critical to reducing both the environmental impacts and energy consumption associated with transportation mobility. While transformational propulsion technologies and hybrid architectures show great promise in meeting such goals, these and other forthcoming solutions depend upon significant weight savings in passenger and commercial vehicles to fully capitalize on their potential to provide freedom of mobility without harmful emissions and dependence on foreign petroleum. Significant weight savings in the automotive fleet is likely to occur through the use of various advanced materials. While improvements in the properties, manufacturability, and cost of advanced materials are critical in achieving vehicle weight reduction, technologies that support the use of these materials in a multi-material system are equally important. Unlike a single material system, structures composed of different metals and polymer composites present significant challenges in areas such as joining, corrosion, recycling, and nondestructive evaluation. Work conducted in this agreement seeks to overcome these challenges by developing new techniques, establishing standards, and preparing advanced technologies for a production environment. Joining in advanced material systems requires significant changes in process and technique as compared to conventional structures. The use of fusion welding is limited by thermal conductivity or microstructural sensitivity in single advanced-material joints; fusion welding can be nearly impossible for many multi-material joints due to differences in melting temperature or potential for formation of brittle intermetallics.

The following sections outline specific task work conducted at PNNL in the area of multi-material enabling technologies. Each task supports one or more goals within the Multi-Material Enabling Agreement.

Activity and Developments

Friction Stir Spot Welding of Advanced High-Strength Steel Follow-on

Principal Investigator: Yuri Hovanski, PNNL
(509) 375-3940; e-mail: yuri.hovanski@pnl.gov

Principal Investigator: Michael L. Santella, Oak Ridge National Laboratory (ORNL)
(865) 574-4805; e-mail: santellaml@ornl.gov

Accomplishments

- Demonstrated a significantly lower cost manufacturing technique for development of a FSSW tool made from direct-injection molded silicon nitride (FY 2010).
- Made hundreds (approximately 250) of FSSWs on dissimilar combinations of uncoated DP 780, galvanized dual-phase DP780 (DP 780GA), uncoated and coated TRIP590, uncoated TRIP780, and uncoated hot-stamp boron steel (HSBS) using a wide range of welding conditions (FY 2011).
- Completed the durability assessment of polycrystalline cubic boron nitride (PCBN) tooling in uncoated DP980, demonstrating the differences in wear characteristics of Q60, Q70, and 100% PCBN tools (FY2011).

Future Directions

- Evaluate the response of DP 780 with a broader range of zinc coatings (hot-dipped and electrogalvanized, in particular), similar to what will be encountered in the manufacturing environment. Modified Aluminum-Silicon (Al-Si) coatings will also be evaluated for HSBS.
- Understand the durability of PCBN and Silicon-Nitride (SiN) tools being constrained at 1800 lb clamping loads and 10,000 revolutions per minute (RPM) (essential to enable the use of current robotic C-frame technology).

Technology Assessment

- Target: Achieve joint strengths for dissimilar welds in coated and uncoated AHSS that maintain consistent strengths exceeding the American Welding Society (AWS) D8.1 minimum specified strength for resistance spot welds (~10.3 kN for 1.5-mm sheet with an 800 MPa tensile strength).
- Target: Demonstrate weld parameters that have clamping loads below the critical maximum for existing robotic C-frames (~8 kN) while maintaining lap-shear strengths in excess of the AWS minimums.
- Gap: Conventional welding techniques (e.g., spot, laser) damage AHSS microstructures, diminishing properties and weight reduction potential. Variations in coating and thickness requirements for specific applications prevent the use of traditional joining techniques to enable dissimilar combinations of AHSS and ultra-high-strength steels (UHSS).
- Gap: Current weld parameter needed to maintain joint strengths in excess of the AWS D8.1 minimum strengths create clamping forces that greatly exceed the ability of current robotic C-frames. Weld parameters that achieve much lower joint strengths will be required to enable use of automated robots in the FSSW process.

Introduction

AHSS and UHSS have the potential to yield weight savings in vehicle structures by reducing the component gauge and enabling more efficient designs. The properties of these steels provide significant increases in mechanical strength as a result of complex chemistries and microstructure obtained through thermomechanical processing and heat treatments. Joining these steels through conventional fusion techniques—such as resistance spot welding, laser welding, or gas-metal arc welding—can damage the microstructure and severely limit the final efficiency of the joint. The use of solid-state joining techniques such as FSSW avoids the challenges that are inherent with fusion techniques. This project supports developing welding techniques that further enable the use of AHSS and UHSS by enabling joining of dissimilar alloys and coatings while achieving higher joint efficiencies in the weld stack-ups.

An initial project on FSSW of AHSS addressed some basic questions such as whether FSSW of AHSS can be accomplished with currently available tool materials, and whether FSSW made in high-strength steels could develop acceptable tensile lap-shear strength. Efforts were also made to improve joint strength through systematic investigations into weld process parameters and tool design. This was accomplished primarily by using redesigned tools and refined operating parameters, the selection of which was guided by analysis of process output data, microstructure analysis, and strength testing.

This follow-on project is designed to address several of the conclusions of the initial project, including characterization of tool life and durability, and to address the overall cost and availability of tooling and equipment capable of producing FSSW in AHSS alloys. Work also continues in developing the appropriate process parameters for AHSS that are problematic to resistance spot weld, including coated transformation induced plasticity (TRIP) steels and dissimilar thickness and alloy combinations.

Approach

The project is a 50/50 collaboration between ORNL and PNNL. Additionally, it includes a panel of consultants including representatives from Chrysler, Ford, and General Motors. Consultants from companies such as MegaStir (PCBN friction stir tool manufacturer), Ceradyne (Si_3N_4 manufacturer), and Kawasaki (robot manufacturer) also participated on an as-needed basis. University collaborations with Brigham Young University and Michigan State University have also been leveraged to provide in-depth analysis of fatigue performance and tool durability.

The primary focus of this project is the development of FSSW parameters, tooling, and equipment for AHSS alloys that cannot be acceptably resistance spot welded. Using previous work as a guide, parametric studies will be done to attempt optimization of FSSW in alloys that cannot be acceptably resistance spot weld (RSW) based on a balance of joint strength properties and weld cycle time. The influence of stir tool design will be included in the effort. Joint properties will be evaluated initially by tension testing lap joints to determine their shear-tension strengths. Depending on those results, more extensive testing will be done to measure fatigue strength, T-peel strength, cross-tension strength, and possibly impact behavior. The usual metallographic techniques and microhardness mapping will be used to further assess joint characteristics and properties.

Additionally, the effects of zinc coatings applied to carbon steel sheets for corrosion protection will be evaluated. Liquid zinc can embrittle steel through a process known as liquid metal embrittlement, and zinc can similarly attack stir tool materials. The effects of both liquid and solid zinc being stirred into spot welds, in addition to their influence of microstructure, strength properties, and fracture behavior, are not well characterized. Initial studies will use existing inventories of TRIP590, TRIP780, and hot-stamp boron steel (HSBS, sourced from a Swedish supplier, the parent company of US Hardtech). Additional alloys of interest to the OEMs will be included as they are acquired.

The initial project demonstrated that PCBN stir tools are effective for FSSW, AHSS, and UHSS. However, initial cost estimates were high relative to their apparent durability. In addition, the limited number of suppliers of PCBN stir tools was concerning to the automotive community. Material formulations of PCBN used for stir tools are evolving with manufacturers, such as MegaStir, who claim improved performance. In addition, other ceramic-based materials—such as silicon nitride—appear to have some potential as lower-cost tool stock. Identifying the intrinsic limitations of candidate tool materials is an essential aspect of developing more effective, durable, economical tooling. As such, tool durability will be performed as part of this study.

Technology Transfer Path

As the focus of this project is related to enabling multi-material vehicles, a specific focus on technology transfer is designed into the scope. Emphasis on sharing data related to tooling, process parameters, and their effect on mechanical properties is crucial to providing industrial collaborators with the information they need to be able to overcome near-term and future collaborative challenges.

A process database with effective loads, temperatures, and operating parameters is being shared with tool providers to allow them to more efficiently design and manufacture appropriate tooling for FSSW of AHSS. Additionally, the same data are being supplied to machine manufacturers and automotive OEMs to help distinguish the needs associated with implementation of this process leading to appropriate deployment.

Results and Discussion

Continued work related to weld development, evaluation of tool materials, and assessment of deployment issues was performed during FY 2011. An overview of weld performance for AHSS combinations with near-term application is shown in Table 1. Without exception, the joint strength was higher when the top material in the two sheet stack-up was the softer of the two materials. Only in the case where HSBS was used on top (HSBS to TRIP780) did the average lap-shear strength fail to exceed the AWS minimum lap-shear strength of the stronger material in the stack. However, even in this case the average lap-shear strength exceeded the minimum required strength of the weaker material (i.e., TRIP780).

Table 1. Lap-shear results for various combinations of advanced high-strength steels welded using an SN97 tool

AHSS Alloys (Material listed first is on top of stack)	RPM	No. of Steps	Avg. Lap- shear Strength (kN)	AWS D8.1 Minimum for Top Material (kN)	AWS D8.1 Minimum for Bottom Material (kN)
TRIP 590 to DP780	800	2	11.1	7.98	10.32
DP780 to TRIP590	800	2	10.9	10.32	7.98
DP980 to TRIP780	800	1	12.6	11.09	10.32
HSBS to TRIP780	800	1	11.6	12.22	10.32
TRIP780 to HSBS	800	2	12.5	10.32	12.22
DP780GA to TRIP590	800	2	11.2	10.32	7.98
DP780GA to HSBS	800	2	14.0	10.32	12.22
DP780 to HSBS	800	2	13.1	10.32	12.22

Durability testing of PCBN tool variations was completed during this period, demonstrating that the Q70 material (30% W-Re with the difference of PCBN) was the most effective for the process parameter set tested—namely, 1600 RPM with a two-step plunge in fewer than 4 seconds. Degradation in lap-shear strength over 1200 welds is shown in Figure 1. Joint strength exceeded the AWS minimum for 1.4-mm DP980 used in these tests for more than 1000 welds, with the exception of the case as 200 in which the base anvil failed during the welding process.

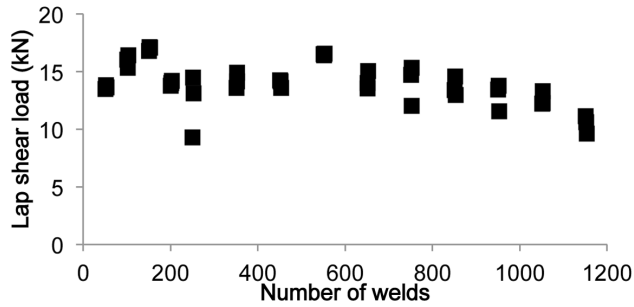


Figure 1. Plot of the variation in lap-shear strength of FSSWs in DP980 (left) made using a Q70 tool with a tapered 3-flat design shown in profile (right)

Results from the weld development and durability studies provided detail needed to evaluate the potential for commercial technology deployment. Of concern to the automotive and welding communities was the magnitude of the process loads required to produce FSSWs with lap-shear strengths exceeding the AWS minimums. A plot of the clamping loads required to produce welds over a 1000 weld run is shown in Figure 2. With a limitation on commercial welding robotic C-frames of approximately 9 kN (1800 lb), a significant decrease in clamping load is needed to enable the use of robotic C-frames. Development of process parameters and tool designs that minimize process loads and clamping forces is currently underway, assessing the potential for using much higher rotational velocities as a means of lowering the clamping loads while maintain the joint strengths.

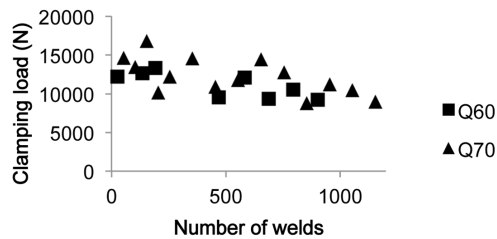


Figure 2. Plot of the variation in Z-loads throughout the life of PCBN variations Q60 and Q70 (left) and a visual of the FSSW process under load (right)

Conclusion

FSSW was demonstrated to effectively produce spot joints in a variety of advanced high-strength and ultra high-strength steel combinations including TRIP, HSBS, and dual-phase steels. Both coated and uncoated variations of these steels were used to access the influence of various zinc coatings on the joint properties. The results from a tool durability study, in conjunction with an analysis of the data obtained while producing dissimilar material welds, provided evidence that process loads would need to be further reduced before the process can be adapted for robotic C-frames. Final development to adapt the parameters for such restrictions is underway as a conclusion to the project.

Friction Stir and Ultrasonic Solid-State Joining of Magnesium to Steel

Principal Investigator: Yuri Hovanski, PNNL
(509) 375-3940; e-mail: Yuri.Hovanski@pnl.gov

Principal Investigator: Michael L. Santella, ORNL
(865) 574-4805 e-mail: santellaml@ornl.gov

Accomplishments

- Demonstrated structural friction stir welded (FSW) joints between automotive mg alloys and automotive sheet steels with lap-shear strengths exceeding 75% of the load-bearing capacity of the weaker material (FY 2011).
- Developed scribed tooling that enables high-strength FSW of dissimilar lap joints (patent application submitted FY 2010).
- Characterized the bond interface of dissimilar friction stir welds of both cast and wrought magnesium alloys joined to automotive sheet steels (FY 2009-FY 2011).

Future Directions

- Complete evaluation of hybrid lap joints that have been friction stir welded and adhesive bonded to determine the effective of the hybrid joining process on both static and dynamic mechanical properties.
- Complete evaluation of surface coatings and interlayers on the corrosion performance of joints between magnesium and steel.

Technology Assessment

- Target: Achieve joint strengths for dissimilar welds between Mg and steel that exceed a structural threshold of 75% joint strength.
- Gap: Conventional welding techniques are incompatible for materials with drastically different melting temperatures. Solid-state welding process like FSW and ultra sonic welding (USW) have the potential to be able to bond materials that are otherwise not possible with traditional fusion approaches.

Introduction

Enabling more widespread usage of lightweight alloys as a means of reducing vehicle weight necessitates the need to better understand how to join these alloys to the suite of other commonly used automotive materials. As steel is currently the automaker's material of choice, the ability to structurally bond magnesium components into a steel body in white becomes a crucial part of enabling greater implementation of lightweight structural materials. In a modern multi-material vehicle, lightweight materials such as Al and Mg alloys can be a challenge to join and attach to the underlying substructure, usually made of steel. Even in Al- and Mg-intensive designs, where entire substructures may be constructed of lightweight metals, there remains a need to join the substructure with other parts of the BIW, such as the predominantly steel passenger safety cage. Joining methodologies available in the cost environment relevant to automotive manufacturing include RSW, adhesives, linear fusion welding, hemming, clinching, bolting, and riveting.

As alternative joining methodologies, FSW, FSSW, and USW may be able to overcome traditional barriers to join and construct hybrid magnesium/steel components. These solid-state joining methods provide unique joining capabilities that—if realized—have the potential to produce faster and more economical alternatives to current technologies (e.g., bolting/riveting). However, FSW and USW for dissimilar Mg/steel combination are significantly underdeveloped for broad deployment.

The purpose of this project is to develop an applied understanding of the following:

- localized metal forming and metallurgical bonding that develops during FSW, FSSW, and USW
- influence of process parameters on joint strength and performance
- properties of joints made with both types of processes including lap-shear strength, fatigue properties, corrosion issues, and microstructural characteristics.

Approach

This project is designed to overcome many of the technical barriers to implementing solid-state joining technologies. The primary efforts of PNNL researchers focused on the development of solid-state friction stir technologies to join Mg alloys to automotive sheet steels. Task 1 focused on systematically evaluating the application of FSW to make lap joints of Mg to steel. It featured a decision gate of achieving lap-shear strengths of at least 40% joint strength as an indication of technical feasibility of the approach. Task 2 concentrated on improving joint strength through modification of process controls and investigating the fundamental metallurgical aspects of bond formation. An initial evaluation by metallographic examination and lap-shear testing using USW for cast Mg alloys was also performed. Task 3 evaluated fatigue properties of Mg-steel FSWs and considered strategies to control corrosion in the joints. The tasks were oriented toward developing information useful to manufacturers in their decision-making processes. However, the intention was to develop a basic understanding of the feasibility to produce Mg-steel joints and of the general usefulness of each of the solid-state welding methods previously outlined.

Technology Transfer Path

As the overall intent of the project in solid-state joining of Mg to steel is intended to be a technology development effort, the overall scope of technology transfer is limited. Nevertheless, the work being developed will be made available to the public via publications, presentations, and international conferences. Additionally, a database containing all appropriate process windows, tooling, and their associated mechanical properties will be provided to participants of the industrial advisory committee.

Results and Discussion

Efforts during FY 2010 concentrated on the development of specialized tooling that enabled increased joint strengths for lap joints between dissimilar materials. These efforts provided the means for determining a suite of process parameters and tooling that consistently produced joints with lap-shear strengths in excess of 75% of the bearing capacity of the weaker material in the two-sheet stack-up. As each of the materials in the dissimilar lap joint had markedly different tensile strengths, stiffnesses, melting points, and other properties, the characterization of failure loads was normalized for the specimen width as shown in the right column of [Table 2](#). In this way, comparisons between specimens of similar materials could be more readily interpreted, allowing for greater clarification of the actual reported lap shear failure loads, also presented in [Table 2](#), center column.

Table 2. Lap-shear failure loads for friction stir welds between Mg alloy AZ31B and automotive sheet steel including both high-strength low alloy and drawing steel type B (MS)

Weld ID	Failure load, N	Failure load/ specimen width, N/mm
AZ31/1.5 mm HSLA I	7482	323
AZ31/ 1.5 mm HSLA II	7883	326
AZ31/ 0.8 mm MS I	4884	220
AZ31/ 0.8 mm MS II	5155	222
HSLA = High-strength low alloy.		

As the tensile strength of the AZ31B Mg sheet used in this study was nearly as high as that of the drawing steel (MS), but less than half of the that of the HSLA steel, the overall joint efficiencies were greatly affected by the overall sheet thickness ratios. **Figure 3** shows that in all cases the Mg sheets were located on the top of the two sheet stack and had a thickness greater than that of the steel substrate. Two specific thickness ratios were examined in great detail; namely 2.3:0.8 (AZ31B to mild steel) and 2.3:1.5 (AZ31B to HSLA). Data presented in Table 2 show that failure loads between the AZ31 and the mild steel were approximately 5 kN, which corresponded to a joint efficiency of more than 80% of the total bearing capacity of the 0.8-mm thick mild steel and less than 50% of the bearing capacity of the 2.3-mm Mg sheet. In comparison, the failure load of the AZ31 to HSLA specimens demonstrated a failure load of approximately 7.5 kN, a significant increase in magnitude over that of the joints made with mild steel. Nevertheless, the actual joint efficiency of the HSLA weld has a much lower overall efficiency because in this case the 2.3-mm Mg sheet has the lower bearing capacity at approximately two-thirds of that of the 1.5-mm HSLA sheet steel.

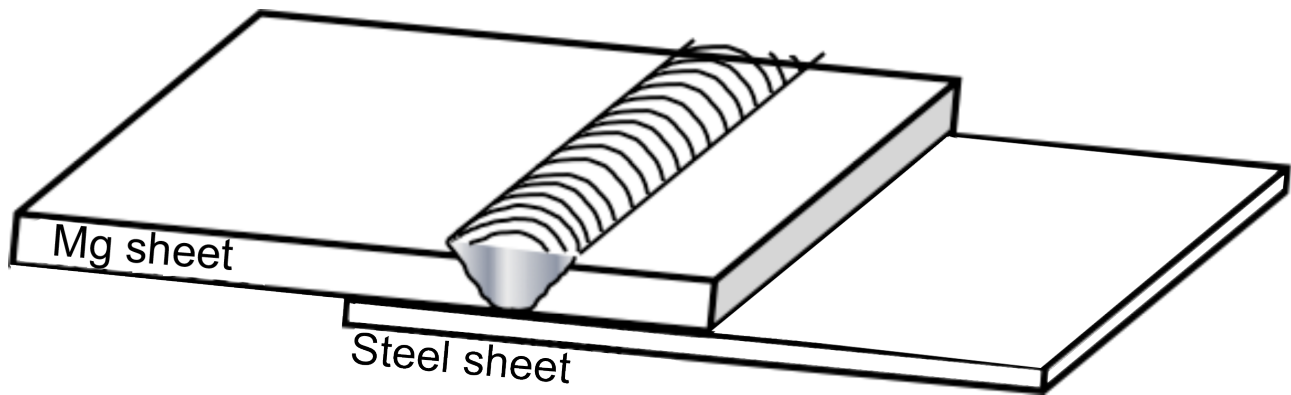


Figure 3. Schematic representation of a lap joint between Mg sheet and steel sheet

Analysis of the performance of various joints led to a better understanding of the influence of the FSW on Mg sheet. The overall bearing capacity of any Mg is reduced in the welding process due to several weld-related phenomena. Furthermore, this reduction in the overall bearing capacity of the Mg creates a limiting threshold for the maximum joint efficiency of welds in which the reduced bearing capacity of the Mg sheet is the weaker material in the dissimilar stack. Literature reported tensile strengths for FSW AZ31 sheet range between 60-80% of the parent sheet, so that even with Mg to Mg welds, 80% efficiency is considered best in class. Thus, joint efficiencies for material combinations in which the weaker material is not the Mg sheet, such as the case with 2.3-mm AZ31 to 0.8-mm mild steel, may exceed an 80% rating. However, when the Mg sheet has the lower tensile strength of the combination, such as the 2.3-mm AZ31 to the 1.5 mm HSLA steel, efficiency above 80% is unlikely.

In addition to developing joints with higher efficiencies, the project team characterized the dynamic performance of FSW dissimilar lap joints between Mg and steel. **Figure 4** presents fatigue results from specimens that demonstrated maximum static strengths in lap-shear tensile tests. The graph on the left, a typical representation of load/cycles to failure, highlights the differences in the actual loads leading to failure in less than 1 million cycles. While there are apparent differences in the trend lines that distinguish the joints between AZ31/HSLA and AZ31/MS, the normalized chart on the right side demonstrates that when normalized by their corresponding static failure loads, the overall fatigue performance of each series is very similar. **Figure 5** presents the fracture surface of a typical specimen showing that fatigue failure, initiating on the upper left and right of the image (edges of the joint interface) propagates across the interface from both edges.

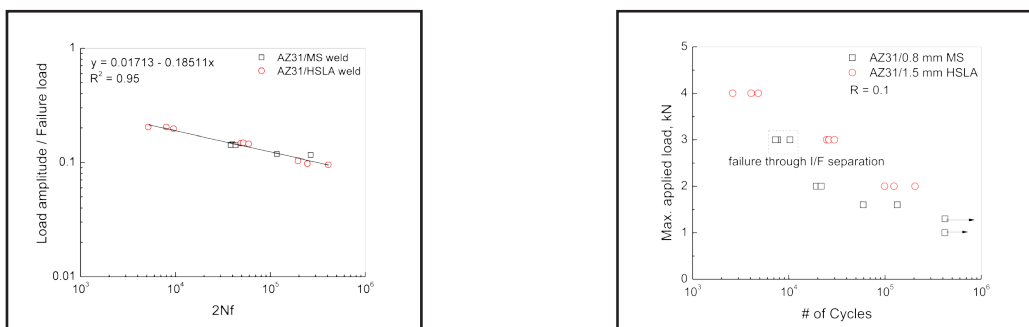


Figure 4. Fatigue results for FSW Mg/steel lap joints (typical S/N curve presented on the left with a normalized graph presented on the right)

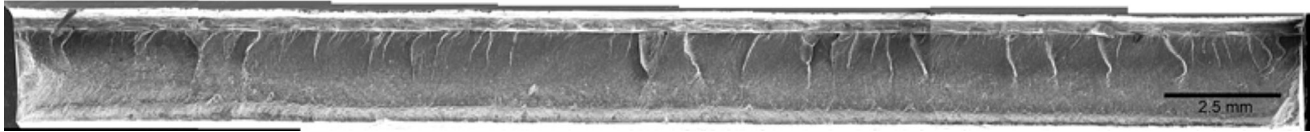


Figure 5. Fractograph of sheet interface between AZ31B Mg sheet and zinc-coated drawing steel type-B

Conclusion

Structural performance milestones were achieved demonstrating the conditions required to achieve greater than 75% efficiency in static performance of FSW Mg /steel lap joints. The material and parameter relationships that enabled higher joint efficiencies were successfully developed. Dynamic performance of the dissimilar joints was characterized, demonstrating the appropriate load regimes for dynamic loading conditions. The project team successfully completed all milestones, effectively developing and demonstrating the capability to joint very dissimilar metals effectively in structural joints.

Conclusions

A multi-material vehicle platform requires an integrated design that uses a wide range of structural materials distributed throughout the entire vehicle with strategic objectives to achieve increased performance and flexibility while providing greater efficiency and reduced weight. Combining and integrating these various materials into a single platform demands novel technology to enable joining of materials that historically were not possible. Both projects outlined herein have been designed to develop and expose various solid-state technologies to the latest available materials that are being used to design and build more efficient vehicles of tomorrow.

Publications/Presentations/Patents

Hovanski Y.; Grant, G.J.; Jana, S.; Mattlin, K. Friction Stir Welding Pin Tool with Scribe. Filed Patent 2010.

Hovanski Y.; Grant, G.; Jana, S.; Santella, M.L. Solid State Joining of Magnesium to Steel. Presented at TMS 2010 Annual Meeting & Exhibition, February 14–18, 2010, Seattle, Washington.

Hovanski, Y.; Jana, S.; Grant, G.J.; Santella, M.L. Friction Stir Welding of Magnesium to Steel. Presented at Materials Science & Technology 2010 Conference, October 17–21, 2010, Houston, Texas.

Hovanski, Y.; Santella, M.L.; Grant, G.J. Friction Stir Spot Welding of Advanced High Strength Steels. Presented at Materials Science & Technology 2009 Conference, October 25–29, 2009, Pittsburgh, Pennsylvania.

Hovanski, Y.; Santella, M.L.; Grant, G.J. Friction Stir Spot Welding of Advanced High Strength Steels. Presented at International Automotive Body Congress Conference, Troy, Michigan, Nov. 2009; published in IABC 2009 Conference Proceedings.

Jana, S.; Hovanski, Y.; Grant, G. Friction Stir Welding of Magnesium to Steel: A Preliminary Investigation. *Met. Trans. A*, 2010, 41A, pp 3173-3182.

Jana, S.; Hovanski, Y.; Grant, G.J.; Mattlin, K.F. Effect of Tool Feature on the Joint Strength Of Dissimilar Friction Stir Lap Welds. In *Friction Stir Welding and Processing VI*; Mishra R.S.; Mahoney, M.W.; Sato, Y.; Hovanski, Y.; Verma, R., Eds.; Wiley: New Jersey, 2011, pp 205-211.

Miles, M.; Ridges, C.; Hovanski, Y.; Peterson, J.; Santella, M.L.; Steel, R. Impact of Tool Wear on Joint Strength in Friction Stir Spot Welding of DP980 Steel. *Science and Technology of Welding and Joining*, [Online] 2011, 16; DOI: 10.1179/1362171811Y.0000000047.

Mishra, R.S.; Mahoney, M.W.; Sato, Y.; Hovanski, Y.; Verma, R. Friction Stir Welding and Processing VI, Wiley: New Jersey, 2011.

Ridges, C.; Miles, M.; Hovanski, Y.; Steel, R.; Peterson, J. Wear Testing of Friction Stir Spot Welding Tools for Joining of DP980 Steel. In Friction Stir Welding and Processing VI; Mishra R.S.; Mahoney, M.W.; Sato Y.; Hovanski Y.; and Verma R., Eds.; Wiley: New Jersey, 2011, pp 97-103.

Santella, M. L.; Hovanski, Y.; Frederick, A.; Grant, G.J; Dahl, M.E. Friction Stir Spot Welding of DP780 Carbon Steel. Science & Tech. of Welding & Joining, 2010, 15, pp 271-278.

Santella, M.L.; Franklin, T; Pan, J.; Pan, T; Brown, E. Ultrasonic Spot Welding of AZ31B to Galvanized Mild Steel. SAE Paper 2010-01-0975. Presented at SAE 2010 World Congress & Exhibition, April 2010, Detroit, Michigan.

Reference

AWS D8.1. "Specification for Automotive Weld Quality-Resistance Spot Welding of Steel." American Welding Society, Miami, Florida.

I. Advanced High-Strength Steel: Multi-Scale Modeling of Deformation Mechanism for Design of New Generation of Steels

Principle Investigator: Ju Li
Department of Materials Science and Engineering
University of Pennsylvania
3231 Walnut Street; Philadelphia, PA 19104
(484) 682-3350; email: liju@seas.upenn.edu

Co-Principle Investigator: Yunzhi Wang
Department of Materials Science and Engineering
The Ohio State University
477 Watts Hall; 2041 College Road; Columbus, OH 43210
(614) 292-0682; email: Wang.363@osu.edu

Technology Area Development Manager: William Joost
U.S. Department of Energy
1000 Independence Ave., S.W.; Washington, DC 20585
(202) 287-6020; e-mail: william.joost@ee.doe.gov

Contractor: University of Pennsylvania and The Ohio State University
Contract No.: NSF CMMI-0728069

Executive Summary

In the majority of solid-state deformation and transformation processes, including but not limited to those in steels, coupled displacive-diffusional processes is a rule rather than an exception. For example, structural phase transformations often involve coupled lattice shear, shuffle, and diffusion (Wang 10). Curvature driven grain growth may involve coupled tangential (displacive) and normal (diffusional) migration of grain boundaries (Cahn 04). Creep deformation often involves both conservative and non-conservative motion of dislocations and grain boundaries. Sometimes, the coupling between displacive and diffusional processes at atomic scale governs the rate of transformation and deformation. Mechanistic studies of these processes require modeling capabilities at atomistic length scales but diffusional time scales, and the Diffusive Molecular Dynamics (DMD) method has been developed to achieve that goal (Li 11). In all these systems, there exists a coupled diffusive-displacive minimum energy pathway (MEP) that decreases the free energy while relieving mechanical, thermal, and chemical non-equilibrium by short-ranged and long-ranged mass transfer (Sarkar 11). The intent of DMD formulation is to be able to “probe” the free energy landscape along both diffusive and displacive reaction coordinates and to be able to gain important insights from these problems.

At present, DMD has been applied to nanoindentation, hot isostatic pressing of nanoparticles, climb of edge dislocation, and diffusional void growth. In nanoindentation, the simulations demonstrate that displacive plasticity depends sensitively on the remnant debris of prior diffusional plasticity. This is evident from dislocation structure, reduction in yield load, and stiffness due to surface step formed by surface diffusion at low indentation rates and/or at high temperatures. In hot isostatic pressing, DMD captures the evolution of multiple nanoparticle compact to theoretical density revealing significance of rigid-body motion and diffusional and displacive processes in obtaining the final microstructure. Dislocation nucleation triggered by diffusive void growth is also a coupled diffusive-displacive phenomenon captured by DMD. This plays an important role in ductile failure, where near a crack tip, the intensive dislocation interactions produce vacancies well in excess of their equilibrium concentration facilitating condensation and void growth. Finally, a possible mechanism for climb of edge dislocation in FCC crystals and energetics associated with it is presented. It is shown that, when simultaneous displacive and diffusive events are allowed, there exists a coupled diffusive-displacive pathway along which the activation energy is substantially lower than the previous theoretical predictions and on par with the experimental observations.

In the following sections, we present the current status of the work and the accomplishments, future directions, and a brief description of the method and the results.

Accomplishments

- The first phase of theoretical formulation is complete (Li 11) and a fully developed code embedded in LAMMPS (Plimpton 95) platform is ready to be used. The structure of the code has been made similar to LAMMPS molecular dynamics (MD) code so that the MD users can conveniently perform a DMD simulation. Rigorous validation and some preliminary results of DMD in nanoindentation and sintering of nanoparticles have been published.
- DMD has been applied to the problem of creep failure (dislocation climb) in face centered cubic materials where long range mass transport takes place over a time scale well beyond the MD time scale. A manuscript on this topic has been submitted and is under review.
- Nudged elastic band method (Henkelman 00) on DMD free energy surface has been implemented.

Future Directions

- Density functional DMD: A more accurate free-energy density functional in terms of the site occupations that effectively include pair, triplet, quartet, etc. correlations will be adopted (deFontaine94). Currently, a simpler version of this density functional DMD (DF-DMD) is being tested, where the site occupancies are assumed to be pair-wise correlated such that the free energy of the system is minimized, which gives a unique free energy as a function of the occupancies. We assume pair correlations are independent for each pair of atoms, thus neglecting higher order correlations completely.
- Extending to multiple species system to be better suited for steel system: The current implementation of DMD in LAMMPS handles only one species, but can be extended to incorporate multiple species without much difficulty. We note that the framework for multiple species had been implemented earlier in a stand-alone code which can serve as a guideline for one looking to implement it inside LAMMPS.
- Uphill Diffusion: DMD kinetics is presently just a “downhill ski” on the DMD free-energy landscape and cannot capture up-hill phenomena in mass-action reaction coordinate space due to omission of the noise term. One can, however, easily envision implementing a variety of accelerated dynamics (Voter 02) and nudged elastic band type calculations (Henkelman 00) with DMD free energy in the extended displacive and mass-action space. One can also include a noise term in the evolution of the occupation probabilities (master equation) in the spirit of the Langevin equation. The magnitude of noise can be derived from the fluctuation-dissipation theorem (Langevin-approach).

Introduction

Materials properties depend on processes that take place on a variety of time scales. These range from atomic vibrations or dislocation-mediated slip processes, which have typical time scales of hundreds of femtoseconds (fs) to hundreds of picoseconds (ps), to diffusion, which may take place on the order of seconds or longer. This disparity in time scales leads to difficulties when trying to model slower processes where individual atomic motions may be important, such as diffusion controlled boundary migration and dislocation climb. A straightforward MD approach, with a typical time step of 1fs, would require an enormous computation time to adequately capture these processes. We have developed a novel method, called the DMD, which can capture the diffusion time scale while retaining the atomic spatial resolution by coarse-graining over atomic vibrations and evolving a site-probability representation of atomic density clouds. DMD solves master equation on a moving atomic grid. It combines long-range elastic effects and short-range atomic interactions simultaneously with gradient thermodynamics.

Approach

DMD is formulated akin to the Variational Gaussian (VG) method (Lesar 89, Lesar 91). But unlike the VG free energy, which is derived in the canonical ensemble, DMD free energy is derived in the grand canonical ensemble to incorporate the occupational probability of atomic density clouds. The use of the grand canonical ensemble becomes advantageous for

materials modeling, where the path to the finite temperature equilibrium structure may involve creation and annihilation of point defects through long range transport, chemical mixing of species, segregation at the interfaces, and reconstruction at the surface etc. A grand-canonical ensemble gives a better grip of this problem by allowing the number of atoms and their positions to change. Figure 1 shows a schematic representation of a vacancy in VG in contrast to that in DMD to illustrate the basic idea of DMD.

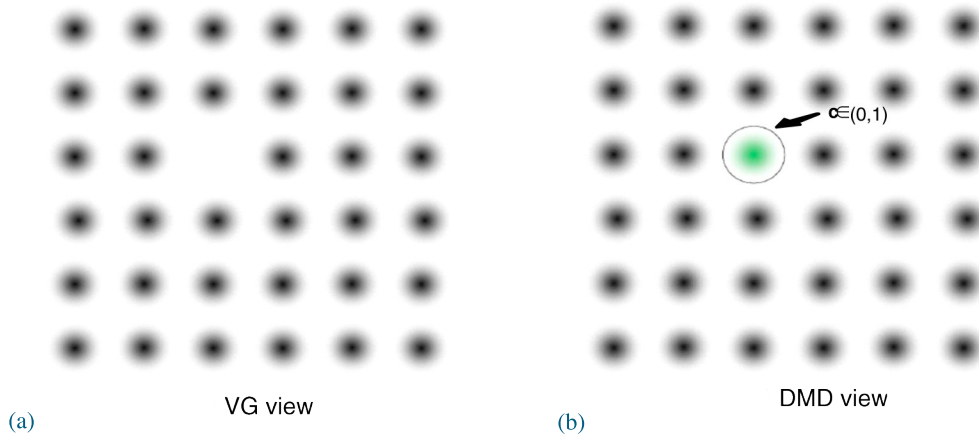


Figure 1. In contrast to $4N$ variables in VG, X_i, α_i, c_i , the mean position and the Gaussian width of vibration, DMD has $5N$ variables: $X_i, \alpha_i, c_i, \hat{i}=1..N$ the mean position, Gaussian width of vibration, and occupational probability, of atomic density clouds. (a) VG representations of a vacancy in a lattice. As in LeSar et al. (Lesar 89), here we track $M = N = 35$ sites. (b) The DMD representation. Here we track $N = 36$ sites, one of which however is partially occupied ($c \in (0,1)$) or vacant ($c \rightarrow 0$), and $M = 35$ sites are fully occupied ($c \rightarrow 1$). Note that each Gaussian cloud individually adjusts its own center position and width.

The DMD free energy (Helmholtz) in Equation 1 has three contributing terms: enthalpy, vibrational entropy and mixing entropy.

$$F_{DMD} = \sum_{i=1}^N c_i E_i(\bar{\psi}_i) + \frac{1}{2} \sum_{i=1}^N \sum_{j \neq i} c_i c_j w_{ij}(\mathbf{X}_{ij}, \alpha_i, \alpha_j) + \frac{3}{2} k_B T \sum_{i=1}^N c_i \left\{ \ln \left[\frac{\alpha_i \Lambda_T^2}{\pi} \right] - 1 \right\} + k_B T \sum_{i=1}^N \left\{ c_i \ln c_i + (1 - c_i) \ln (1 - c_i) \right\} \quad (1)$$

We define a site-wise exchange chemical potential by taking partial derivative of the free energy with respect to the site occupation probability. Once we have site-wise chemical potentials, we can drive diffusion in the system by invoking a master equation.

During a DMD simulation, each time step is realized in two parts. First, the variables $\{X_i, \alpha_i\}$ are statically minimized as in the VG method, while holding $\{c_i\}$ constant. This process can be assumed to take place instantaneously because X_i and α_i change on the inertial (ps) and thermalization (100 ps) time scales, respectively, both of which are much smaller than the diffusional time scale. Then in the second part, the $\{c_i\}$ are integrated numerically according to the master equation while holding $\{X_i, \alpha_i\}$ constant. This is equivalent to assuming the system is always in vibrational and mechanical equilibrium, but not chemical equilibrium, at each time-step. It is therefore not possible to model dynamical effects where inertia plays a role. Since displacive relaxation of $\{X_i, \alpha_i\}$ is “instantaneous” in DMD, the fundamental “clock” of DMD is controlled by the value of chemical diffusivity or diffusive time scale, but not by atomic vibration.

Results and Discussion

Here we present the application of DMD in two systems: the climb of extended edge dislocation and diffusional void growth in single crystal copper. Figure 2 shows the evolution of the dislocation lines during the climb of extended edge dislocation. Though climb of extended edge dislocation has been addressed by many researchers over the past five decades, either by continuum energy calculation or by experiments, an atomistic simulation of the whole process with atomic-level energetics is shown for the first time. Two features of the simulation are noteworthy: (a) a coupled displacive-diffusional pathway that emerges out of the DMD simulation automatically (with no human intervention) is found, and (b) along this pathway, the activation energy of 0.83 eV is lower than the previous theoretical predictions (101 eV) (Stroh 54, Grilhe 77). This minimum energy pathway which the system chose on its own under the prescribed boundary conditions reflects a naturally occurring

course that would evolve by a continuous accretion of point defects. It should be mentioned here that even though this pathway is distinctly different from that of Thomson-Balluffi, the evolution of the dislocation lines agrees overall with the Thomson-Balluffi mechanism.

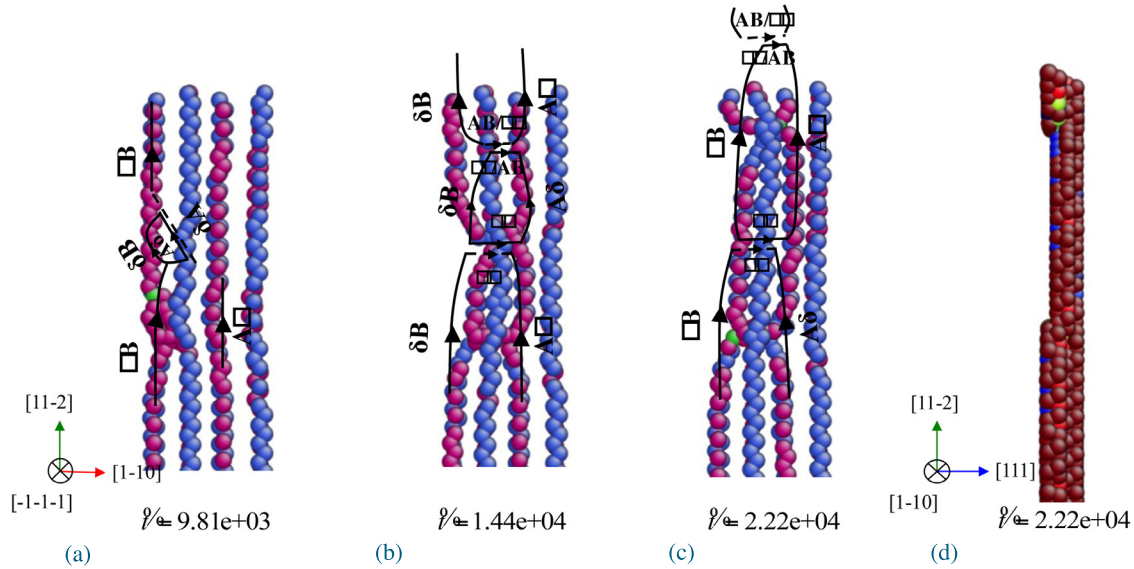


Figure 2. (a) Climb of the small stacking fault region by nucleation of prismatic loop AB followed by its growth and reaction with the partial δB at $t = 9.81 \times 10^3$. (b) Dislocation structure showing the double jog on the extended dislocations at $t = 1.44 \times 10^4$. (c) One jog swept across almost half of the line at $t = 2.22 \times 10^4$. (d) [1-10] view of the centrosymmetry plot of the same configuration showing climb by one atomic layer.

Long-range vacancy diffusion assisted void growth and subsequent dislocation nucleation is studied atomistically in single crystal copper using DMD, and the results are shown in Figure 3. We find that, when starting from a void nucleus the size of a few atoms, diffusional processes lead to a $\{111\}$ faceted growth in an otherwise perfect crystal. This process continues until the void reaches a critical size to nucleate dislocations at the corners where stress concentration is the highest. Finally, the void growth rate was compared with the steady-state continuum diffusion equation derived under spherical symmetry and a good agreement was observed.

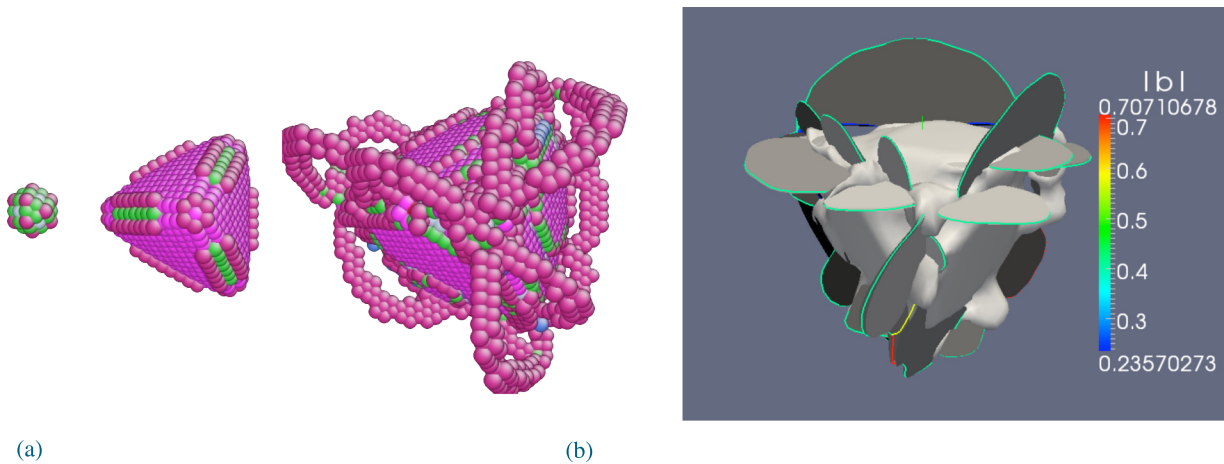


Figure 3. (a) Coordination plot of the void configurations viewed along $\langle 111 \rangle$ at different reduced times $t = 0$, $t = 5.44 \times 10^5$, $t = 1.06 \times 10^6$. Only sites with non-perfect coordination are shown. Atomic sites having $c_i < 0.01$ have been eliminated. For coordination calculation, sites having $c_i < 0.01$ were excluded from the nearest-neighbor calculation. Red, green, pink, and silver colors signify coordination number of 11, 10, 9 and 8, respectively. (b) Dislocation lines and stacking faults using dislocation extraction algorithm code by Stukowski et al. Legend shows magnitude of the Burgers vectors. Red, green and blue lines signify perfect, partial, and stair-rod dislocations respectively.

Conclusions

A vast number of researchers in materials science deal with systems at finite temperature where diffusion becomes a dominant mechanism. The path to the finite temperature equilibrium properties and structure of these systems may involve creation and annihilation of point defects through long range transport, chemical mixing of species, segregation at the interfaces, and reconstruction at the surface, etc. Often, their experimental observations cannot be correlated with theoretical predictions or atomistic simulations due to lack of reaching the appropriate time scale. DMD, built on solid statistical mechanics foundation, has the capability of bridging the gap. Unlike the other accelerated dynamics methods (Voter 02), DMD provides a natural framework that can handle coupled diffusive-displacive processes involving multiple species and that, in theory, can be coupled to well-established diffusion-microelasticity equation solvers such as finite element and phase field methods. In summary, the highlights of this method are:

- DMD thermodynamics is formulated akin to density functional theory. It is an atomic realization of regular solution model, with gradient thermodynamics, long-range elastic and short-range coordination interactions, all included.
- DMD shows the significance of probing an energy landscape simultaneously along coupled diffusive-displacive reaction coordinates in determining the MEP for many infrequent-event systems. This concept of coupled diffusive-displacive reaction coordinate is profoundly important for microstructural evolution and can lead to significant physical insights concerning the deformation and transformation mechanisms at atomic scale.

Presentations/Publications

Li, J.; Sarkar, S.; Cox, W. T.; Lenosky, T. J.; Bitzek, E.; Wang, Y. Diffusive molecular dynamics and its application to nanoindentation and sintering. *Phys. Rev. B* 2011, 84, p. 054103.

Sarkar, S.; Li, J.; Cox, W. T.; Bitzek, E.; Lenosky, T. J.; Wang, Y. Atomistic Mechanism of Climb of Extended Edge Dislocation Dipole in Copper. Submitted to *Physical Review Letters* (in review).

S. Sarkar, W. T. Cox, J. Li, Y. Wang. "Mechanism of Climb of Dissociated Edge Dislocation in Copper: A Diffusive Molecular Dynamics Study". *Materials Science & Technology*, Columbus, OH. October 16-20, 2011.

J. Li, S. Sarkar, W. T. Cox, T. J. Lenosky, E. Bitzek, Y. Wang. "Diffusive Molecular Dynamics". TMS, San Diego, CA. February 27- March 03, 2011.

S. Sarkar, W. T. Cox, J. Li and Y. Wang. "Diffusive Molecular Dynamics". *Materials Research Society Fall Meeting*, Boston, MA. November 30-December 03, 2010.

S. Sarkar, J. Li and Y. Wang. "Diffusive Molecular Dynamics Simulation of Nanoparticle Sintering". *Materials Science & Technology*, Houston, TX. October 17-21, 2010 (invited).

E. Bitzek, S. Sarkar, W. T. Cox, T. J. Lenosky, Y. Wang and J. Li. "Atomic-Scale Modeling of Diffusion-Driven Microstructure Evolution in Irradiated Metals". *DPG Spring Meeting*, March 21- 26, 2010, Regensburg, Germany.

E. Bitzek, W. T. Cox, S. Sarkar, T. J. Lenosky, Y. Wang and J. Li. "Atomic-Scale Modeling of Diffusion-Driven Microstructure Evolution", *Gordon Research Conference*, August 2-7, 2009, Andover, NH (best poster award).

References

- Wang, Y.; Li, J. Phase field modeling of defects and deformation. *Acta Mater.* 2010, 58, pp. 1212–1235.
- Cahn, J. W.; Taylor, J. E. A unified approach to motion of grain boundaries, relative tangential translation along grain boundaries, and grain rotation. *Acta Mater.* 2004, 52, pp. 4887–4898.
- Li, J.; Sarkar, S.; Cox, W. T.; Lenosky, T. J.; Bitzek, E.; Wang, Y. Diffusive molecular dynamics and its application to nanoindentation and sintering. *Phys. Rev. B* 2011, 84, p. 054103.
- Plimpton, J. Fast Parallel Algorithms for Short-Range Molecular Dynamics. *J Comput. Phys.* 1995, 117, pp. 1–19.
- De Fontaine, D. Cluster Approach to Order-Disorder Transformations in Alloys. *Solid Stat. Phys.* 1994, 47, pp. 33–176.
- Voter, A.; Montalenti, F.; Germann, T. C. Extending the Time Scale in Atomistic Simulation of Materials. *Annu. Rev. Mater. Res.* 2002, 32, pp. 321–346.
- Henkelman, G.; Uberuaga, B. P.; Jonsson, H. A climbing image nudged elastic band method for finding saddle points and minimum energy paths. *J. Chem. Phys.* 2000, 113, pp. 9901–9904.
- LeSar, R.; Najafabadi, R.; Srolovitz, D. Finite-Temperature Defect Properties from Free-Energy Minimization. *Phys. Rev. Lett.* 1989, 63, pp. 624–627.
- LeSar, R.; Najafabadi, R.; Srolovitz, D. Thermodynamics of Solid and Liquid Embedded-Atom-Method Metals: A Variational Study. *J. Chem. Phys.* 1991, 94, pp. 5090–5097.
- Stroh, A. Constrictions and jogs in extended dislocations. *Proc. Phys. Soc. B* 1954, 67, pp. 427–436.
- Grilh'e, J.; Boisson, M.; Seshan, K.; Gaboriaud, R. J. Climb model of extended dislocations in f.c.c. metals. *Philos. Mag.* 1977, 36, no. 4, pp. 923–930.

J. Advanced High-Strength Steel: Development of Novel Finite Element Simulation Tools That Implement Crystal Plasticity Constitutive Theories Using An Efficient Spectral Framework

Principle Investigator: Surya R. Kalidindi
Department of Mechanical Engineering and Mechanics, Drexel University
Philadelphia, PA 19104
(215) 895- 1311; e-mail: skalidin@coe.drexel.edu

Technology Area Development Manager: William Joost
U.S. Department of Energy
1000 Independence Ave., S.W.; Washington, DC 20585
(202) 287-6020; e-mail: william.joost@ee.doe.gov

Contractor: Drexel University
Contract No.: NSF Award CMMI 0727931

Executive Summary

The emergence of Advanced High Strength Steels (AHSS) has major implications for a broad range of structural applications. The accelerated insertion of AHSS in automotive applications demands the use of improved physics-based constitutive theories in the predictive finite element (FE) simulation tools used to optimize the performance of the final manufactured part. These improved models should reliably capture the multi-scale constitutive behavior of AHSS, while accounting for the evolution of microstructure during large plastic strains that occur in the various manufacturing processes. However, the currently used multi-scale modeling approaches are impractical for addressing this challenge since they require major computational resources. In an effort to develop an efficient practical strategy for multi-scale simulations that leads to more accurate predictions of the thermo-mechanical response of AHSS, we have developed and implemented a new spectral crystal plasticity framework that exploits the computational efficiency of discrete Fourier transforms (DFTs). This new approach was able to speed up the current crystal plasticity calculations by about two orders of magnitude. In this report, we describe our efforts in integrating this novel spectral crystal plasticity approach with the commercial FE simulation tool ABAQUS to facilitate simulation of arbitrary deformation processing operations on polycrystalline metals. The integration was accomplished through the development of a customized user material subroutine, UMAT. The integrated spectral crystal plasticity FE simulation tool produced excellent predictions similar to the classical crystal plasticity FE tool, but with major computational savings.

In order to include details of the higher-order interactions at the lower length scales, we have formulated a novel approach called Material Knowledge System (MKS) for capturing high fidelity microstructure-property-processing relationships. In this report, we also describe our efforts for integrating the MKS approach with the commercial FE package, ABAQUS, once again through a customized user material subroutine. The MKS-FE approach was validated using selected examples where we have simulated the elastic deformation responses in different composite material structures by including the microstructure features at each material point in the FE model. It is found that the MKS-FE approach accurately captured the microscale stress and strain fields in the microstructure at a significantly faster computation speed with much lower computational cost. The extension of the MKS framework to include the crystal plasticity theory will be pursued in future work.

Accomplishments

Demonstrated the first implementation of the spectral crystal plasticity approach developed for metals deforming by crystallographic slip in the commercial FE package ABAQUS through a user material subroutine, UMAT. The preliminary results of the spectral crystal plasticity FE approach accurately reproduced all of the features of the conventional crystal plasticity FE method with substantial computational savings.

Developed a new spectral crystal plasticity database for hexagonal crystal systems that deformed by slip with an arbitrary combination of basal, prism, and pyramidal slip systems. The new compact HCP database was found to speed up the crystal plasticity calculations by two orders of magnitude.

Integrated the high fidelity microstructure-property-processing relationships established by MKS framework with the commercial FE package ABAQUS to enable practical, computationally efficient, multi-scale material simulations. The new MKS-FE approach was critically evaluated through a simple case study involving elastic deformation in a component made from a composite material.

Future Directions

- Apply the spectral crystal plasticity-FE approach for simulating multiphase materials such as AHSS during complex metal forming operations.
- Critically evaluate the merits of using fast generalized spherical harmonics in place of discrete Fourier transforms in building the spectral databases for crystal plasticity. Our preliminary results indicate a promise for speeding up the crystal plasticity calculations by at least another order of magnitude.
- Extend the MKS framework to crystal plasticity framework to include grain-scale interactions. This higher-order extension to crystal plasticity approach is required to partition the imposed deformation on the polycrystal to each of the constituent grains while taking into account the details of its neighborhood. This is expected to be particularly important for multi-phase polycrystalline metals such as AHSS.
- Study the influence of the two constituent phases (ferrite and martensite) on the deformation mechanisms in Dual-Phase (DP) steels using our recently developed experimental protocols that combine the information extracted from both orientation image maps and spherical nano-indentation measurements. It is anticipated that the experimental results obtained here will help develop more reliable physics-based crystal plasticity models that can better simulate the heterogeneous deformation behavior of DP steels.

Technology Assessment

- Target - A multi-scale crystal plasticity formulation for multi-phase polycrystalline metals that can be incorporated into commercial finite element packages and executed with modest computational resources (such as a regular desktop PC).
- Gap – Lack of understanding of the specific physical phenomena responsible for improved ductility of DP steels.

Introduction

Crystal plasticity theories (Asaro and Needleman 1985; Bronkhorst et al. 1992; Kalidindi et al. 1992; Kalidindi et al. 2004) are used extensively in understanding and predicting the evolution of the underlying microstructure (mainly texture related aspects) and the concomitant anisotropic stress-strain response in polycrystalline metals subjected to finite plastic strains. Such physics-based constitutive theories are highly desirable for conducting more accurate simulations of various metal manufacturing/fabrication processes, since they provide better understanding and predictions of the material behavior. The main deterrent in the more widespread use of these theories (in place of the highly simplified phenomenological isotropic plasticity theories typically used) is the fact that the implementation of the crystal plasticity theories in a finite element modeling framework demands substantial computational resources and highly specialized expertise.

In previous years on this project (Knezevic et al. 2009; Al-Harbi et al. 2010), we have developed computationally efficient representations for the essential functions capturing the solutions to the conventional crystal plasticity theory in fcc metals subjected to arbitrary deformation paths. More specifically, functional forms have been established for the deviatoric stresses $\sigma'_{ij}(g,L)$, the lattice rotations $W_{ij}^*(g,L)$, and the total slip rates $\sum \alpha \dot{\gamma} \alpha (g,L)$ where g is the crystal lattice orientation and L is the applied velocity gradient tensor. In any given time step in the simulation of the deformation process, these functions can then be used to compute all of the needed microscale and macroscale field quantities that would be typically computed by the traditional crystal plasticity approach. The domain of the functions of interest is the product space comprising all possible crystal orientations and all possible isochoric deformation modes. New spectral representations of these functions using Discrete Fourier Transforms (DFTs) were found to be able to speed up the crystal plasticity computations by about two orders

of magnitude compared to the traditional approaches used in crystal plasticity computations. The tremendous saving in the computational time was possible by recognizing that only a limited number of the dominant DFTs were adequate to recover the functions of interest.

The spectral crystal plasticity framework developed so far addresses crystal plasticity for a region within a single crystal without taking into account the effect of local interactions between crystals. The polycrystal response was obtained using the simplifying Taylor assumption of uniform strain in all constituent grains. However, in most multiphase materials, such as AHSS, there is a need for higher-order models that account for grain interactions. Development of higher-order models requires a more sophisticated approach that partitions the imposed deformation on the polycrystal to each of the constituent grains while taking into account the details of its neighborhood. The most successful approach for accurately capturing the grain interactions in a polycrystal involves the use of FE models. However, this is impractical because it would entail executing micromechanical FE models on representative volume elements of polycrystals at each integration point in the macroscale simulation. In recent work, we employ a completely different approach to address this challenge. We have developed a new framework, called MKS (Kalidindi et al. 2010; Landi and Kalidindi 2010; Landi et al. 2010; Fast and Kalidindi 2011; Fast et al. 2011), for harvesting efficiently the essential knowledge contained in the results obtained from micro-mechanical FE models and store this knowledge in an easily accessible database. This new approach is developed by applying established methods in non-linear system theory and informatics.

In this report, we demonstrate the first implementation of our spectral crystal plasticity tools with the commercial FE package ABAQUS. The preliminary results of this new spectral crystal plasticity FE approach accurately reproduced all of the features of the conventional crystal plasticity FE method with major computational savings. Furthermore, we describe our efforts to conduct efficient multiscale material simulations using the integrated MKS-FE framework. Specifically, we illustrate the successful integration of the MKS framework with the commercial finite element package ABAQUS to enable efficient multi-scale modeling of the elastic response of a structural component made from a composite material.

Approach

We have developed spectral crystal plasticity based FE tools for simulating deformation processing operations and final mechanical performance of AHSS components. Although building the spectral database requires substantial effort, it is a one-time activity. Once an appropriate database is built, all subsequent computations requiring solutions at the lower length scales can be accomplished with minimal computational effort and resources. This new approach was first established for rigid-viscoplastic behavior and recently extended for elastic-viscoplastic deformation. Although the elastic deformation in most metals subjected to finite plastic deformation is very small and can be neglected, it is essential to include elasticity for incorporating the spectral crystal plasticity approach with the commercial FE code ABAQUS, in the form of a user material subroutine, UMAT. This is mainly because most FE simulation tools, such as ABAQUS, provide the total deformation gradient at each integration point as input to the UMAT, and not the plastic part alone. Furthermore, elasticity plays an important role in phenomena such as the springback effect, which is an elasticity driven change in the shape of a part upon unloading.

The elastic deformation was successfully included to our spectral crystal plasticity approach using the following constitutive relations:

$$\tau^{\nabla*} = C[D^*]$$

where D^* is the elastic stretching tensor, C is the 4th-rank elasticity tensor, and $\tau^{\nabla*}$ is the Jaumann rate of the Kirchoff stress τ seen by an observer who rotates with the lattice and is defined as

$$\tau^{\nabla*} = \dot{\tau} - W^* \tau + \tau W^*.$$

In order to use the above relation, the total stretching tensor needs to be decomposed into elastic and plastic parts such that the stresses computed from both the spectral crystal plasticity and Jaumann rate relations are equal to each other within an acceptable tolerance. We have developed a new efficient algorithm using modified Newton-Raphson scheme to get the right decomposition of the stretching tensor into the elastic and plastic components.

Another important task for this project was to develop and implement a computationally efficient formalism for the localization (opposite of homogenization) relationships that lie at the core of all multi-scale modeling approaches. This was accomplished using a novel concept called Materials Knowledge Systems (MKS) (Kalidindi *et al.* 2010; Landi and Kalidindi 2010; Landi *et al.* 2010; Fast and Kalidindi 2011; Fast *et al.* 2011). A salient feature of this new framework is that it facilitates flow of high-fidelity information in both directions (i.e. homogenization and localization) between the constituent length scales and thereby offers a new strategy for concurrent multi-scale modeling. This new approach was incorporated into a commercial FE package, ABAQUS, for conducting multi-scale simulation of the elastic deformation in composite microstructures. This was once again accomplished through the development of a user material subroutine, UMAT.

Results and Discussion

Integrating the Spectral Crystal Plasticity Approach with a FE Simulation Tool

We have incorporated our elastic-viscoplastic spectral crystal plasticity databases into the FE package, ABAQUS, through a user material subroutine, UMAT. As a preliminary case study, we have simulated plane strain compression of a copper polycrystalline material subjected to 50% height reduction (equivalent to about 0.7 true strain). The three-dimensional FE model consisted of 90 C3D8 elements. The initial texture was assumed to be random consisting of 720 different crystal orientations. Each integration point inside each element was assigned a different single crystal orientation, i.e. there were 8 crystals per element. The predicted stress-strain curve and deformed texture from our spectral crystal plasticity FE approach were compared against the corresponding predictions from the conventional crystal plasticity FE approach (Kalidindi *et al.* 1992) in Figure 1. It is seen that the new spectral crystal plasticity FE approach accurately reproduced all of the features of the conventional crystal plasticity FE method at a significantly faster computational speed. In this case study, the classical crystal plasticity FE simulation required 2 hour, whereas the spectral crystal plasticity FE model took only 4 minutes. In addition, a particularly attractive feature of this new spectral UMAT is that it provides the user with tremendous flexibility in making trade-offs between accuracy and computational speed. The approach described here will allow the user to perform a large number of very quick simulations at a lower than desired accuracy, identify the specific ones that appear to produce promising results, and redo these much more accurately (at a higher computational cost).

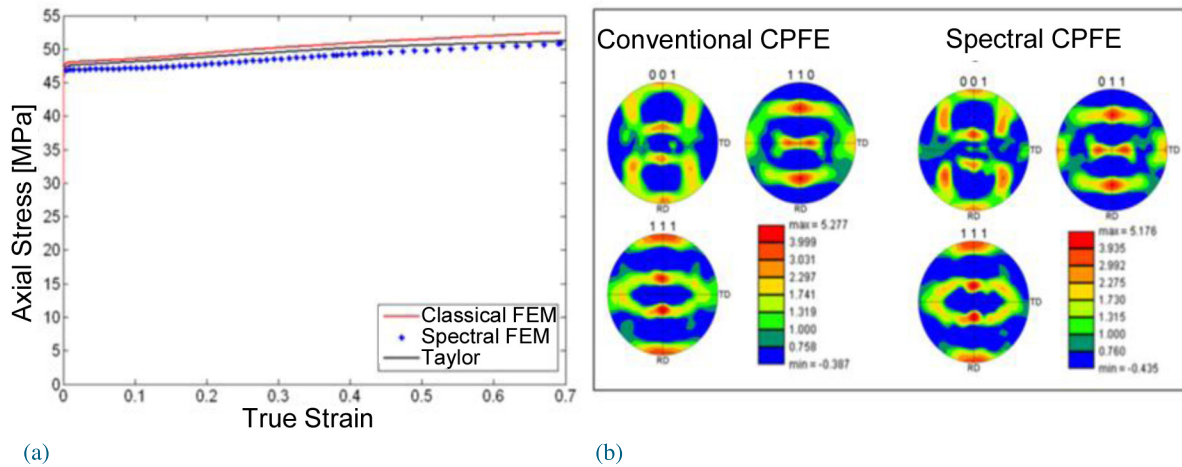


Figure 1. Comparison of the predictions from the spectral crystal plasticity FE approach against the corresponding predictions from the conventional crystal plasticity FE approach for plane strain compression of copper polycrystalline material: (a) stress-strain curves, and (b) pole figures.

MKS-FE Simulation Tool for Conducting Efficient Multi-scale Simulations

As a first demonstration of the MKS-FE approach, we consider the elastic bending of a cantilever beam made from a composite material. In this MKS-FE simulation, each material point in the macroscopic FE model is associated with a representative three-dimensional microstructure at that location (see Fig. 2 (a)). In this novel approach, information is consistently exchanged between the microscale and macroscale in a fully coupled manner. In other words, the MKS approach is used to compute the microscale spatial distribution of the stress and strain fields at each material point in the macroscopic FE model (i.e. localization) and the homogenized (volume-averaged) stress field from the microscale is transferred to the macroscale FE analyses at the component scale.

The MKS-FE approach was critically evaluated by comparing the microscale stress and strain distributions predicted from the MKS-FE approach with the corresponding predictions from a direct FE simulation with an extremely fine mesh resolution (i.e. a very large number of elements in the FE model) that allows explicit incorporation of the microstructural details (see Fig. 2 (b)). Fig. 3 shows a contour plot of the microscale ϵ^{11} component of strain for a mid-plane through the microstructure at the fixed-end of the cantilever beam (location A in Fig. 2) calculated using the MKS-FE and direct FE approaches. It is seen that the two predictions are in excellent agreement with each other. It should be noted that the predictions from the MKS-FE approach are obtained with very minimal computational effort. In this case study, the direct FE simulation that consists of ~ 6 million elements required 15 hours when using 64 processors on a supercomputer, whereas the MKS-FE model took only 55 seconds on a standard desktop computer. It is therefore clear that there is tremendous gain in computational efficiency in using the MKS approach for conducting practical multi-scale FE simulations.

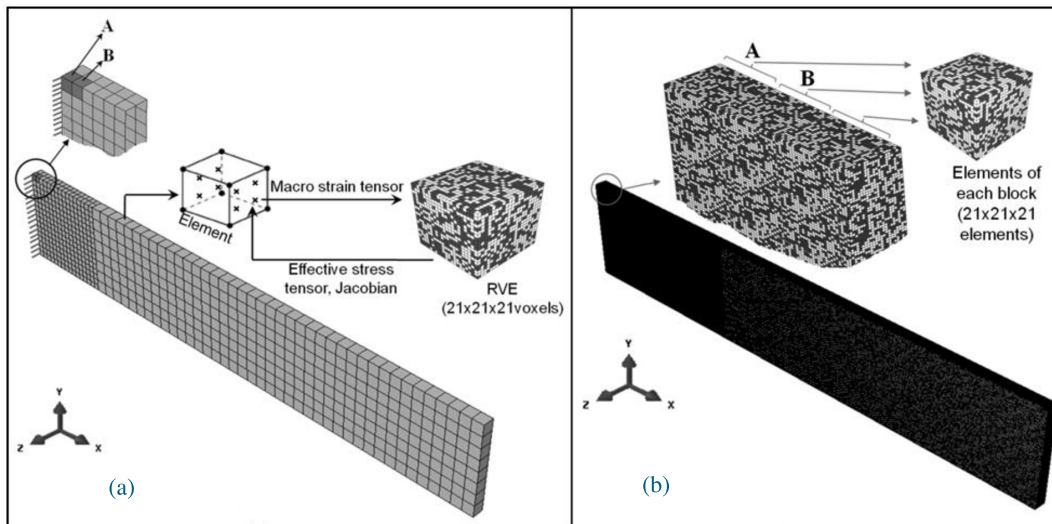


Figure 2. FE model of the cantilever beam bending problem: (a) a schematic of how the MKS approach is integrated with the FE package ABAQUS in the form of a user material subroutine (UMAT), and (b) a direct FE model of the cantilever beam used to validate the MKS-FE approach. Each element in the MKS-FE model shown in (a) is discretized into $21 \times 21 \times 21$ elements in the direct FE model shown in (b). The elements in each $21 \times 21 \times 21$ block of elements are assigned the same 3-D microscale structure and local properties as the microscale RVEs used in the MKS-FE model.

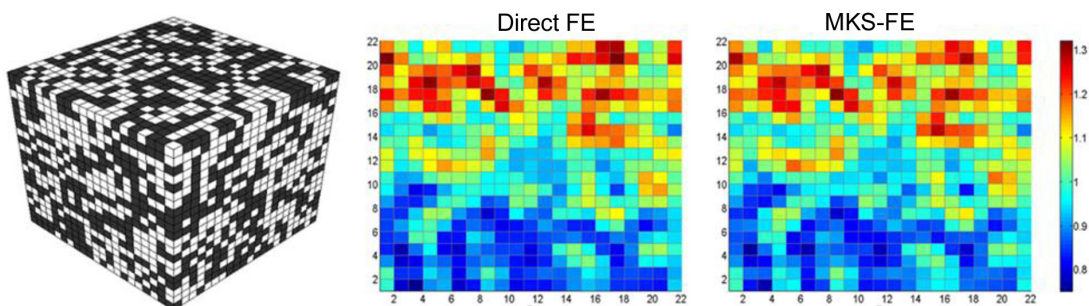


Figure 3. Comparison of contour maps of the local ϵ^{11} component of strain (normalized by the macroscopic applied strain) for the mid-plane of a 3-D microstructure (left), calculated using the MKS-FE (right) against the corresponding predictions from the direct FE model (center) at the fixed-end of the cantilever beam model shown in Figure 2.

Technology Transfer Path

The current work will result in improved physics-based multi-scale material models that are needed for successful design of cost-effective manufacturing processes for a new class of AHSS with dramatically improved performance characteristics. For example, the new models can optimize the performance of engineering components used in automotive applications which leads to higher safety and increased fuel efficiency. We are in discussions with a number of commercial entities (including Scientific Forming Technologies Corporation and Materials Resource Laboratories, Inc.) to explore opportunities for technology transfer.

Conclusion

In this report, we have demonstrated the first integration of recently developed spectral crystal plasticity databases for cubic polycrystalline materials with the FE package, ABAQUS, in the form of a user materials subroutine, UMAT. The preliminary results showed that the new spectral crystal plasticity FE approach produces excellent predictions similar to the classical crystal plasticity FE method but at a significantly faster computational speed. We have also extended our spectral crystal plasticity framework to include elastic deformation which was necessary for integrating our approach with the FE package, ABAQUS.

We have also presented the first implementation of the recently developed MKS framework into the FE package, ABAQUS, through a user material subroutine, UMAT, for conducting efficient multi-scale simulation. As an example, we have simulated the elastic deformation responses in different composite material structures by including the microstructure features at each material point in the FE model. The new MKS-FE approach was critically evaluated by comparing its predictions with the corresponding predictions from a highly discretized direct FE model. It is found that the MKS-FE approach accurately captured the microscale stress and strain fields in the microstructure at a significantly faster computation speed compared to the direct FE models. The extension of the MKS framework for crystal plasticity will be pursued in future work.

Presentations/Publications/Patents

Al-Harbi, H.; Kalidindi, S.; and Shaffer, J. Use of Spectral Databases for Crystal Plasticity Finite Element Simulations of Bulk Deformation Processing of Cubic Metals. Invited talk at TMS2011, February 27-March 3, 2011, San Diego, CA.

Al-Harbi, H.; Fast, T.; Kalidindi, S.; and Landi, G. Development of Novel Finite Element Simulation Tools that Implement Crystal Plasticity Constitutive Theories Using an Efficient Spectral Framework. NSF CMMI Research and Innovation Conference 2011. January 4-7, 2011, Atlanta, GA.

Al-Harbi, H.; Fast, T.; Kalidindi, S.; and Landi, G. Development of Novel Finite Element Simulation Tools that Implement Crystal Plasticity Constitutive Theories Using an Efficient Spectral Framework. Proceedings of 2011 NSF Engineering Research and Innovation Conference, Atlanta, Georgia.

Fast, T.; Kalidindi, S.; Landi, G.; and Niezgoda, S. Formulation and Calibration of Higher-Order Elastic Localization Relationships Using the MKS Approach. USNCCM-11, Minneapolis, July 25-28, 2011, Minneapolis, MN.

References

- Al-Harbi, H. F., M. Knezevic and S. R. Kalidindi (2010). "Spectral Approaches for the Fast Computation of Yield Surfaces and First-Order Plastic Property Closures for Polycrystalline Materials with Cubic-Triclinic Textures." *Cmc-Computers Materials & Continua* 15(2): 153-172.
- Asaro, R. J. and A. Needleman (1985). "Texture development and strain hardening in rate dependent polycrystals." *Acta Metallurgica et Materialia* 33(6): 923-953.
- Bronkhorst, C. A., S. R. Kalidindi and L. Anand (1992). "Polycrystalline plasticity and the evolution of crystallographic texture in fcc metals." *Philosophical Transactions of the Royal Society of London Series a-Mathematical Physical and Engineering Sciences* 341(1662): 443-477.
- Fast, T. and S. R. Kalidindi (2011). "Formulation and Calibration of Higher-Order Elastic Localization Relationships Using the MKS Approach " *Acta Materialia* 59 4595-4605.
- Fast, T., S. R. Niezgoda and S. R. Kalidindi (2011). "A new framework for computationally efficient structure-structure evolution linkages to facilitate high-fidelity scale bridging in multi-scale materials models." *Acta Materialia* 59(2): 699-707.
- Kalidindi, S. R., A. Bhattacharya and R. Doherty (2004). "Detailed Analysis of Plastic Deformation in Columnar Polycrystalline Aluminum Using Orientation Image Mapping and Crystal Plasticity Models." *Proceedings of the Royal Society of London: Mathematical, Physical and Engineering Sciences*. 460(2047): 1935 - 1956
- Kalidindi, S. R., C. A. Bronkhorst and L. Anand (1992). "Crystallographic texture evolution in bulk deformation processing of fcc metals." *Journal of the Mechanics and Physics of Solids* 40(3): 537-569.
- Kalidindi, S. R., S. R. Niezgoda, G. Landi, S. Vachhani and T. Fast (2010). "A Novel Framework for Building Materials Knowledge Systems." *Cmc-Computers Materials & Continua* 17(2): 103-125.
- Knezevic, M., H. F. Al-Harbi and S. R. Kalidindi (2009). "Crystal plasticity simulations using discrete Fourier transforms." *Acta Materialia* 57(6): 1777-1784.
- Landi, G. and S. R. Kalidindi (2010). "Thermo-Elastic Localization Relationships for Multi-Phase Composites." *Cmc-Computers Materials & Continua* 16(3): 273-293.
- Landi, G., S. R. Niezgoda and S. R. Kalidindi (2010). "Multi-scale modeling of elastic response of three-dimensional voxel-based microstructure datasets using novel DFT-based knowledge systems." *Acta Materialia* 58(7): 2716-2725.

K. Development of Nano-Acicular Duplex Steels

Principal Investigator: David C. Van Aken
Missouri University of Science and Technology
Materials Science and Engineering
1400 N. Bishop; Rolla, MO 65409-0340
(573) 341-4717; e-mail: dcva@mst.edu

Co-Principal Investigator: Julia E. Medvedeva
Missouri University of Science and Technology
Physics
1315 N. Pine St.; Rolla, MO 65409-0640
(573) 341-4789; e-mail: juliaem@mst.edu

Co-Principal Investigator: Von L. Richards
Missouri University of Science and Technology
Materials Science and Engineering
1400 N. Bishop; Rolla, MO 65409-0340
(573) 341-4730; e-mail: vonlr@mst.edu

Technology Area Development Manager: William Joost
U.S. Department of Energy
1000 Independence Ave., S.W.; Washington, DC 20585
(202) 287-6020; e-mail: william.joost@ee.doe.gov

Contractor: Missouri University of Science and Technology (Missouri S&T)
Contract No.: National Science Foundation Award CMMI-0726888

Executive Summary

A chemical and structural analysis of stacking faults (SF) in Fe-Mn-Al-C austenitic (fcc) (where Fe stands for iron, Mn for Manganese, Al for Aluminum, and C is for carbon) solid solutions was considered using the Vienna ab-initio simulation package (VASP) with the projector augmented waves (PAW) for pseudopotentials. The generalized gradient approximation (GGA) was used for the exchange-correlation functional. An energy cutoff of 350 eV was used for the plane-wave basis set. A 24-atom supercell was used to calculate the generalized stacking fault energy (GSFE) relative to impurity (C, Mn, and Al) distribution and a $4 \times 4 \times 4$ k-point mesh was chosen. The atomic positions were relaxed until the forces were smaller than $0.01 \text{ eV}/\text{\AA}$. Despite the importance of the magnetic interactions in Fe-based alloys, we are restricted by the calculations for nonmagnetic state and discuss only the role of interatomic interactions. Calculations show that the impurities have influence on the stacking fault energies (SFE) only when located within a few interatomic layers near the SF. As a result, the SFE does not depend on the average concentration of the impurities in matrix, but is highly sensitive to the concentration of the impurities in the vicinity of the SF defect. The parabolic dependence of the intrinsic stacking fault energy (ISFE) which controls the plasticity mechanism in the austenitic steel with high Mn content, may be reproduced when all Mn atoms are located near the SF. We predict that Mn will show a slight tendency for segregation near SF, while C prefers to be located far from the SF (fcc/hcp) region. Both Al and C impurities linearly increase the ISFE, while the formation of Mn-C pairs and short range Al-ordering restrain the SFE growth. Short range order in Fe-Al-C alloys strongly affects the energy barrier for nucleation of dislocations and leads to softening phenomenon.

Accomplishments

- Demonstrated that ab-initio methods allow one to understand how the position and concentration of impurities at SF may affect the GSFE and what are the microscopic origins of this behavior.
- The peritectic formation of austenite was studied in two lightweight steels with primary δ -ferrite volume fractions of 0.35 and 0.66. Peritectic austenite was seven times more likely to have the Kurdjumov-Sachs (K-S) orientation relationship when the primary δ -ferrite volume fraction was 0.66. In contrast, a lower volume fraction of δ -ferrite produced a peritectic reaction where both δ -ferrite and austenite grew with either a $\langle 100 \rangle$ or $\langle 110 \rangle$ parallel to the heat flux and the K-S orientation was observed for only 5% of the peritectic interfaces.
- Melting point phenomena of micron-sized indium particles embedded in an Al matrix were studied by means of acoustic emission. The acoustic energy measured during melting increased with indium content. Acoustic emission during the melting transformation suggests a dislocation generation mechanism to accommodate the 2.5% volume strain required for melting of the embedded particles. A geometrically necessary increase in dislocation density of $4.1 \times 10^{13} \text{ m}^{-2}$ was calculated for the 17 wt% indium composition. Acoustic emission during bainitic transformation can now be explained by a mechanism of volume strain accommodation by dislocation generation, rather than a displacive transformation mechanism.

Future Directions

- Missouri S&T has been contracted by the leading steel maker in Korea to study the precipitation of K-carbide in a new lightweight automotive steel.
- Work hardening behavior and dynamic strain aging phenomena will be studied with respect to formation of Mn-C-Al solute clusters and subsequent K-carbide formation.

Approach

Lightweight steel is produced by alloying with Al and silicon (Si) to produce a composition having greater than 4 weight percent (wt. %) of these 3p elements. In terms of atomic percent, this level of alloy represents more than 10 percent and these steels are expected to demonstrate new physical and mechanical behaviors. C and the addition of Mn (up to 30 weight percent) are often employed to stabilize the austenite. It should be noted that interstitial C strongly increases the ISFE and suppresses twinning, while the role of Mn with respect to ISFE is more complex and is largely responsible for a wide variation in microstructure, work hardening behavior, and enhanced plasticity [Allain et al., Sato et al., Liang et al., Van Swygenhoven et al.]. These impurities may form bound Mn-C pairs in Fe-Mn-C alloy that may significantly retard the dislocation motion [Dastur and Leslie]. Al is an effective alloying element to raise the ISFE of high Mn steels and to suppress formation of deformation twins, but these alloys still maintain high work hardening rates [Dumay et al., Zuidema et al., Canadinc et al., Astafurova et al.] which is associated with planar slip and the formation of high dislocation density sheets [Canadinc et al.]. There is strong evidence that short range order (SRO) promotes planar slip [Owen and Grujicic] and is important in the work hardening behavior prior to the formation of twins in Hadfield steel [Zuidema et al.]. Effects of SRO and the formation of Mn-C dipoles on ISFE in Fe-Mn-Al-C alloys have not been studied using either thermodynamic models or ab-initio methods. Since the interaction between solute and interstitial atoms plays an important role in the mechanical properties, the knowledge of impurity distribution is critical for understanding the microscopic origin of the impurity effect.

Results & Discussion

To study the dependence of ISFE (γ_{ISF}) on Mn concentration, we performed calculations for a different number of Mn atoms at the SF on the (111) plane. Our calculations provide parabolic dependence of γ_{ISF} with Mn content at the SF (Figure 1, black line). The SFE decreases with a

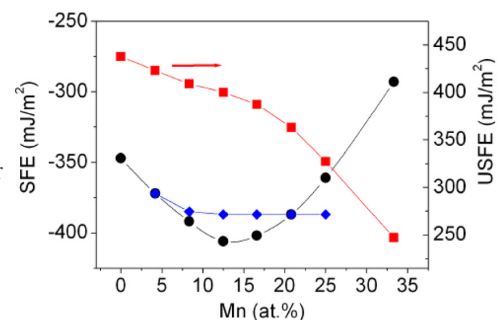


Figure 1. The intrinsic (black) and unstable (red) SF energies as dependent upon Mn concentration at the SF in fcc Fe-Mn. The ISFE does not change significantly (blue line) for concentrations greater than 10% when the Mn atoms are distributed on n layers below the SF.

mean rate of 5 mJ/m² per 1 at.% within the interval from 0 to 12 at.% Mn, and increases with a slightly larger rate of 6.6 mJ/m² per 1 at.% from 15 to 33 at.% Mn. The minimum corresponds to 13 at.% Mn and coincides with the predictions made by Lee and Choi.

As it follows from Figure 1, the Mn concentration range up to 30% yields smaller values of the SFE as compared to those in fcc Fe. A decrease in SFE favors the formation of martensite. Thus, our calculations suggest that the martensite structure may be formed within this concentration interval, whereas austenite is stable for higher Mn concentrations. These results correlate with the phase diagram of Fe-Mn which demonstrates that ϵ -martensite is not formed above 30% Mn. Extrapolation of the SFE curve by the function $y=0.2927*x^2-8.09*x-346$ (Figure 1) gives that γ_{ISF} changes sign from negative to positive at ~ 50 at.% Mn.

The parabolic behavior of γ_{ISF} was obtained within the nonmagnetic scheme, and suggests that the interatomic interactions and not magnetism determines the nonlinear dependence of the SFE on Mn content. Note, that we considered variations in Mn concentration exactly at the SF. Earlier first-principles calculations, which predicted a gradual increase in the SFE for all Mn concentrations [Hickel et al.], were performed for nonmagnetic Fe (A1), Fe₇₅Mn₂₅ (L₁₃), Fe₅₀Mn₅₀ (L₁₀), Fe₂₅Mn₇₅ (L₁₃), and Mn (A1) phases where Mn atoms were in the ordered positions. In order to determine how Mn positions relative to the SF region influences γ_{ISF} , we also calculated the following two configurations: (i) when the n Mn atoms were distributed not on the SF plane, but through the n layers below the SF; and (ii) when one Mn atom was substituted in the n^{st} -layer ($n = 0, 1, 2, 3$) below SF. Such calculations will provide an answer to whether γ_{ISF} depends on the Mn position relative SF or on the total Mn concentration in bulk. In the first case (Figure 1, blue line), we found that the SFE does not depend on Mn concentration for $x > 10$ at.%, and all changes in SFE are produced by the Mn atoms located in the 0th- and 1st-layers below SF. Indeed, as follows from the calculations (ii), Mn in the second layer below SF does not affect γ_{ISF} (we obtained -372, -354 and -349 mJ/m² for Mn in the 0th, 1st and 2d layer, respectively). Hence, Mn that is distant from the SF layer does not change the SFE ($\gamma_{ISF} = -347$ mJ/m² for fcc Fe). Thus, it is the Mn atoms distributed within the one interlayer distance near the SF region that affect γ_{ISF} , but not the total Mn concentration in the Fe-Mn alloy.

The lowering of SFE with increasing n also suggests that the location of Mn near the SF is energetically more preferable than being far away from this region. To elucidate the effect of Mn on the formation of SF, the unstable SFE γ_{US} were calculated, which represent the lattice resistance to the formation of SF. As shown in Figure 1 (red line), γ_{US} decreases with increasing Mn content at SF for $x > 20$ at.% Mn. This points to a lower energy barrier for the formation of SF in the regions with high Mn concentration. These results indicate the possibility of Mn segregation near SF and, hence, near the interface boundary of an fcc-hcp microstructure.

We would like to stress that the magnitude of SFE obtained in our study, as well as in previous *ab-initio* calculations, is greatly underestimated compared to the experimental values and the thermodynamic estimations. For example, SFE for pure Fe being extrapolated to $T=0$ K is higher than -40 mJ/m² [Dick et al.]. This discrepancy may be related to magnetic interactions. Indeed, the comparison of paramagnetic and nonmagnetic results for pure Fe show that magnetism increases the SFE from -350 mJ/m² to -150 mJ/m² [Dick et al.], but nevertheless it is far from the extrapolated value. The effect of light interstitial impurities is a possible reason for this discrepancy. In particular, *ab-initio* calculations predict that nitrogen increases SFE by 73 mJ/m² per 1 at.% N and that SFE is close to zero at 4 at.% N [Kibey et al.].

Next, we consider the effect of C occupying the octahedral interstitial sites in the n^{st} -layer ($n = 0, 1, 2, 3$) below SF in fcc Fe. One C atom at the SF layer ($n = 0$) increases both γ_{US} , and γ_{ISF} , but they are gradually reduced to the values for pure Fe as n increases (Table 1). C in the third layer below SF ($n = 3$) has little influence on the SF energy. There is a strong

Table 1. The SFE (mJ/m²) for single impurity in the n -layer below SF and two impurity atoms in k - and l - layers ($n = k, l$).

		$n = 0$	$n = 1$	$n = 2$	$n = 3$	$n = 0, 0$
Mn	γ_{US}	423	430	433	435	409
	γ_{ISF}	-372	-354	-349	-347	-392
C	γ_{US}	547	541	493	449	601
	γ_{ISF}	49	-51	-145	-320	203
Al	γ_{US}	319	432	429	435	232
	γ_{ISF}	-284	-295	-343	-347	-192

dependence of γ_{ISF} on both the C location and its concentration, whereas the variations in γ_{US} are less significant. A much larger increase would occur in the case when two nearest C atoms are at the SF layer ($n = 0,0$). The increase in γ_{US} (energy barrier for the SF formation) with C content (Table 1) indicates that the segregation of interstitial C at the SF is unlikely.

The dependence of the SFE on the impurity layer n shows (Table 1) that C, in marked contrast to Mn, has a strong effect within a more extended region, which covers three atomic layers near the SF defect. Averaging γ_{ISF} on the three SF planes ($n = 0, 1, 2$) produces an increase of 74 mJ/m^2 per 1 at.% C. This coincides with the nitrogen effect on SFE that was predicted to be 75 mJ/m^2 per 1 at.%N [Kibey et al.]. These results imply that in the Fe-C alloy, the fcc phase is more favorable than hcp. Indeed, C suppresses the $\gamma \rightarrow \epsilon$ transformation and is known as a strong austenite stabilizer. The decrease in SFE obtained from the thermodynamic estimations (12 mJ/m^2 per 1 at.%C) is notably smaller than the value obtained via averaging through three n layers near the SF plane. The high γ_{US} shows that C does not segregate at SF and does not favor the formation of SF. C prefers to be far from the SF region, and this may be the reason for the overestimated value obtained by including the nearest region to SF into the average. Taking into account this argument, the averaged γ_{ISF} through the more distant layers ($n = 2, 3$) produces an increase of 28 mJ/m^2 per 1 at.% C, which is in a better agreement with thermodynamic estimations.

In accord with these findings on the favorable impurity positions, the formation of Mn-C pair may influence the SFE. Calculations for one (Mn-C-Fe) and two Mn (Mn-C-Mn) atoms substituted in the preferable positions near the interstitial C at the SF reduces the ISFE by 5 mJ/m^2 and 9 mJ/m^2 per 1 at.% Mn in comparison with the value for Fe-C, respectively. This means that the formation of bound Mn-C pairs near the SF plane restrains the increase in SFE caused by C alone. As a result, the calculated SFE is in a better agreement with the observed value.

For Al, we considered the substitutional sites in the n^{st} -layer ($n = 0, 1, 2$) below SF as well as the Al concentration effect (Table 1, Figure 2). We obtained that Al impurity in fcc Fe lead to an increase of SFE which depends on the Al distribution and concentration. Al (4 at.%) located at SF or in the first (nearest) layer leads to the similar increase of γ_{ISF} , while there is no effect on SFE when Al is in the second or third layer ($n = 2$ or 3). The increase in γ_{ISF} averaged over the layers $n = 0, 1$, and 2 is 10 mJ/m^2 per 1 at.% Al. The concentration of 8 at.% Al was modeled by two atoms which were: (i) both at SF ($n = 0,0$), or (ii) one atom at SF and one atom in the first layer ($n = 0,1$) below SF. For Al atoms in $n = 0,0$ and $n = 0,1$ positions, the SFE increases by 19 mJ/m^2 and 11 mJ/m^2 per 1 at.% Al, respectively. This result shows a correct trend in the changes of γ_{ISF} with Al addition, but shows a much greater increase than previous thermodynamic estimations and experimental data, that showed the increase in SFE of 5 mJ/m^2 [Yang and Wan].

We found that γ_{US} is sharply reduced with Al alloying. For the concentration of 12 at.% Al, USFE decreased by a factor of three times (Figure 2). This means that Al may segregate near the SF plane. Secondly, it points out that Al sharply lowers the energy barrier for SFs and dislocation formation, and therefore favors enhanced plasticity.

Planar slip before mechanical twinning was observed in the Fe-Mn-Al-C alloys with rather high SFE, while a planar slip is traditionally considered to dominate in alloys with low SFE [Park et al.]. Here it should be noted that planar slip in face centered cubic materials is often associated with SRO or short range clustering. Gerold and Karnthaler explained the softening as a result of disorder of either SRO or short range clustering by the initial dislocation glide during yielding, which permits easy flow of successive dislocations. A SRO suggested in Fe-Mn-Al-C steel was related to the precursor of Fe_3AlC_x precipitates [Park et al.].

Our investigations of the relative distribution of impurities in fcc Fe demonstrate the preference for Al to occupy the position related to D0_3 structure. In the Fe-C alloy it corresponds to the formation of perovskite-like K-carbide Fe_3AlC with E2_1 crystal structure, where Al occupies the $(0,0,0)$ position, Fe atoms are in the $(\frac{1}{2}, \frac{1}{2}, 0)$ positions, and C is located at the center octahedral site $(\frac{1}{2}, \frac{1}{2}, \frac{1}{2})$.

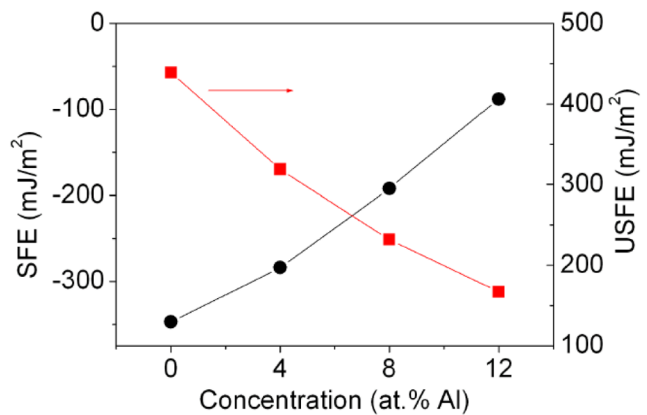


Figure 2. The intrinsic (black) and unstable (red) SFE as dependent upon Al concentration at the SF in fcc Fe-Al.

To determine how the SRO affects the SFE, we modeled the Al distribution near SF plane and calculated γ_{ISF} and γ_{US} for the different Al positions. First of all, we found that the ordering of two Al atoms in the positions, which correspond to their sites in D0_3 , results in an energy gain of 14 meV as compared to the other possible Al positions. Furthermore, the SFE γ_{ISF} and γ_{US} depend on the Al ordering near the SF plane. We obtained that if the positions of two Al atoms at the nearest SF planes correspond to the D0_3 ordering, γ_{US} is sharply reduced from 230.3 mJ/m^2 to 137.3 mJ/m^2 , while γ_{ISF} almost does not change (it decreases by only 4.2 mJ/m^2). To understand the reasons for such a selective effect of the Al ordering on the generalized SFE, we considered the changes in the Fe-Fe, Fe-Al and Al-Al distances under displacements on the (111) plane. The $1/12\langle 112 \rangle$ displacement, which corresponds to unstable SF (γ_{US}) makes two ordered Al atoms being at the distance $R_{\text{Al-Al}}$ of 2.89 Å, which is larger than the Al-Al distance of 2.82 Å in fcc Al, while for all other Al positions $R_{\text{Al-Al}}$ becomes equal to 2.33 Å (that is much shorter than in fcc Al). So, the bonding between Al atoms is much stronger in the second structure, while the structure with partial Al ordering corresponds to the weaker Al-Al bonding with respect to fcc Al.

Three Al atoms ordered within three layers near the SF plane lead to a further reduction of γ_{US} up to 83 mJ/m^2 , while γ_{ISF} decreases to -356 mJ/m^2 . Thus, SRO reduces the energy barrier γ_{US} for the SF dislocations, but does not increase the SFE. Furthermore, SRO may be responsible for the overestimated SFE in our calculations for non-ordered Al distribution. Based on these results we can conclude that a SRO, which was suggested in Fe–Mn–Al–C steel to explain the planar slip deformation before occurrence of mechanical twinning regardless of the SFE value [Park et al.], is related to the precursor of Fe_3AlC_x precipitates. We demonstrated that the mechanism of the softening phenomenon is attributed to a sharp lowering of the energy barrier for SF dislocations due to a short range ordering of Al atoms in Fe-Al-C.

Conclusion

The calculations of generalized SFE demonstrated that only impurities distributed within the two layers near SF plane affect the SFE. We showed that the SFE does not depend on the average concentration of impurities in the matrix and there is a strong sensitivity of the SFE to the concentration of impurities in the vicinity of stacking fault defect. The true parabolic dependence of the SFE on Mn concentration was obtained for Mn concentrated at the SF plane, while Mn located more than one interlayer distance from SF plane does not influence the stacking fault energy. The SFE dependence upon the composition of the SF plane explains why previous studies examining a disordered structure failed to predict the composition dependence of the SFE. Our results correlate with the phase diagram of Fe-Mn, which demonstrates that ϵ -martensite is not formed above 30% Mn. The lowering of SFE with Mn content up to 25 at.% demonstrates also that the location of Mn near SF is more energy preferable than being far away from this region. Both Al and C linearly increase SFE (both impurities suppress the $\gamma \rightarrow \epsilon$ transformation) and this effect is more pronounced for interstitial C. We show that C prevents the formation of SF and prefers to occupy locations remote from the SF region. Short range order in Fe-Al-C alloys strongly affects the energy barrier for dislocation nucleation and results in softening, while it inhibits the increase in SFE. Certainly, this approach provides the GSF energies at zero temperature and does not predict the exact values of SFE, which strongly depends on temperature and impurity distribution. Nevertheless, we demonstrated that ab-initio methods give the opportunity to establish how the position and concentration of impurities at SF affect the GSF energies.

Presentations/Publications/Patents

“Magnetism in bcc and fcc Fe with carbon and manganese,” N.I. Medvedeva, D. Van Aken, and J.E. Medvedeva, *J. Phys. Cond. Matter* 22, 316002 (2010).

“The Effect of carbon distribution on the manganese magnetic moment in bcc Fe-Mn alloy”, N.I. Medvedeva, D.C. Van Aken, J.E. Medvedeva, *J. Phys.: Cond. Matter*, 23, 326003 (2011).

References

- Allain, S., Chateau, J.-P., Bouaziz, O., Migot S., and Guelton, N., "Correlations between the calculated stacking fault energy and the plasticity mechanisms in Fe-Mn-C alloys," *Mater. Sci. Eng. A* vol. 387-389 (2004) 158-162.
- Astafurova, E. G., Kireeva, I. V., Chumlyakov, Y. I., Maier, H. J., and Sehitoglu, H., The influence of orientation and aluminum content on the deformation mechanisms of Hadfield steel single crystals, *Int. J. Mat. Res.* Vol. 98 (2007) pp. 144-149.
- Canadinc, D., Sheitoglu, H., Maier, H. J., and Chumlyakov, Y. I., Strain hardening behavior of aluminum alloyed Hadfield steel single crystals, *Acta Mater.* Vol. 53 (2005) 1831-1842.
- Dastur, Y.N. and Leslie, W. C., Mechanisms of Work Hardening in Hadfield Manganese Steel, *Metall. Trans. A*, vol. 12 (1981) 749-759.
- Dick, A., Hickel, T. and Neugebauer, J., The Effect of Disorder on the Concentration-Dependence of Stacking Fault Energies in $\text{Fe}_{1-x}\text{Mn}_x$ - a First Principles Study, *Materials Technology*, 80, 603 (2009).
- Dumay, A., Chateau, J.-P., Allan, S., Migot, S., and Bouaziz, O., Influence of addition elements on the stacking-fault energy and mechanical properties of an austenitic Fe-Mn-C steel, *Mater. Sci. A* vols. 483-484 (2008) 184-187.
- Gerold, V. and H.P. Karnthaler, H.P., "On the Origin of Planar Slip in F.C.C. Alloys," *Acta Metall.* Vol. 37 (1989) 2177-2183.
- Hickel, T., Dick, A., Grabowski, B., Kormann, F., Neugebauer, J., Steel Design from Fully Parameter-free Ab Initio Computer Simulations, *Steel Res. Int.*, vol. 80, p.4 (2009).
- Kibey, S., Liu, J.B., Curtis, M.W., Johnson, D.D., and Sehitoglu, H., Effect of nitrogen on generalized stacking fault energy and stacking fault widths in high nitrogen steels, *Acta Mater.* 54, 2991 (2006).
- Lee, Y.-K. and Choi, C.-S., Driving force for $\gamma \rightarrow \epsilon$ martensitic transformation and stacking fault energy of γ in Fe-Mn binary system, *Metall. Mater. Trans. A* 31A, p. 355 (2000).
- Liang, X., McDermid, J. R., Bouaziz, O., Wang, X., Embury, J.D., and Zurob, H. S., Microstructural evolution and strain hardening of Fe-24Mn and Fe-30Mn alloys during tensile deformation, *Acta Mater.* Vol. 57 (2009) 3978-3988.
- Owen, W.S. and Grujicic, M., Strain Aging of Austenitic Hadfield Manganese Steel," *Acta Mater.* Vol. 47 (1999) 111-126.
- Park, K.-T., Jin, K.G., Ho, S.H., Hwang, S.W., Choi, K., and Lee, C.S., Stacking fault energy and plastic deformation of fully austenitic high manganese steels: Effect of Al addition, *Mater. Sci. Eng. A* vol. 527 (2010) 3651-3661.
- Sato, S., Kwon, E.-P., Imafuku, M., Wagatsuma, K., and Suzuki, S., "Microstructural characterization of high-manganese austenitic steels with different stacking fault energies," *Mater. Characterization* vol. 62 (2011) 781-788.
- Van Swygenhoven, H., Derlet, P. M., and Froseth, A.G., "Stacking fault energies and slip in nanocrystalline metals," *Nat. Mater.* Vol. 3 (2004) 399-403.
- Yang, W.S. and Wan, C.M., "The influence of aluminum content to the stacking fault energy in Fe-Mn-Al-C alloy system" *Journal of Materials Science*, vol. 25, p. 1821, 1990.
- Zuidema, B. K., Subramanyam, D.K., and Leslie, W.C., The Effect of Aluminum on the Work Hardening and Wear Resistance of Hadfield Manganese Steel," *Metall. Trans. A*, vol. 18, (1987) 1629-1639.

L. Sheet Formability and Springback of Advanced High-Strength Steels - The Ohio State University

Principal Investigator: Robert H. Wagoner
Department of Materials Science and Engineering, The Ohio State University
2041 College Rd.; Columbus, OH 43210
(614) 292-2079; e-mail: wagoner.2@osu.edu

Co-Principal Investigator: James G. Schroth
Staff Research Engineer, General Motors R&D Center
30500 Mound Road; M/C 480-106-212 ; Warren, MI 48090-9055
(586) 986-0977; e-mail: james.g.schroth@gm.com

Technology Area Development Manager: William Joost
U.S. Department of Energy
1000 Independence Ave., S.W.; Washington, DC 20585
(202) 287-6020; e-mail: william.joost@ee.doe.gov

Contractor: The Ohio State University
Contract No.: CMMI-0729114

Executive Summary

Advanced high strength steels (AHSS) promise enormous potential benefits to society, but their widespread adoption requires a fundamental understanding of their constitutive behavior. In particular, accurate predictions of formability and springback of AHSS are the critical issues in the manufacturing of vehicles. In this work, fundamental understanding in the cause of shear fracture and proper representation of nonlinear unloading is formulated.

A new plastic constitutive model (H/V Model) that relates flow stress to strain, strain-rate, and temperature is formulated to accurately predict failure of AHSS. The H/V Model and novel draw-bend fracture (DBF) tests revealed that the shear fracture of dual phase (DP) steels occurs by temperature increases during forming in sharp bending regions related to their high ductility and strength. Microstructural details are not usually a determining factor, but can be important in rare cases.

Activity and Developments

Sheet Formability and Springback of Advanced High Strength Steels

Principal Investigator: Robert H. Wagoner
(614) 292-2079; e-mail: wagoner.2@osu.edu

Accomplishments

- An accurate temperature-sensitive constitutive model (H/V Model) was developed, tested, and published. It predicts necking and failure with more accuracy than any existing constitutive model.
- A novel constitutive model for general nonlinear unloading was proposed (QPE Model). Simulation of draw-bend springback (DBS) results gave predictions within the experimental scatter when using QPE model.
- New DBF tests reproducing industrial conditions for formability and springback were devised and verified. DBF uses dual displacement control and provides better reproducibility and consistency than other such methods.

Future Directions

- The fundamental understanding gained for DP steels as well as the newly-developed techniques will be leveraged and extended to new AHSS such as TRIP, TWIP, CP, and QP steels.
- Symmetric DBF tests with real-time Digital Image Correlation (DIC) will be conducted.
- Elevated-temperature, continuous, tension-compression testing, and elevated-temperature balanced biaxial bulge testing will be conducted.

Introduction

AHSS are being used currently by automakers for their impressive combinations of strength and ductility. Widespread adoption of AHSS offers major improvements in automotive vehicle performance: safety, energy usage, emissions, and durability. In particular, DP steels are the most widely used of the various AHSS available. These materials feature coarse microstructures of a soft ferrite matrix and hard martensite “islands.” The internal stress concentrations produce early yield, high work hardening, and thus high tensile ductility. While the properties of DP steels are remarkable, there exist two major obstacles, both related to forming: unpredictable formability and springback. Understanding and predicting their formability and springback requires accurate knowledge and representation of their plastic constitutive behavior.

In this report, a novel H/V Model based on the tensile data of uniform strain range was developed and adopted to predict the AHSS failure without damage mechanics. Also, a new Quasi-Plastic-Elastic (QPE) model, in which the evolution of Young’s modulus and Bauschinger effect were considered, introduced, and conducted to predict springback in draw bend tests by using FEM code.

Approach

The draw-bend test, originally developed for measuring friction and wear (Demeri, 1981; Vallance and Matlock, 1992; Wenzloff et al., 1992; Haruff et al., 1993), was developed by the PI’s group for springback (Carden, 2002) and fracture applications (Kim et al., 2011; Damborg et al., 1997). The principle of the test is shown in Figure 1. A strip of sheet metal is formed around a circular tool (typically fixed and lubricated) and then drawn using a dual-actuation control system. For fracture testing, displacement rates at each end of the strip specimen are controlled to avoid the spurious reversal of strip motion. For springback testing, constant sheet tension is maintained while drawing at constant speed V_1 .

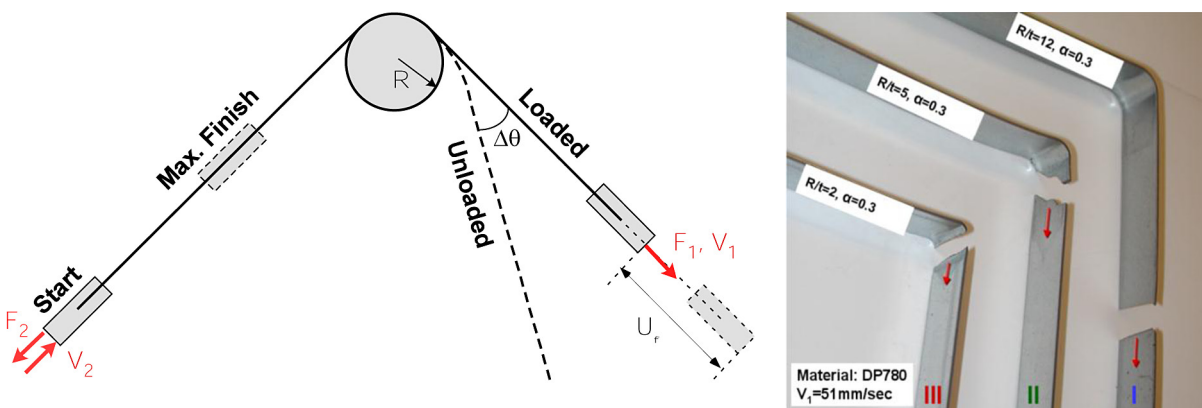


Figure 1: Schematic and variables of the draw-bend tests (left side) and the three types of fractures observed in the draw-bend fracture (DBF) test (right side).

Results and Discussion

Draw-bend fracture (DBF) and Draw-bend springback (DBS) Tests

DBF tests under various conditions revealed that the occurrence of shear fractures increased dramatically at higher pulling speeds. This observation led to the postulate that deformation-induced heating was the critical factor rendering shear fractures unpredictable by normal (isothermal) methods used industrially. AHSS's, because of their high energy product, produce significantly more heat than traditional steels. At industrial forming strain rates, the deformation is nearly adiabatic.

This theory was confirmed (Kim et al., 2009, 2010, 2011; Sung et al., 2009, 2010, 2011) by infrared thermographic measurements and comparison with a series of thermo-mechanical finite element (FE) simulations using the H/V constitutive model (next section). For the three grades of DP steels tested at various rates and R/t ratios, measured temperatures agreed with the simulation-predicted ones within 5° C. Also, displacements to failure were predicted with an average error of 15% thermo-mechanically, as compared with 65% isothermally. Thus, deformation-induced heating is the major contributor to unpredictable shear fracture.

H/V Model and Thermo-Mechanical Simulations

An empirical 1D constitutive form describing the flow stress as a function of strain, strain-rate, and temperature was developed (Sung et al., 2010). The function consists of three multiplicative functions describing strain hardening (f), strain-rate sensitivity (g), and temperature sensitivity (h) as follows:

$$\sigma = \sigma(\epsilon, \dot{\epsilon}, T) = f(\epsilon, T) \cdot g(\dot{\epsilon}) \cdot h(T) \quad (1)$$

The functions g and h are standard forms, but the function f is novel. It combines, using a linear combination coefficient α , the two typical novel strain hardening forms f_h (Hollomon, 1945) and f_v (Voce, 1948):

$$f(\epsilon, T) = \alpha f_H + (1 - \alpha) f_V \quad (2)$$

The parameter α is allowed to vary linearly with temperature, such that at low homologous temperatures the expected power-law hardening is obtained (i.e. $\alpha=1$) while at higher temperatures a saturation stress is observed (i.e. $\alpha=0$).

The constitutive form embodied in Equations (1) and (2) has been shown to reproduce the tensile behavior of DP steels accurately, Figure 2, even in the post-uniform (necking) region. The H/V model is markedly better in reproducing non-isothermal behavior (Figure 2 (a)), as well as isothermal behavior (Figure 2 (b)). It accomplishes this by extrapolating more accurately to the higher strains encountered in the post-uniform strain regime (Matlock et al., 2011).

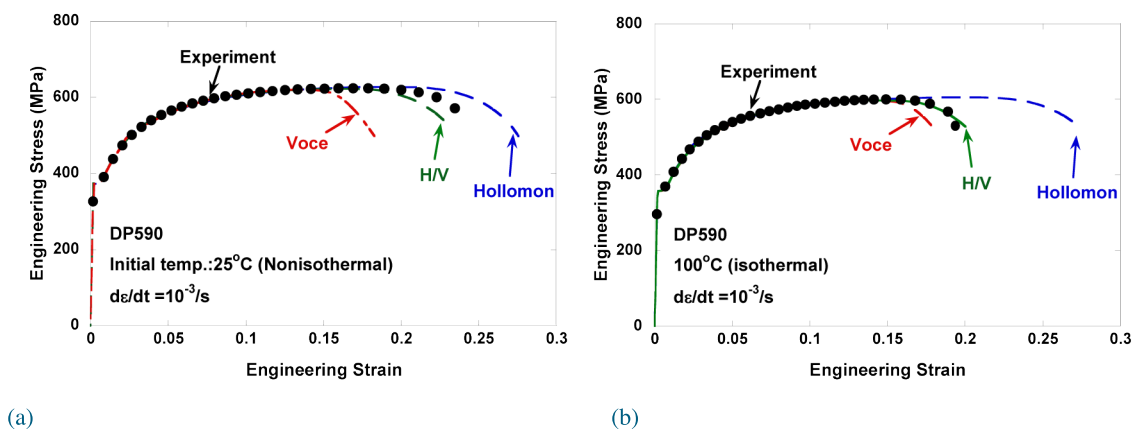


Figure 2. Comparison of tensile data and FE simulations using selected constitutive models: (a) nonisothermal tests, and (b) isothermal tests.

Tensile elongations were predicted using the H/V model for 3 DP steels (590, 780, 980) and at 3 temperatures (25, 50, 100° C). Results were compared with isothermal (Hollomon, 1945; Voce, 1948) and non-isothermal models (Lin and Wagoner, 1986; Rusinek and Klepaczko, 2010). The H/V results were within 3-6% of the measurements, as compared with 19-42% error for the standard formulations. Similar results were obtained for predicting draw-bend failure modes (shear vs. tension) and pull-distance to failure.

QPE Model

AHSS show large nonlinear unloading or “variable modulus effect” following plastic deformation that has significant effect on springback (Morestin and Boivin, 1996; Augereau et al., 1999; Cleveland and Ghosh, 2002; Caceres et al., 2003; Luo and Ghosh, 2003; Yey and Cheng, 2003; Yang and Cheng, 2003). For DP steels, effective Young’s modulus up to 32% less than the hand book value upon unloading was observed (Cleveland and Ghosh, 2002).

A consistent 3-D description of nonlinear unloading (“QPE Model”) was proposed, developed, implemented in FE codes, tested, and verified (Sun and Wagoner, 2011). The QPE model introduces a third component of strain that is recoverable (elastic-like) but energy dissipative (plastic-like). It reproduces nonlinear loading and unloading curves following stress/strain path changes, Figure 3 (a), where existing approaches fail. Draw-bend springback simulations agreed with experiments to within 3 degrees (total springback ~ 50 degrees) for QPE model, vs. 6-18 degrees for standard formulations (Sun and Wagoner, 2011).

Figure 3 (b) shows that the QPE loop characteristics depend only on the magnitude of the stress change after plastic deformation, not on the details of the alloy or its microstructure (DP 780 vs. DP 980), or on the degree of unloading (i.e. partial unloading vs. unloading to zero stress).

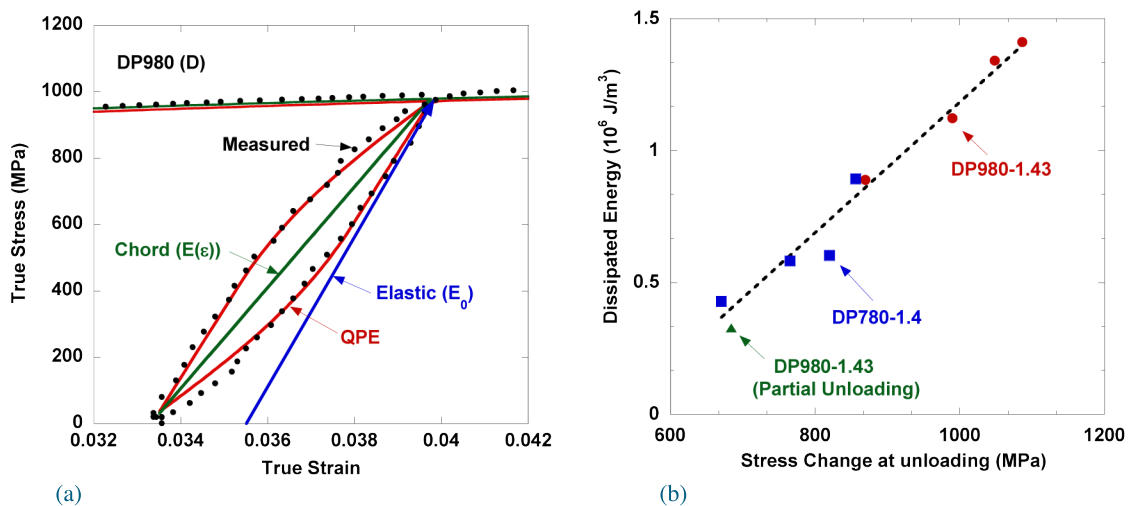


Figure 3. QPE model predictions and measurements: (a) unloading-reloading cycle for DP 980, QPE vs. existing approaches and experiment, (b) measured dissipated energy is function of stress change only, not alloy, microstructure or degree of unloading.

Conclusion

The following fundamental breakthroughs were made:

- Shear fracture occurs by temperature increases in sharp bending regions related to the high ductility and strength of the alloys. Microstructural details are not usually a determining factor, but can be important in rare cases.
- A class of material behavior deemed “quasi-plastic elastic” was identified as responsible for complex, nonlinear unloading that can increase springback by more than 30%, much greater than for traditional autobody steels.
- An accurate temperature-sensitive constitutive model (H/V Model) was developed.
- New draw-bend tests reproducing industrial conditions for formability and springback were devised and verified.

Presentations/Publications/Patents

- Gram, M., Wagoner, R. H., Fineblanking of High Strength Steels: Control of Material Properties for Tool Life. *J. Mat. Proc. Technol.*, 2011. 211, pp. 717-728.
- Gram, M., Fineblanking of Advanced High Strength Steels: Control of Material Properties for Tool Life, M. S. Thesis, Dept. Materials Science and Engineering, The Ohio State University, 2010.
- Kim, J. H., Sung, J. H., Matlock, D. K., Kim, D., Wagoner, R. H. Predicting Shear Failure of Dual-Phase Steels. in NUMIFORM 2010, Proc. 10th Int. Conf. Numer. Meth. Ind. Form. Proc. 2010. Vol.1, eds. F. Barlat, Y. H. Moon, M. G. Lee, AIP Conf. Proc. #1252, New York, pp. 63-70.
- Kim, J. H., Sung, J. H., Piao, K., Wagoner, R. H., The Shear Fracture of Dual-Phase Steel. *Int. J. Plasticity*, 2011. 27, pp. 1658-1676.
- Kim, H., Yang, Y. P., Wagoner, R. H., Bandar, A.: Predictions of Shear Failure in Stamping of Advanced High Strength Steels (AHSS), AISI Shear Fracture Symposium, August 19, 2010, Dearborn, Michigan.
- Lim, H., Lee, M. G., Sung, J. H., Kim, J. H. Wagoner, R. H., Time-Dependent Springback of Advanced High Strength Steels. *Int. J. Plasticity* (Accepted for publication).
- Lim, H., Lee, M. G., Sung, J. H., Kim, J. H., Wagoner, R. H., 2011, Time-Dependent Springback of Advanced High Strength Steels, NUMISHEET 2011, Seoul, Korea.
- Piao, K., Lee, J. K., Kim, H. Y., Wagoner, R. H., An Elevated Temperature Tension / Compression Test for Sheet Material. *Int. J. Plasticity*, (Submitted for publication).
- Piao, M., An Elevated-Temperature Tension/ Compression Test and Its Application to Magnesium AZ31B, Ph. D. Dissertation, Dept. Materials Science and Engineering, The Ohio State University, 2011.
- Sun, L., Wagoner, R. H., Complex Unloading Behavior: Nature of the Deformation and Its Consistent Representation. *Int. J. Plasticity*, 2011. 27, pp. 1126-1144.
- Sun, L., Wagoner, R. H., A Consistent Constitutive Model for Nonlinear Unloading Behavior, The 14th ESAFORM Conf. Mater. Form., Esaform 2011, AIP Conf. #1353, 2011, pp. 159-2011.
- Sun, L., Wagoner, R. H., Constitutive Modeling of Proportional and Non-proportional Hardening of Dual-Phase Steels, *J. Mater. Proc. Technol.*, (Submitted for publication)
- Sun, L., Wagoner, R. H., 2011, Complex Unloading Behavior: Nature of the Deformation and Its Consistent Constitutive Representation, NUMISHEET 2011, Seoul, Korea.
- Sun, L., Complex Unloading Model for Springback Prediction, Ph. D. Dissertation, Dept. Mechanical Engineering, The Ohio State University, 2011.
- Sung, J. H., Kim, J. H., Wagoner, R. H., A Plastic Constitutive Equation Incorporating Strain, Strain-Rate, and Temperature. *Int. J. Plasticity*, 2010. 26, pp. 1746-1771.
- Sung, J. H., The Causes of “Shear Fracture” of Dual-Phase Steels, Ph. D. Dissertation, Dept. Mechanical Engineering, The Ohio State University, 2010.
- Wagoner, R. H., Sung, J. H., Kim, J. H., Kim, D. Y., Matlock, D. K.: FE and Analytical Study of Draw-Bend Failure of AHSS, ESAFORM 2010, Brescia, Italy, April 7, 2010.
- Wagoner, R. H., Kim, J. H., Sung, J. H., Matlock, D. K., Kim, D. Y.: Predicting the Shear Failure of Dual-Phase Steels, NUMIFORM 2010, Pohang, Korea, June 16, 2010.
- Wagoner, R. H., Kim, J. H., Sung, J. H., Matlock, D. K., Kim, D. Y.: Predicting the Shear Failure of Dual-Phase Steels, AISI Shear Fracture Symposium, August 19, 2010, Dearborn, Michigan.

Wagoner, R. H., Kim, J. H., Sung, J. H., Matlock, D. K., Kim, D. Y.: The Formability of Dual-Phase Steels, Posco, Gwangyang, S. Korea, September 15, 2010.

Wagoner, R. H., Kim, J. H., Sung, J. H.: Simple Analytical Model of Shear Fracture, Metal Forming Conference, Toyohashi, Japan, September 20, 2010.

Wagoner, R. H.: The Formability of Dual-Phase Steels, ArcelorMittal, Paris, France, October 26, 2010.

References

Augereau, F., Roque, V., Robert, L., and Despaux, G., Non-destructive testing by acoustic signature of damage level in 304L steel samples submitted to rolling, tensile test and thermal annealing treatments. *Mat. Sci. Eng. A-Struct. Mater. Prop. Micro. Proc.*, 1999. 266: p. 285-294.

Caceres, C.H., Sumitomo, T., and Veidt, M., Pseudoelastic behaviour of cast magnesium AZ91 alloy under cyclic loading-unloading. *Acta Materialia* 2003. 51: p. 6211-6218.

Carden, W.D., Measurement of Springback. *Int. J. Mech. Sci.*, 2002, 44: p79-101

Cleveland, R.M., and Ghosh, A. K., Inelastic effects on springback in metals. *International Journal of Plasticity*, 2002. 18: p. 769-785.

Damborg, F.F., Wagoner, R. H., Danckert, J., Matlock, D. K. Stretch-bend formability. in *MP2M-Cener Seminar*. 1997. Danish Technical University. Demeri, M.Y., The stretch-bend forming of sheet metal. *Journal of Applied Metalworking*, 1981. 2: p. 1-3.

Haruff, J.P., Hylton, T. A., Matlock, D. K., Frictional response of electrogalvanized sheet steels. *The Physical Metallurgy of Zinc coated steel*, 1993.

Hollomon, J.H., Tensile deformation. *Trans. AIME*, 1945. 162: p. 268–290.

Kim, J. H., Sung, J. H., Wagoner, R. H. Thermo-Mechanical Modeling of Draw-Bend Formability Tests. in *Proc. IDDRG: Mat. Prop. Data for More Effective Num. Anal.* 2009. eds. B. S. Levy, D. K. Matlock, C. J. Van Tyne, Colo. School Mines, 2009, pp. 503-512.

Kim, J. H., Sung, J. H., Matlock, D. K., Kim, D., Wagoner, R. H. Predicting Shear Failure of Dual-Phase Steels. in *NUMIFORM 2010, Proc. 10th Int. Conf. Numer. Meth. Ind. Form. Proc.* 2010. Vol.1, eds. F. Barlat, Y. H. Moon, M. G. Lee, AIP Cof. Proc. #1252, New York, pp. 63-70

Kim, J. H., Sung, J. H., Piao, K., Wagoner, R. H., The Shear Fracture of Dual-Phase Steel. *Int. J. Plasticity*, 2011. 27, pp. 1658-1676.

Lin, M. R., Wagoner, R. H., Effect of temperature, strain, and strain rate on the tensile flow stress of I. F. steel and stainless steel type 310. *Scripta Metallurgica*, 1986. 20: p. 143-148.

Luo, L.M., and Ghosh, A. K., Elastic and inelastic recovery after plastic deformation of DQSK steel sheet. *J. Eng. Mater. Technol.-Trans. ASME*, 2003. 125: p. 237-246.

Matlock, D. K, Gibbs, P. J., Speer, J. G., De Moor, E., Wagoner, R. H., Schroth, J. G., On the Importance of Stability-Controlled Retained Austenite in New Advanced High Strength Steels, *Proceedings NSF CMMI Research and Innovation Conference*, Atlanta, Georgia, January 4-7, 2011, NSF, Washington, DC, Paper No. 0729114, 11 pages.

Morestin, F., and Boivin, M. , On the necessity of taking into account the variation in the Young modulus with plastic strain in elastic-plastic software. *Nuclear Eng. Design*, 1996. 162: p. 107-116.

Rusinek, A., Klepaczko, J. R., Shear testing of a sheet steel at wide range of strain rates and a constitutive relation with strain-rate and temperature dependence of the flow stress. *Int. J. Plasticity*, 2001. 17: p. 87-115.

Sun, L., Wagoner, R. H., Complex Unloading Behavior: Nature of the Deformation and Its Consistent Representation. *Int. J. Plasticity*, 2011. 27, pp. 1126-1144.

Sung, J.H., Kim, J. H., Wagoner, R. H. Accurate Constitutive Equation for Dual Phase Sheet Steels., in *Proc. IDDRG 2009, Proc. IDDRG: Mat. Prop. Data for More Effective Num. Anal. 2009.* eds. B. S. Levy, D. K. Matlock, C. J. Van Tyne, Colo. School Mines, 2009, pp. 165-176.

Sung, J. H., Kim, J. H., Wagoner, R. H., A Plastic Constitutive Equation Incorporating Strain, Strain-Rate, and Temperature. *Int. J. Plasticity*, 2010. 26, pp. 1746-1771

Sung, J. H., Kim, J. H., Wagoner, R. H. , The Draw-Bend Fracture Test (DBF) and Its Application to DP and TRIP Steels. *J. Mater. Proc. Technol*, 2011. (in preparation).

Vallance, D.W., Matlock, D. K., Application of the bending-under-tension friction test to coated sheet steels. *Journal of Materials Engineering and Performance*, 1992. 1: p. 685-694.

Voce, E., The relationship between stress and strain for homogeneous deformation. *Journal of the Institute Metals*, 1948. 74: p. 537-562.

Wenzloff, G.J., Hylton, T. A., Matlock, D. K., A new procedure for the bending under tension friction test. *Journal of Material Engineering and Performance*, 1992. 1: p. 609-613.

Yeh, H.Y., and Cheng, J. H., NDE of metal damage: ultrasonics with a damage mechanics model. *International Journal of Solids and Structures* 2003. 40: p. 7285-7298.

Yang, M., Akiyama, Y., and Sasaki, T. , Evaluation of change in material properties due to plastic deformation. *Journal of Materials Processing Technology*, 2004. 151: p. 232-236.